Winter 2018

Gust Alleviation System for General Aviation Aircraft

Lucas Coleman Mills
Old Dominion University

GUST ALLEVIATION SYSTEM FOR

GENERAL AVIATION AIRCRAFT

by

LUCAS COLEMAN MILLS
B.S. August 2015, Old Dominion University

A Thesis Submitted to the Faculty of
Old Dominion University in Partial Fulfillment of the
Requirement for the Degree of

MASTER OF SCIENCE

AEROSPACE ENGINEERING

OLD DOMINION UNIVERSITY
December 2018

Approved by:

Brett Newman (Director)

Colin Britcher (Member)

Drew Landman (Member)

ABSTRACT

GUST ALLEVIATION SYSTEM FOR GENERAL AVIATION AIRCRAFT

Lucas Coleman Mills
Old Dominion University, 2018
Director: Dr. Brett Newman

A designed control motion scheme to improve passenger comfort in general aviation aircraft by reducing normal acceleration and pitch rate due to turbulence is investigated. An aerodynamic math model is created for ViGYAN's Active Ride Improvement System flight article, a one-eighth scale Pilatus Porter PC-6 with conventional forward main wing, aft horizontal and vertical tails, and a single engine with tractor configuration. The test article incorporates a full-span gust flap and forward mounted gust sensor to mechanize the gust alleviation control system, and these features are present in the dynamic model. The model is a two degree of freedom linear pitch-plunge description of the flight dynamics and is enhanced by including separate gust effects and indicial lifts. Three wind fields are input to the model for linear simulation testing with the controls both fixed and active, and comparisons are drawn for alleviations in the human motion sickness range. The system successfully produced nearly an order of magnitude reduction in normal acceleration and an order of magnitude reduction in pitch rate. This gust alleviation performance shows that the ride improvement concept appears feasible by offering significant improvement in passenger comfort in general aviation aircraft experiencing turbulence with practical engineering implementation.

Co-Directors of Advisory Committee: Dr. Colin Britcher
Dr. Drew Landman

ACKNOWLEDGEMENTS

I would like to take this opportunity to thank the people who helped and contributed to the successful completion of this thesis. First, I would like to thank Dr. Brett Newman for being my thesis director, for his edits to this report, and for his guidance throughout the duration of this project. I would also like to thank Drs. Colin Britcher and Drew Landman for their time spent in reviewing this manuscript and for their participation on my thesis committee. I am grateful to my mother and father, who have always supported me and my educational endeavors. I would like to thank ViGYAN and its employees for the opportunity to work with their company and for the funding for this project. Finally, I would like to extend a big thank you to Norman Crabill for serving as a mentor, for providing quality direction, and for sharing stories of his aerospace engineering career, which provided me with inspiration over the two years that I spent on this project; they are stories that I will never forget.

NOMENCLATURE

Variable		Units
A_{ij}	State space matrix element	$-$
AR_t	Tail aspect ratio	$-$
AR_w	Wing aspect ratio	$-$
B_{ij}	State space matrix element	$-$
C_{ij}	State space matrix element	$-$
C_{L_q}	Coefficient of lift due to pitch rate	rad^{-1}
C_{L_α}	Coefficient of lift due to angle of attack	rad^{-1}
$C_{L_{\dot{\alpha}}}$	Coefficient of lift due to angle of attack rate	rad^{-1}
$C_{L_{\delta_e}}$	Coefficient of lift due to elevator deflection	rad^{-1}
$C_{L_{\delta_f}}$	Coefficient of lift due to flap deflection	rad^{-1}
C_{M_q}	Coefficient of moment due to pitch rate	rad^{-1}
C_{M_α}	Coefficient of moment due to angle of attack	rad^{-1}
$C_{M_{\dot{\alpha}}}$	Coefficient of moment due to angle of attack rate	rad^{-1}
$C_{M_{\delta_e}}$	Coefficient of moment due to elevator deflection	rad^{-1}
$C_{M_{\delta_f}}$	Coefficient of moment due to flap deflection	rad^{-1}
$\bar{c}$	Mean aerodynamic chord	ft
c_b	Body chord	ft
c_t	Tail chord	ft
c_w	Wing chord	ft
D_{ij}	State space matrix element	$-$

e	Form factor	$-$
$\vec{F}$	Force vector	lbf
$\vec{F}_A$	Aerodynamic force vector	lbf
$\vec{F}_g$	Gravity force vector	lbf
$\vec{F}_T$	Thrust force vector	lbf
F_x	Force component in x axis	lbf
F_y	Force component in y axis	lbf
F_z	Force component in z axis	lbf
$\vec{G}$	Translational momentum vector	$slug \cdot ft/s$
$\vec{g}$	Gravitational acceleration vector	ft/s^2
$\vec{H}$	Angular momentum vector	$slug \cdot ft^2/s$
I_{xx}, I_{yy}, I_{zz}	Aircraft moments of inertia	$slug \cdot ft^2$
I_{xy}, I_{yz}, I_{xz}	Aircraft products of inertia	$slug \cdot ft^2$
$\hat{\imath}$	x axis unit vector	$-$
$\hat{\jmath}$	y axis unit vector	$-$
$\hat{k}$	z axis unit vector	$-$
k_{e1}	Elevator first motion gain	$-$
k_{e2}	Elevator second motion gain	$-$
k_f	Flap gain	$-$
k_i	Transfer function gain	$-$
L	Rolling moment	$ft \cdot lbf$
L	von Karman turbulence scale length	ft
L_b	Aerodynamic body indicial state space variable	$-$

L_{CS}	Indicial control surface lift	–
L_e	Aerodynamic elevator indicial state space variable	–
L_f	Aerodynamic flap indicial state space variable	–
L_g	Indicial gust lift	–
L_t	Aerodynamic tail indicial state space variable	–
L_w	Aerodynamic wing indicial state space variable	–
L_α	Indicial angle of attack lift	–
$\vec{M}$	Moment vector	$ft \cdot lbf$
M	Pitching moment	$ft \cdot lbf$
$\vec{M}_A$	Aerodynamic moment vector	$ft \cdot lbf$
$\vec{M}_T$	Thrust moment vector	$ft \cdot lbf$
M_q	Angular acceleration due to pitch rate	$\frac{rad/s^2}{rad/s}$
M_t	Tail angular acceleration	$\frac{rad/s^2}{rad}$
M_{w+b+f}	Wing and body angular acceleration	$\frac{rad/s^2}{rad}$
M_α	Angular acceleration due to angle of attack	$\frac{rad/s^2}{rad}$
$M_{\dot{\alpha}}$	Angular acceleration due to angle of attack rate	$\frac{rad/s^2}{rad/s}$
$M_{\delta e}$	Angular acceleration due to elevator deflection	$\frac{rad/s^2}{rad}$
M_{δ_f}	Angular acceleration due to flap deflection	$\frac{rad/s^2}{rad}$
m	Mass	$slug$
N	Yawing moment	$ft \cdot lbf$

n_z	Normal acceleration	g
P	Roll rate	rad/s
$\dot{P}$	Roll acceleration	rad/s^2
p_i	Transfer function pole	$-$
Q	Pitch rate	rad/s
$\dot{Q}$	Pitch acceleration	rad/s^2
R	Yaw rate	rad/s
$\dot{R}$	Yaw acceleration	rad/s^2
$\vec{R}$	Total position vector	ft
$\vec{R}_{cm}$	Position vector of center of mass	ft
$\vec{r}$	Relative position vector	ft
s	Half chord lengths	$-$
s	Laplace variable	s^{-1}
$\bar{s}$	Mean body area	ft^2
s_b	Body area	ft^2
s_{b_c}	Cross sectional body area	in^2
s_t	Tail area	ft^2
s_w	Wing area	ft^2
t	Temporal variable	s
U	Velocity in x axis	ft/s
$\dot{U}$	Acceleration in x axis	ft/s^2
V	Velocity in y axis	ft/s
$\dot{V}$	Acceleration in y axis	ft/s^2
V_b	Body volume	ft^3

$\vec{V}$	Total velocity vector	ft/s
$\vec{V}_{cm}$	Velocity vector of center of mass	ft/s
V_{cm}	Velocity magnitude of center of mass	ft/s
$\vec{v}$	Relative velocity vector	ft/s
W	Velocity in z axis	ft/s
$\dot{W}$	Acceleration in z axis	ft/s^2
w_g	Vertical gust velocity	ft/s
x	Body reference frame coordinate axis	$-$
x_{ac}	Aerodynamic center from wing leading edge	ft
x_b	Aerodynamic body indicial state space variable	$-$
x_{cm}	Center of mass from wing leading edge	ft
x_{cp}	Center of pressure from wing leading edge	ft
x_e	Aerodynamic elevator indicial state space variable	$-$
x_f	Aerodynamic flap indicial state space variable	$-$
x_t	Aerodynamic tail indicial state space variable	$-$
x_w	Aerodynamic wing indicial state space variable	$-$
y	Body reference frame coordinate axis	$-$
y_b	Aerodynamic body indicial state space variable	$-$
y_e	Aerodynamic elevator indicial state space variable	$-$
y_f	Aerodynamic flap indicial state space variable	$-$
y_t	Aerodynamic tail indicial state space variable	$-$
y_w	Aerodynamic wing indicial state space variable	$-$
Z_q	Vertical acceleration due to pitch rate	$\frac{ft/s^2}{rad/s}$

Z_α	Vertical acceleration due to angle of attack	$\frac{ft/s^2}{rad}$
$Z_{\dot{\alpha}}$	Vertical acceleration due to angle of attack rate	$\frac{ft/s^2}{rad/s}$
Z_{δ_e}	Vertical acceleration due to elevator deflection	$\frac{ft/s^2}{rad}$
Z_{δ_f}	Vertical acceleration due to flap deflection	$\frac{ft/s^2}{rad}$
Z_{w+b}	Wing and body vertical acceleration	$\frac{ft/s^2}{rad}$
z	Body reference frame coordinate axis	$-$
z_i	Transfer function zero	$-$
α	Angle of attack	rad
α_g	Gust angle of attack	rad
β	Sideslip angle	rad
Δt	Simulation time step	s
δ_a	Aileron deflection	rad
δ_e	Elevator deflection	rad
δ_f	Flap deflection	rad
δ_{gs}	Forward gust sensor deflection	rad
δ_r	Rudder deflection	rad
ϵ_{DW}	Downwash parameter	$-$
ϵ_e	Elevator alpha per delta	$-$
ϵ_f	Flap alpha per delta	$-$
μ	Viscosity of air	$slug/ft\ s$

$\vec{\omega}$	Angular velocity vector	rad/s
Φ	von Karman Power Spectrum	$\left(\frac{ft}{s}\right)^2/rad/ft$
Φ	Roll angle	rad
$\dot{\Phi}$	Roll angle rate of change	rad/s
$\dot{\vec{\Phi}}$	Roll angle rate of change vector	rad/s
Ψ	Yaw angle	rad
$\dot{\Psi}$	Yaw angle rate of change	rad/s
$\dot{\vec{\Psi}}$	Yaw angle rate of change vector	rad/s
ρ	Density of air or aircraft	$slug/ft^3$
Ω	von Kaman spatial frequency	rad/ft
σ_{w_g}	Gust velocity standard deviation	ft/s
Θ	Pitch angle	rad
$\dot{\Theta}$	Pitch angle rate of change	rad/s
$\dot{\vec{\Theta}}$	Pitch angle rate of change vector	rad/s
$\forall$	Volume	ft^3

TABLE OF CONTENTS

LIST OF TABLES

LIST OF FIGURES

1 INTRODUCTION

1.1 Problem Description

Turbulence is a substantial problem for general aviation aircraft. This disturbance creates financial problems for aircraft owners, in terms of structural damage or failure, and physical problems, such as motion sickness, for passengers and pilots alike. When an aircraft is attempting flight during a windy day, the pilot traditionally has three options available to him. First, do not fly; second, climb to altitudes above the turbulence, but where oxygen may be needed; or, finally, maintain altitude and slow down to reduce the severity of the loading on the vehicle. This problem becomes more significant for smaller general aviation aircraft, as they may not have the necessary power available to climb out of the turbulence. Due to their light wing loading, these aircraft will instead respond significantly to the turbulence, often making their passengers sick. This end result may be a contributing reason for the decline in the number of pilots who own and operate small general aviation aircraft in recent years. These problems have led past and present engineers to attempt to reduce the loads and accelerations of aircraft from turbulence via automated or inertial control surface deflections. A general term for this process is gust alleviation. As stated in a report by Human Factors Research Inc., "Man will continue to propel his body through water, air, and space with dynamics that are increasingly different from his normal body propulsion. Motion sickness research can contribute to the success of these ventures, as prediction leads to understanding, and understanding to control the ill effects of new dynamic environments." [1]

The research in this thesis was undertaken to assist ViGYAN Inc. in the development of its Active Ride Improvement System, or ARIS. The primary goal of this project is to make the modern general aviation aircraft more appealing to the average passenger. This program aims to use the latest technology in gust sensing and data processing, as well as a unique aerodynamic control system derived to achieve nearly an order of magnitude reduction in aircraft normal acceleration and pitch rate, when flying through turbulent wind fields.

A mathematical model of the vehicle to be used in study, the ARIS Flight Model version 1.5 or AFM 1.5, was created to simulate its dynamic responses to multiple sources of perturbations. Concepts such as distributed gust inputs for each lifting surface and unsteady aerodynamics were added to the math model for additional accuracy. As past researchers have been limited in their attempts at gust alleviation due to data processing speeds and servo deflection times, a transfer function for the forward gust sensor was generated and utilized during the linear simulations for added realism. The necessary gust flap command profile, including gains and a time delay, was then solved for. A step gust, doublet, and stochastic turbulence model, based on a favored power spectrum, were used as excitation inputs to the math model, in order to compare the vehicle's responses both with and without the gust alleviation system. Following the nominal analysis, the second elevator gain was tuned for additional alleviation in both normal acceleration and pitch rate.

1.2 Literature Review

This section will review important histories, theories, and methodologies relevant to the concepts on which this thesis is based. First, the concepts of turbulence and its natural and mathematical generation will be reviewed. Next, a brief history of previous attempts at gust alleviation, both successes and limitations, will be examined. Finally, the development of unsteady aerodynamics will also be reviewed.

1.2.1 Turbulence

Concern about an airplane's response to gust can be traced back to the very first report published by the National Advisory Committee for Aeronautics (NACA) titled "Report on Behavior of Aeroplanes in Gust." [2] A gust is defined as "A sudden, brief rush of wind." [3] Taken from an aeronautical engineer's standpoint, a gust load is defined as the change of angle of attack of an aircraft due to a gust velocity at a right angle to the flight path. [4] Wind gusts can be split into three categories: vertical, lateral and head on. For the purposes of this thesis, only vertical gusts will be considered. Vertical gusts affect the vehicle by causing it to pitch and plunge, where pitch is the rotational motion of the vehicle about the aircraft's lateral axis, and plunge is its vertical translational motion.

Turbulence is generally thought of as a continuous gust structure [4] and has been categorized into four intensities: light, moderate, severe, and extreme. [5] In light turbulence, passengers may feel a slight strain against seatbelts or shoulder straps; however, food service to the passengers will be carried on as normal and no difficulty will be encountered while they are walking about the cabin. [5] When

exposed to moderate turbulence, passengers will definitely feel strain against their shoulder straps, and unsecured objects may be dislodged. Food service to passengers and moving about the cabin may be difficult under this condition. If the vehicle undergoes severe turbulence, the occupants are forced violently against their shoulder straps, all food services are halted, unsecured objects are tossed about dangerously, and walking about the cabin can be near impossible. Finally, under extreme turbulence, the aircraft is violently tossed around and is nearly impossible to control. Structural damage to the aircraft may also occur. [5]

Before describing the methods for predicting dynamic air turbulence behavior, the sources of turbulence must be explained. Some of the main contributors to aerodynamic turbulence are wind shear, wake turbulence, and storms. [5] Wind shear itself can be broken down into three categories. The first is known as terrain mixing. This wind type is caused by the frictional shear from obstruction or irregularities on the ground. [6] The second type is named free wind shear; it is due to the vertical gradient of the wind profile. [5] Mountain waves make up the third type of wind shear turbulence; they are defined as oscillations to the lee side of high ground that result from the disturbance in the horizontal air flow caused by the high ground. [6] The length and the scale of these mountain waves depend on the mountain height, the wind speed, and the instability of the atmosphere. [6] Another source of turbulence is wake turbulence. This wind field evolves from the trailing vortices shed by the wings of an aircraft. This phenomenon is more of a problem for lighter aircraft than for heavier ones. When small, light aircrafts travel through the wake shed off of a larger

and heavier one, they have been known to not have sufficient roll power to overcome the aerodynamic forces that act on them from the resulting vortices, and they may roll to angles of up to 180 degrees. [5] Storms produce turbulence via the cold fronts that they produce, if the temperature difference across the face of the front is at least 10 degrees Fahrenheit, and the front is moving with a velocity of at least 30 knots. [6] Finally, temperature gradients themselves may cause wind shear and have been known to cause a 90 degree change in direction and up to a 30 knot increase in surface winds over merely a few minutes, in some areas of the southwest United States. [6]

When attempting to predict dynamic gust behavior in an engineering simulation, two primary methods historically have been used: the discrete gust concept and the continuous gust concept. Under the discrete gust concept, it is assumed that the airplane will be subjected to vertical gusts with a one minus cosine shape. [4] This method uses time history analyses to find solutions to the differential equations that describe the airplane's rigid and elastic mode responses to turbulence and thus predict the severity of the aircraft motion response to wind gusts. [4] This perspective was the dominant method for the Federal Aviation Regulations, FAR, gust load requirements until the mid-1960s, when Lockheed partnered with the Federal Aviation Authority (FAA), to publish a paper describing power spectral gust design procedures for general aviation aircraft. [4] Since then, the general consensus is that the continuous gust method is much more statistically accurate, so the discrete method is no longer required by the FAR or by the FAA, but it is still relevant to engineering analysis and design. The continuous gust concept assumes that

atmospheric turbulence can be described as a stationary Gaussian process. [4] This assumption is important because it describes the infinite number of ways in which an individual gust can be shaped. The Gaussian assumption is also significant because it allows the continuous gust concept to be analyzed via power spectrums. The most widely used shapes for these power spectrums were derived by von Karman and Dryden. [7] Power spectral analysis is beneficial in gust load studies, as the turbulence structure can be described in analytic form, utilizing frequency response analysis rather than simply a time history, which aids in identifying critical frequencies of response and amplification-attenuation levels. Also, the load response of airplanes to continuous rough air can be evaluated and then modified through configuration layout or control system changes to approach desirable response characteristics in continuous rough air, as defined by design requirements. [7] Based on the continuous gust assumption and the benefits of power spectral analysis, the power spectral density method for the deviation of airplane loads has been widely adopted. [8-12]

1.2.2 Gust Alleviation History

The contents of this thesis are not the first attempt at gust alleviation and will certainly not be the last. Some of the first work on this subject on record was completed by Bairstow and Nayler in 1913, when they computed the necessary elevator deflections to reduce an aircraft's response to head on gust. [13] However, this investigation was all analytical work with no experimentation. Roughly 25 years later, in 1940, Donely and Shufflebarger utilized NACA's newly opened gust tunnel

to perform the experimental test of a mass overbalanced wing flap. [14] With a rather simple system, they were able to achieve 39% reduction in normal acceleration. In 1950, the idea of utilizing gust sensing vanes to actuate full-span wing flaps and the elevator to alleviate normal acceleration by gusts was proposed by Ludwig. [15]

In the year 1951, after realizing the significant benefits of reducing accelerations and the possibility of improving passenger comfort, Phillips and Kraft published their paper entitled "Theoretical Study of Some Methods for Increasing Smoothness of Flight Through Rough Air." [16] They attempted three separate ways of reducing accelerations due to gust by using flaps only, elevator only, and a combination of the two, but they ultimately concluded that the third approach was the only effective option. Possibly the most significant contribution of their work to this thesis was the idea of splitting the airplane's force and moment stability derivatives into separate wing-body and tail components, which allowed for a distributed gust to excite the aircraft. They utilized steady sinusoidal gust disturbances at varying frequencies for the wind field input to their mathematical model. Limitations in their theory came by not including unsteady lift effects, due to their complexity. Although they did not include these effects in their equations of motion, they did note that unsteady effects become prominent at higher frequencies and they discussed the magnitudes those errors would cause. They mathematically achieved roughly 50% reduction of normal acceleration at 0.6 hertz and 40% reduction at 2 hertz. Following their mathematical development, Kraft applied their theory to a two-prop airplane flying at 150 miles per hour at an altitude of 2500 feet. [17] The

comparison of controls fixed and active cases proved their theoretical alleviation estimates to be correct.

In 1956, a thesis submitted to the University of Virginia, written by Norman Crabill, investigated the use of a mass overbalanced elevator to reduce the normal acceleration of a rocket boosted airplane flying at Mach 0.7, while also including indicial lift effects. [18] The underlying idea was to use a simple system to increase the damping ratio of the airframe by varying the viscous restraint of the elevator. Engineering analysis led to achieving an optimum increase in damping ratio, from 0.25 to 0.58. A 20% flat minimum normal acceleration reduction was mathematically achieved, along with a peak of 48% reduction at the airframe's natural short period frequency.

A more recent attempt at gust alleviation came about in the late 1970s to early 1980s under the Dornier Company. They created their open-loop gust alleviation, or OLGA, system with the intention to apply it to small general aviation aircraft to improve ride comfort. Before its application to a full-scale aircraft, they utilized a one-eighth scale model of the Dornier 28 for wind tunnel testing. This physical model was given two degrees of freedom, in the form of pitch and plunge. [19] After performing parameter identification to adjust their math model, they implemented symmetrically moving ailerons to eliminate gust lift and simultaneous elevator deflection to limit the pitching moment due to the gust and aileron deflection. Both of these movements were performed with respect to their forward gust sensor. Limitations in the effectiveness of alleviation originated from inaccuracy in stability

derivatives, degraded readings from the forward gust sensor, slow processor computing time, and low control surface deflection rates. Even with these limitations, their wind tunnel model achieved roughly 20 dB of vertical acceleration alleviation for the controls active, compared to the controls fixed cases. When the OLGA was applied to the full-scale Dornier 28, only about 10 dB reduction in vertical acceleration and 6 dB in pitch rate were achieved below two hertz. The intention was to implement this system on a full-scale production aircraft, the Donier 228, but this was never done, for unknown reasons.

Etkin, in his paper for the Wright Brothers Lectureship in Aeronautics in 1980, addresses a wide array of topics dealing with turbulent wind and its effect on aircraft flight, including historical developments, turbulent wind descriptions, aircraft system modeling with wind disturbances, motion prediction, passenger-pilot discomfort in turbulent air, and gust alleviation concepts. [20,21] He defines the major engineering concerns related to flight in turbulent-gust environments as vehicle structure strength, manual or automatic controllability, airframe structural fatigue, handling qualities, and passenger-crew comfort and safety. One important topic discussed by Etkin is the six-dimensional component modeling of translational and rotational gust velocities, and how the rotational components are approximated from a linearly varying spatial wind field, the so-called linear-field approximation. The simpler uniform-field approximation, or point gust model, in which the wind is spatially invariant, is also discussed. This simpler model is used in the thesis, but spatial or gust penetration effects, where forward components of the airframe

structure experience gust velocities before aftward components do, is accounted for by modeling thesis airframe components separately.

Rynaski and others at Calspan Corporation conducted a thorough investigation of various control law and performance criteria options for gust alleviation using engineering analysis and simulation. [22,23] Investigations were applied to a numeric model of the United States Air Force (USAF) – Calspan Total In-Flight Simulator (TIFS) research aircraft, including rigid body pitch and plunge degrees of freedom and up to five symmetric aeroelastic mode degrees of freedom controlled by elevator and direct lift flap surfaces. Systematic gust alleviation approaches based on matrix state space formulation were explored, using combined feedforward and feedback architectures to minimize turbulence effects, to address limited control availability, to trade control leverage on specific rigid body or aeroelastic motions, and to maintain stability with reduced sensitivity to flight condition. Reduction of root mean square accelerations of 50% or more were simultaneously achieved at various airframe locations and at various frequency ranges. Flight test results of these gust alleviation control strategies on the TIFS airframe are not fully reported on in the literature. [24]

Several development and test programs were considered, during the 1970s, to assess feasibility and to exploit the potential of the gust alleviation control system concept for large military and commercial jet aircraft. One major effort carried out by the USAF was the Load Alleviation and Mode Stabilization (LAMS) program. In this program, significant reductions in structural loads during flight through atmospheric

turbulence were achieved in B-52 and C-5A test aircraft. [25,26] From these early efforts, gust alleviation systems for large jet aircraft are commonplace for improving ride quality, load reduction, fatigue life, and performance, due to the larger but lighter wings and tail surfaces in commercial airliners and military transports, tankers, and strategic platforms. [27-29] Unfortunately, very little of this technology has been transferred to general aviation aircraft, which this thesis addresses.

Clear air turbulence at high altitude caused by mountain wave, thunderstorm wake, and thunderstorm updraft mechanisms poses special problems for aircraft flight. These large scale atmospheric disturbances, involving strong vortex or shear structures, are often unanticipated encounters that lead to severe loading, large motion transients, structural damage, and passenger-crew injury. [30,31] On-board forward looking lidar (light detection and ranging) sensors are one concept used for detecting these disturbances and for providing control lead for gust alleviation systems in high speed applications. Robinson considered the feasibility of such a system in an early study. [32] A more detailed investigation supported by NASA Langley Research Center was also conducted. [33] A significant reduction in aircraft loading and motion transients was predicted from this concept. For general aviation systems studied in this thesis with much lower speed, control lead is to be achieved by a mechanically mounted forward gust sensor.

1.2.3 Unsteady Aerodynamics Evolution

Many atmospheric flight problems are solved with the assumption of quasi-steady aerodynamics, or, in other words, the wake on the flow around an airfoil has

no effect on the lift [34], making the lift and moment responses of an aircraft to be steady, with respect to time, for a fixed aerodynamic angle. In flight, the presence of circulation on the lifting wing leaves a discontinuity in the form of vortices. [35] Due to the assumption that the wake is supposed to remain undistorted, the effects of different wakes are additive, permitting various flows to be built-up by superposition. [35] This concept is known as indicial, or unsteady, lift. One of the first pioneers of unsteady aerodynamic research was Herbert Wagner. His function, the Wagner function, allowed for the mathematical representation of the exponential build-up of lift on an airfoil, at a fixed angle of attack following a step input, at the quarter chord point, by solving for the downwash at the three-quarter chord point in the time domain. [36] This expression, however, was only valid for a step input, meaning that the airfoil would have to start at rest and asymptote to a uniform velocity. An important note of Wagner's function is the assumption that roughly half of the lift is present at the start of the build-up. Roughly a decade later, Theodore Theodorsen published his equations that describe the unsteady aerodynamics of self-excited sinusoidal motions of an airfoil by means of aerodynamic flutter. [37] He not only introduced the dependency of the unsteady lift effects on frequency, but he also contributed valuable research into the effects of a finite wing span and different section shapes. [37] These equations would prove to be the gateway into the derivation, by future researchers, of more complex analytical solutions to unsteady aerodynamic problems. Following the work of Wagner, Hans Georg Kussner developed a mathematical model to represent the unsteady lift of an airfoil caused by

a transverse gust. Sears and von Karman would build on Kussner's work by applying his theory to any arbitrary shape of penetrating gust. [38] R. T. Jones would then develop operational equivalents of these unsteady lift and gust effects for varying aspect ratios by correcting the aerodynamic inertia and the angle of attack of the infinite wing. These functions describe the growth of circulation in two-dimensional flow as a function of half chord lengths traveled from the lifting surface's leading edge.

1.3 Research Contributions

The thesis research contributes to the field of gust alleviation for general aviation in several ways. First, the research shows the effects that small-chord wing flaps, current data processors, and high speed control servos can attribute to the significant alleviation of normal acceleration and pitch rate due to turbulence. Second, the analytical nature of the research can expose key factors and subsystems that contribute to, or limit, the airframe motion alleviation, i.e., the parameter dependency or sensitivity, which can provide valuable insight for system design or modification. Third, the research can provide a theoretical performance baseline to compare the achieved flight performance against. Fourth, the knowledge gained from the research can guide the development and the implementation of an actual working system during ViGYAN's test flight phases of their AFM 1.5 flight model. Further, the control parameter and the delay time numerical values used in this study to achieve significant reductions can be used as starting points for flight trials.

2 BACKGROUND DATA

This chapter will review the relevant background data necessary for the analysis which follows. As this research is centered on a specific vehicle, the characteristics of its geometry, control surfaces, forward gust sensor, data processor, and assumed flight conditions will be explained in detail. The methodology for this particular gust alleviation system will also be explained. Reference frames and positive directions for certain variables are also defined here. Lastly, the wind fields to be input into the math model and their generation will also be discussed. Both deterministic and stochastic wind fields are considered. The stochastic wind is described in both the time and frequency domains, while the deterministic wind is given in time only.

2.1 Vehicle Characteristics

The vehicle used in the analysis contained in this thesis was a radio controlled (RC), one-eighth scale Pilatus Porter PC-6 aircraft, shown in Figures 2.1 - 2.2, and its planform, shown in Figure 2.3. This aircraft was named the AFM 1.5, or ARIS Flight Model 1.5, and is to be used for a proof of concept demonstration, after engineering analysis is completed. Flight testing is beyond the scope of this thesis. A PC-6 model was chosen, as it represents a small passenger general aviation aircraft. The aircraft layout is conventional, with forward main wing, aft horizontal and vertical tails, and single engine in the tractor configuration. The xyz frame indicated in Figure 2.3 has its origin located at the vehicle mass center, with x pointing out of the nose, y pointing out the right wing, and z pointing “down.” This frame moves and rotates with the

airframe. The overall dimensions and assumed flight conditions, at an altitude of 300 feet, of the one-eighth scale aircraft are given below, in Table 2.1. All variables are defined in the nomenclature list.

Table 2.1 AFM Flight Conditions and Reference Parameters

Flight Conditions	$V_{cm} = 58.667 \frac{ft}{s}$	$\rho = 2.377e-3 \frac{slug}{ft^3}$	$\mu = 3.738e-7 \frac{slug}{ft\ s}$
Aircraft Inertial Parameters	$x_{cm} = 0.2625\ ft$	$m = 0.3770\ slug$	$I_{yy} = 0.5352\ slug - ft^2$
Total Vehicle Reference Parameters	$\bar{s} = 5.34\ ft^2$	$\bar{c} = 0.833\ ft$	~
Wing Reference Parameters	$s_w = 5.34\ ft^2$	$c_w = 0.833\ ft$	$AR_w = 7.69$
Body Reference Parameters	$s_b = 1.72\ ft^2$	$c_b = 4.333\ ft$	$V_b = 1.013\ ft^3$
Tail Reference Parameters	$s_t = 1.23\ ft^2$	$c_t = 0.553\ ft$	$AR_t = 4.02$

The wings of the model utilized the NACA 2415 airfoil shape, while the tail was a flat plate. Control surfaces on the wing included inboard gust flaps alongside the traditional ailerons. The ailerons were modified so that when the gust alleviation system was turned on, they would act as flaps to aid the elimination of the wing lift created by gusts. Both the flaps and ailerons were small, in the sense that they are only ten percent of the chord length, with mechanical deflection limits of plus and minus 30 degrees. This small size is beneficial, in that their inertia properties are more favorable for quick deflections, and hinge moments may be neglected. The

propulsion system was a 1.5 horsepower electric motor and propeller, with batteries located ahead of the vehicle center of gravity. The lightweight construction of this model and the absence of a heavy concentrated payload in the cabin section yielded a larger scaled-up radius of gyration than would be expected on a full-scale model. The aircraft was also equipped with a forward gust sensor on the left wing, known as the J-Bird, shown in Figures 2.1 and 2.2. Being located one-half chord length ($\bar{c}$) ahead of the wing's leading edge allows the control surfaces, driven by the J-Bird output signal, to begin their first motion before the gust comes in contact with the wing. Also, the one-half chord length is sufficiently small to eliminate any significant vibrational effects.

Figure 2.1 ARIS Model 1.5

Figure 2.2 Forward Gust Sensor, a.k.a. The Bird

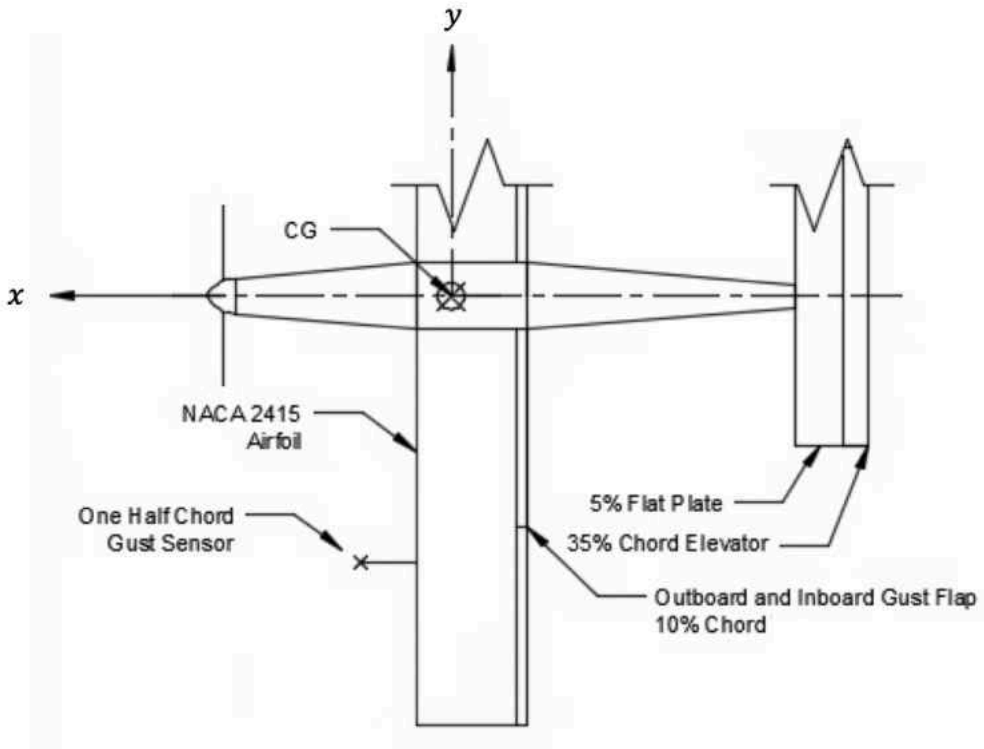

Figure 2.3 ARIS Planform

Six electric servos, Turnigy HV 380s, were installed on the model. Four servos were placed on the wing, one for each tailing edge control surface. The fifth servo would operate the elevator, and the sixth, the rudder. All six servos were equipped with proportional-integral-derivative controllers, which eliminated the unwanted effects of overshoot. These servos were capable of operating between 50 and 333 hertz. The on-board processor to be used in the test flights for gust alleviation is a Texas Instruments TIVA C Series. The automatic gust controller would read servo commands from the RC receiver, read the gust sensor signal, and write servo commands to the surface control servos. Both read and write servo commands utilized pulse width modulations, with pulse widths between 1 and 2 milliseconds, corresponding to the servo ranges of plus or minus 45 degrees. The time required to read the gust sensor was based on the data acquisition rate, which was capable of operating well above the maximum frequency of the servos. Due to the servo's limiting frequency, the engineering system model would be computed at 333 hertz for all linear simulations, corresponding to 3 millisecond time steps.

The gust alleviation system uses four parameters: three gains, one for the wing gust flap and two for the elevator, and the fourth parameter, which is the time difference for the second elevator motion, with respect to the first. A block diagram of this system is given in Figure 2.4. The flap gain, k_f, amplifies the J-Bird signal to create equal and opposite lift to that of the wing and the body response to the gust. The first elevator gain, k_{e1}, scales the J-Bird signal to equalize the combined moments created by the gust flap, along with the wing and body. The second elevator gain, k_{e2},

modifies the delayed J-Bird signal to eliminate the lift created on the tail by the gust. The time delay, Δ_t, for the second elevator motion was found by iteration. Table 2.2 shows the control law expressions.

The mechanics underlying the two steps of the gust alleviation control system are shown in the figures below. To minimize figure clutter, the body linear and angular displacements and rates are not shown, but note that they are in the same direction as that of the wing motion. Figure 2.5 shows the positive direction of the gust input. Figures 2.6 and 2.7 show the two steps of the gust alleviation command profile. In Figure 2.6, a positive unit gust velocity ($w_g = +1\frac{ft}{s}$) generates upward wing translational acceleration ($-Z_w$) and leading edge up wing rotational acceleration ($+M_w$). The control law correspondingly generates 1) an upward flap deflection ($-\delta_f$) that produces a canceling translational acceleration ($+Z_f$), and 2) a downward elevator deflection ($+\delta_e$) that produces a canceling rotational acceleration ($-M_e$) and translational acceleration ($-Z_e$). It is important to note that the lift and the moment created by the body are not included in Figure 2.6 for reasons of clutter, but their response acts in the same direction as the wing. In Figure 2.7 and after a small delay in time (Δ_t), the positive unit gust velocity generates tail accelerations ($-Z_t$ and $-M_t$), which are canceled by the control law generated accelerations ($+Z_e$ and $+M_e$) coming from an upward elevator deflection ($-\delta_e$).

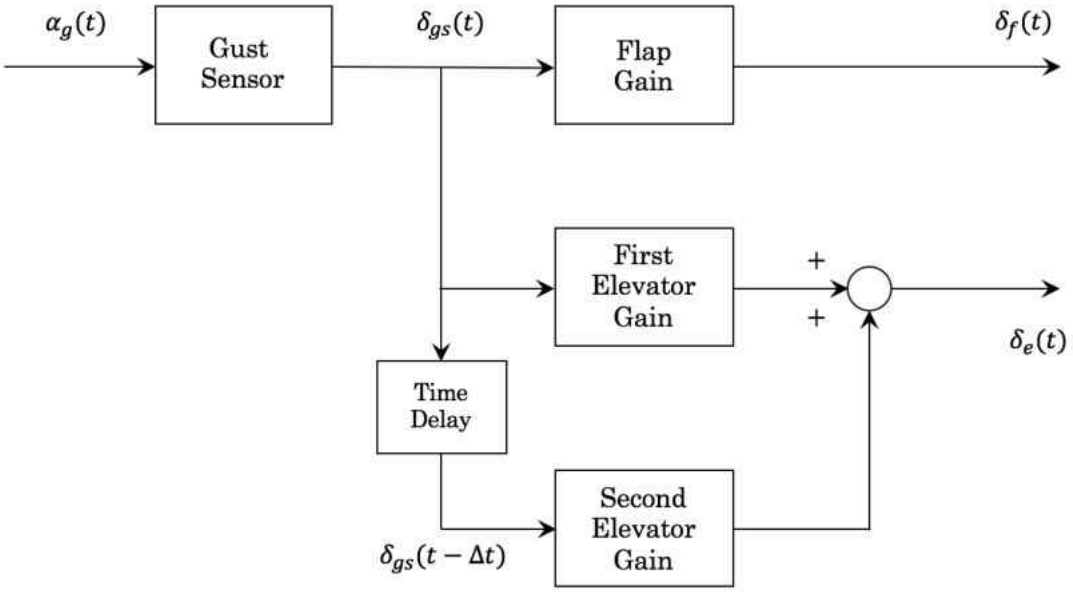

Figure 2.4 Gust Alleviation System

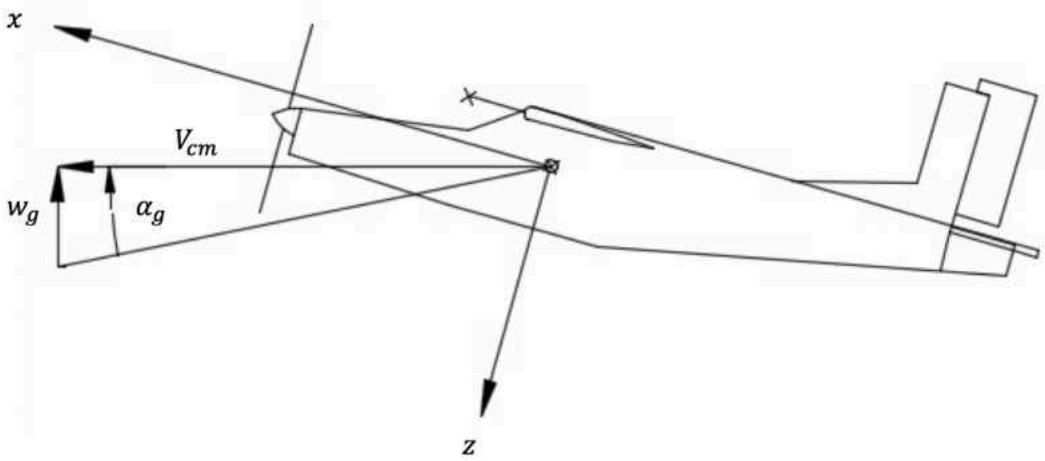

Figure 2.5 Gust Excitation

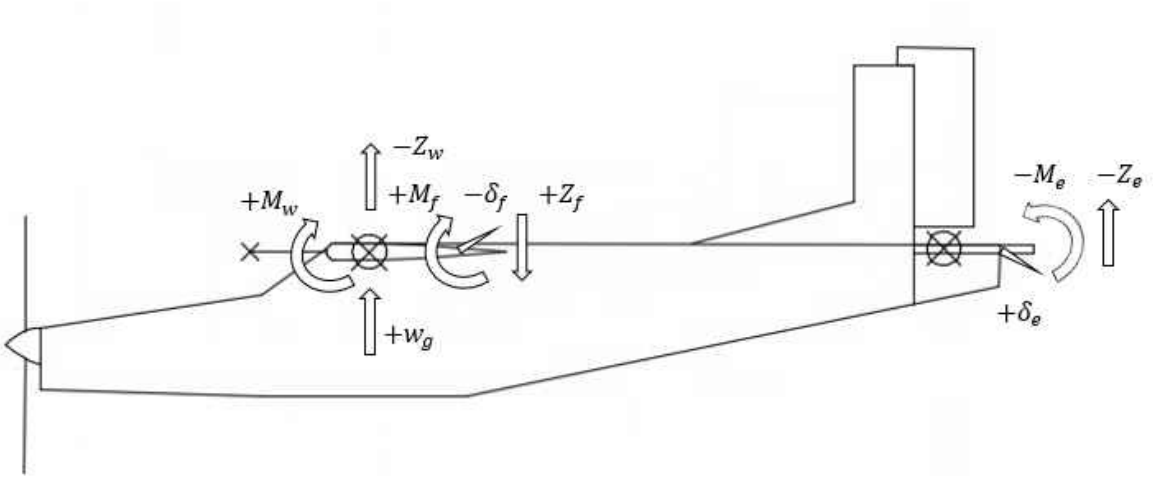

Figure 2.6 Control Law Stage 1

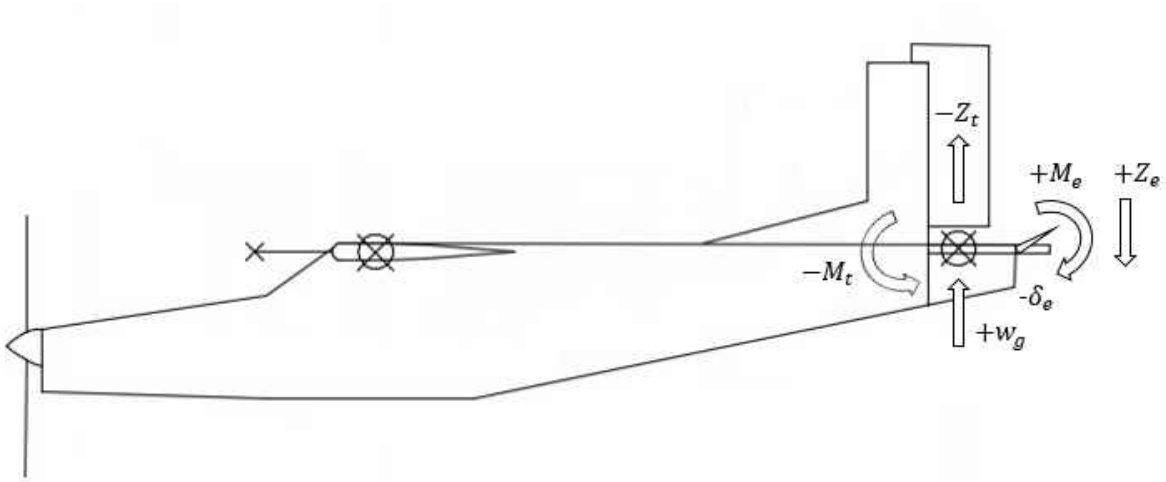

Figure 2.7 Control Law Stage 2

Table 2.2 Control Law Format

$\delta_{gs}(t) = -\alpha_g(t)$	$\delta_f(t) = k_f \delta_{gs}(t)$	$\delta_e(t) = k_{e1}\delta_{gs}(t) + k_{e2}\delta_{gs}(t - \Delta t)$

2.2 Input Wind Fields

This section will briefly review the three wind fields that were utilized as inputs to the math model.

2.2.1 Step Gust

A deterministic vertical step gust of three degrees, Figure 2.8, will be utilized as an input to the mathematical model, since the responses generated will be used to test the derived gains for the control surfaces, due to the reading of the forward gust sensor. The necessary time delay of the second elevator motion will also be solved from this wind field. Although this instantaneous gust change does not exist in nature, sharp vertical gradients in wind fields do exist, and the performance of the gust alleviation control system can be examined under this type of excitation. Note that the aircraft travel distance over this 0.7 second interval can be easily generated from the flight speed given in Table 2.1.

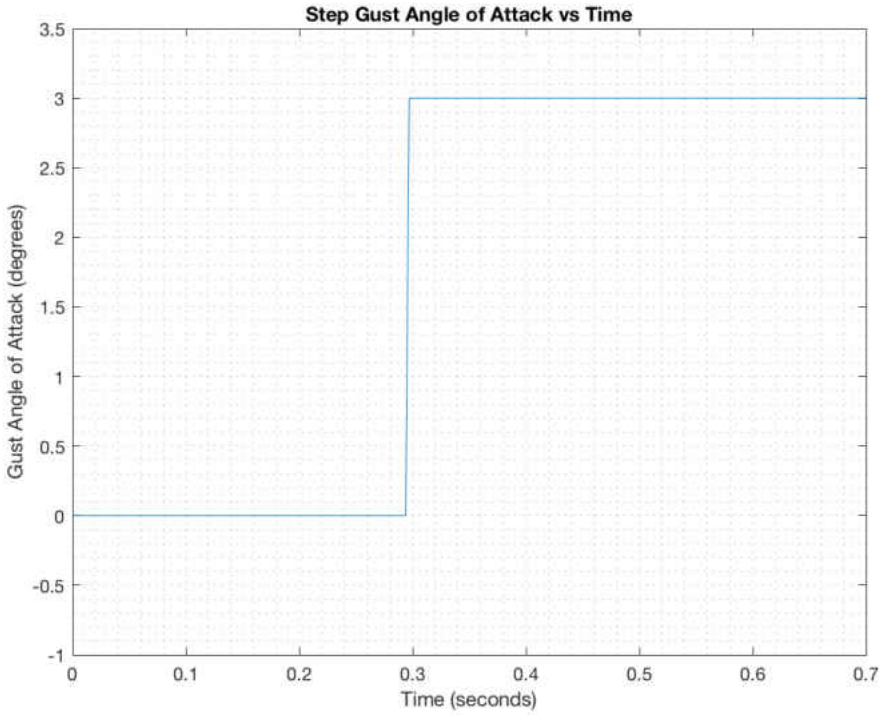

Figure 2.8 Step Gust Angle of Attack

2.2.2 Doublet Gust

A deterministic doublet gust angle of attack input, Figure 2.9, will test the AFM's reaction when the perturbation changes direction multiple times as a precursor to a stochastic environment. The amplitude changes between positive and negative 3 degrees. The doublet gust excitation also facilitates an important assessment of how the model responded when the control motion was not allowed to fully return to a steady state before additional excitation commences.

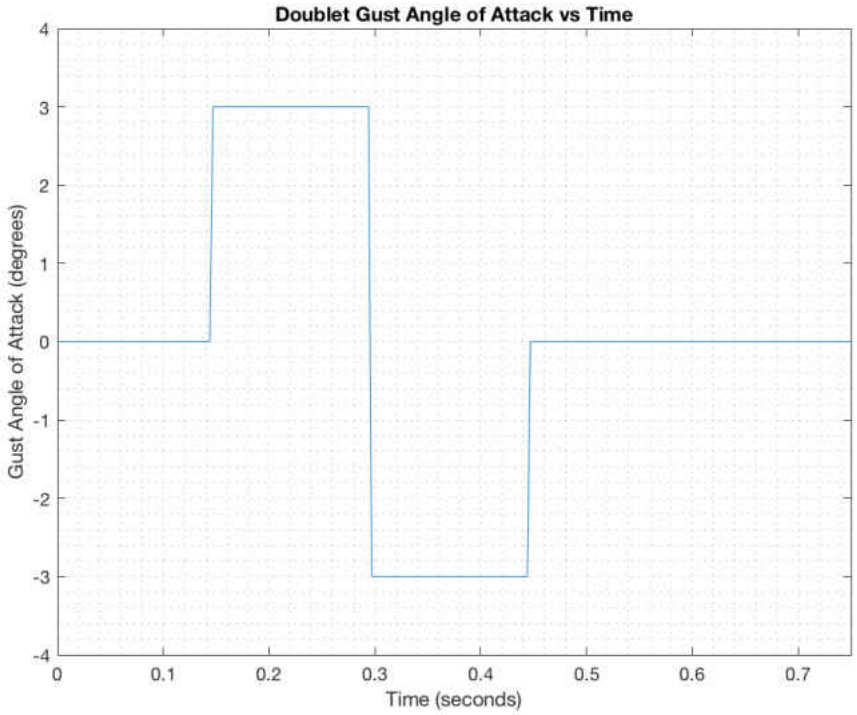

Figure 2.9 Doublet Gust Angle of Attack

2.2.3 von Karman Turbulence

The wind field used for the stochastic turbulence input was generated from the von Karman power spectrum. The von Karman power spectrum uses its own frequency, Ω, of radians per foot, and it differs from the Dryden spectrum in that its logarithmic decay slope is minus five thirds, whereas Dryden's is minus two. For a standard deviation of one foot per second gust velocity, the power spectrum is shown below, in Figure 2.10, for three different scale lengths.

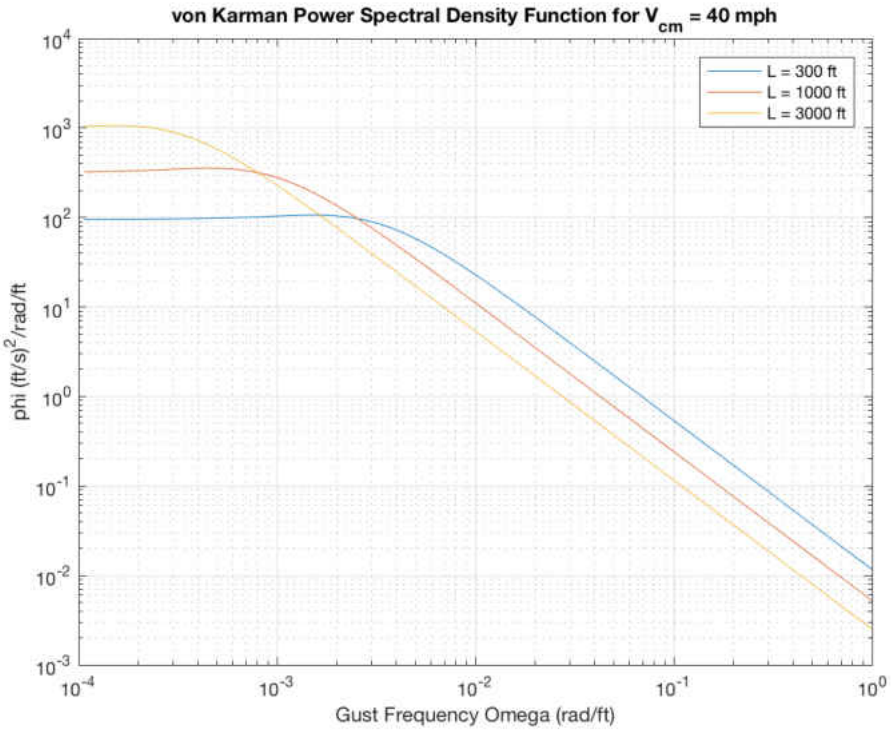

Figure 2.10 von Karman Function

From Figure 2.10, it can be seen that the magnitude of the vertical velocity depends on the scale length chosen. A previously derived approximate transfer function, Equation (2.2-1) [39], was used to generate a stochastic von Karman turbulence time history, as shown in Figure 2.11. White noise, $n(s)$, is used to excite the transfer function in Equation (2.2-1). The standard deviation of vertical gust velocity was selected as 2 feet per second and the scale length was taken as the anticipated flight altitude of 300 ft. The poles, zeros, and gain of the transfer function are given in Table 2.3. To accurately represent continuous, rather than discrete, time, the outputs of the gust velocity model in Equation (2.2-1) from linear simulation are multiplied, as shown in Equation (2.2-2), where "dt" represents the magnitude of the time step in the linear simulation. [39] As with the von Karman power spectrum,

inspection of the transfer function approximation poles, zeros, and gain shows dependence on scale length, vehicle velocity, and standard deviation of vertical gust velocity. Standard deviation, or root mean square, was calculated via Equation (2.2-3), where w_{g_i} is an individual sample value, $\overline{w}_g$ is the mean sample value, and N is the number of samples. For the time history in Figure 2.11, the computed standard deviation is 1.96 degrees per second, which agrees closely with the selected spectrum value of 2 degrees per second.

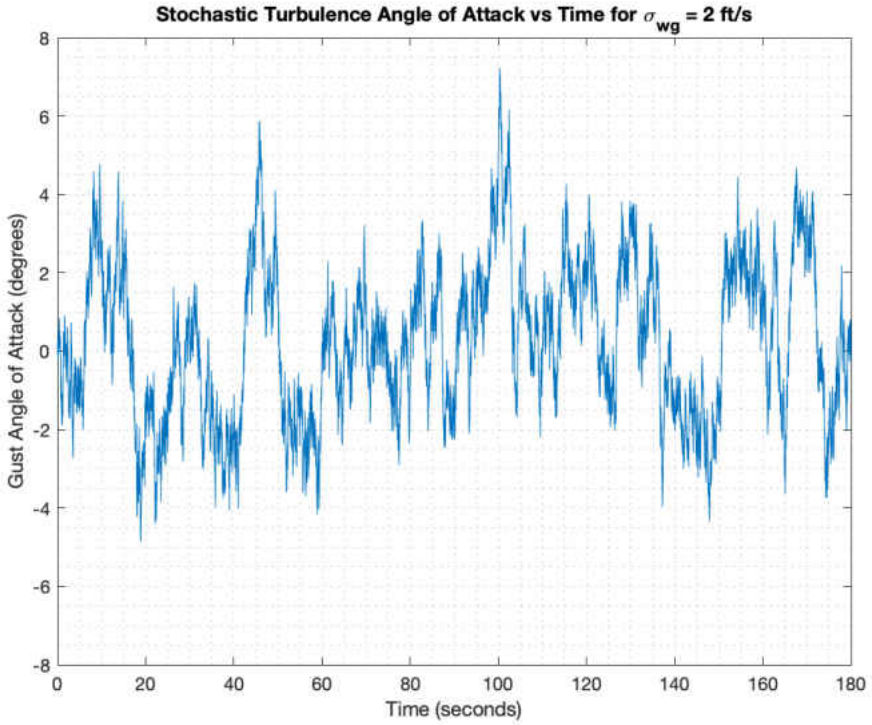

Figure 2.11 von Karman Generated Gust

$$\left(w_g(s)\right)_{discrete} = \frac{k(s+z_1)(s+z_2)}{(s+p_1)(s+p_2)(s+p_3)} n(s) \qquad (2.2\text{-}1)$$

Table 2.3 Stochastic Turbulence Transfer Function Poles, Zeros, and Gain

$k = 1.246\sigma_{w_g}\left(\frac{V_{cm}}{L}\right)^{\frac{1}{2}}$	$z_1 = 0.3820\frac{V_{cm}}{L}$	$z_2 = 7.704\frac{V_{cm}}{L}$
$p_1 = 0.4801\frac{V_{cm}}{L}$	$p_2 = 1.215\frac{V_{cm}}{L}$	$p_3 = 11.14\frac{V_{cm}}{L}$

$$w_g = \left(w_g\right)_{continuous} = \left(w_g\right)_{discrete}\sqrt{\frac{\pi}{dt}} \tag{2.2-2}$$

$$\sigma_{w_g} = \sqrt{\frac{1}{N}\sum_{i=1}^{N}(w_{g_i} - \bar{w}_g)^2} \tag{2.2-3}$$

3 THEORETICAL DEVELOPMENT

This chapter contains a rigorous development of the six dynamic equations of motion to describe an airplane's response to air perturbations. These equations will be set in a translating and rotating reference frame fixed to the aircraft, known as the body frame. Although only two of the six equations will be used, pitch and plunge, it is important to include the full development, so as to aid in future additions to this research. These two longitudinal equations will then be modified with an additional input for the gust, in terms of its angle of attack relative to the vehicle velocity vector. The necessary stability derivatives will be calculated for the AFM 1.5 vehicle, so that an analysis can be performed on it. In order to represent gust penetration effects, three separate gust inputs for the wing, body, and tail are created, and the corresponding component aerodynamic forces and moments are also kept separate in the model. The math model will then be put into state space form and the separate gust formulation will be verified via time history comparisons of a step input. To further enhance the accuracy of the model, indicial lift concepts will be appended to the state space form. Graphical transfer functions were created to compare the model both with and without indicial effects. Lastly, the necessary gains for the required control surface motions with respect to the forward gust sensor will be calculated.

3.1 Equations of Motion Derivation

The development of the aircraft's equations of motion begins by placing a translating and rotating reference frame on the aircraft, with its origin located at the center of mass and the inertial reference frame located on the Earth's assumed

stationary surface. The xyz aircraft centric frame was previously shown in Figures 2.2 and 2.4. A vector can then be drawn to any differential point mass on the aircraft, relative to the inertial origin. The position and velocity vector expressions are then given by Equations (3.1-1) and (3.1-2)

$$\vec{R} = \vec{R}_{cm} + \vec{r} \tag{3.1-1}$$

$$\vec{V}^I = \vec{V}^I_{cm} + \vec{v}^I \tag{3.1-2}$$

where

$$\vec{V}^I = \frac{d^I \vec{R}}{dt} \tag{3.1-3}$$

$$\vec{V}^I_{cm} = \frac{d^I \vec{R}_{cm}}{dt} \tag{3.1-4}$$

$$\vec{v}^I = \frac{d^I \vec{r}}{dt} \tag{3.1-5}$$

In these expressions, superscript "I" denotes a derivative with respect to the inertial frame.

From these definitions, the equations for continuous translational and angular momentum about the center of mass can be expressed.

$$\vec{G} = \int_B dm\vec{V}^I = m\vec{V}^I_{cm} \tag{3.1-6}$$

$$\vec{H}_{cm} = \int_B \vec{r} \times dm\vec{V}^I \tag{3.1-7}$$

The forces and moments acting on the aircraft are then defined as the time rate of change of translational and angular momentum, respectively, in the inertial frame of reference.

$$\vec{F} = \frac{d^I \vec{G}}{dt} \tag{3.1-8}$$

$$\vec{M} = \frac{d^I \vec{H}_{cm}}{dt} \tag{3.1-9}$$

To solve for the force equation, aerodynamic, gravitational, and thrust forces must be considered. Since force is the time rate of change of linear momentum in the inertial frame, the derivative is often expressed considering that the aircraft is in a moving reference frame. The derivative in a moving reference frame consists of the derivative in the body frame, denoted by the subscript "B", plus the angular velocity of the body frame with respect to the inertial frame cross multiplied with the original vector. This processing gives the force equation, with the assumption of constant mass, in vector notation.

$$\vec{F} = \vec{F}_g + \vec{F}_A + \vec{F}_T \tag{3.1-10}$$

$$\vec{F}_g + \vec{F}_A + \vec{F}_T = \frac{d^B \vec{G}}{dt} + \vec{\omega} \times \vec{G} \tag{3.1-11}$$

$$\vec{F}_A + \vec{F}_T + m\vec{g} = m\left(\frac{d^B \vec{V}^I{}_{cm}}{dt} + \vec{\omega} \times \vec{V}^I{}_{cm}\right) \tag{3.1-12}$$

The moment equation can be solved by taking a closer look at the angular momentum about the center of mass term. The differential mass can be replaced by the aircraft density multiplied by the differential volume. Then, substituting Equation (3.1-3) for the velocity of the differential mass term, and subsequently Equation (3.1-1) for the inertial position vector, reveals Equation (3.1-14).

$$\vec{H}_{cm} = \int_{\forall} \vec{r} \times \rho d\forall \left(\frac{d^I \vec{R}_{cm}}{dt} + \frac{d^I \vec{r}}{dt} \right) \tag{3.1-13}$$

$$\vec{H}_{cm} = \int_{\forall} \rho \vec{r} \times (\vec{\omega} \times \vec{r}) d\forall \tag{3.1-14}$$

By applying the derivative formula again, the moment vector Equation (3.1-15) results.

$$\begin{aligned} \vec{M}_A + \vec{M}_T = & \int_{\forall} \rho \vec{r} \times \left(\frac{d^B \vec{\omega}}{dt} \times \vec{r} \right) d\forall \\ & + \vec{\omega} \times \left[\int_{\forall} \rho \vec{r} \times (\vec{\omega} \times \vec{r}) d\forall \right] \end{aligned} \tag{3.1-15}$$

While these general vector equations are useful, they contain the six scalar equations needed to unlock the linear aircraft equations of motions. Each term in the two kinetic vector equations contains three components that represent their x, y, and z parts.

$$\vec{g} = g_x \hat{\imath} + g_y \hat{\jmath} + g_z \hat{k} \tag{3.1-16}$$

$$\vec{F}_A = F_{A_x} \hat{\imath} + F_{A_y} \hat{\jmath} + F_{A_z} \hat{k} \tag{3.1-17}$$

$$\vec{F}_T = F_{T_x}\hat{\imath} + F_{T_y}\hat{\jmath} + F_{T_z}\hat{k} \tag{3.1-18}$$

$$\vec{M}_A = L_A\hat{\imath} + M_A\hat{\jmath} + N_A\hat{k} \tag{3.1-19}$$

$$\vec{M}_T = L_T\hat{\imath} + M_T\hat{\jmath} + N_T\hat{k} \tag{3.1-20}$$

$$\vec{V}_{cm} = U\hat{\imath} + V\hat{\jmath} + W\hat{k} \tag{3.1-21}$$

$$\vec{\omega} = P\hat{\imath} + Q\hat{\jmath} + R\hat{k} \tag{3.1-22}$$

$$\vec{r} = x\hat{\imath} + y\hat{\jmath} + z\hat{k} \tag{3.1-23}$$

After plugging all of these terms into the vector equations, the six scalar and nonlinear coupled ordinary differential equations that govern the x, y, and z motions in translation and in rotation become available. Note that an inertially symmetric aircraft will be assumed henceforth, implying $I_{xy} = I_{yz} = 0$.

$$mg_x + F_{A_x} + F_{T_x} = m(\dot{U} + WQ - VR) \tag{3.1-24}$$

$$mg_y + F_{A_y} + F_{T_y} = m(\dot{V} + UR - WP) \tag{3.1-25}$$

$$mg_z + F_{A_z} + F_{T_z} = m(\dot{W} + VP - UQ) \tag{3.1-26}$$

$$L_A + L_T = I_{xx}\dot{P} - I_{zx}\dot{R} + \left(I_{zz} - I_{yy}\right)QR - I_{zx}PQ \tag{3.1-27}$$

$$M_A + M_T = I_{yy}\dot{Q} + (I_{xx} - I_{zz})RP + I_{zx}(P^2 - R^2) \tag{3.1-28}$$

$$N_A + N_T = I_{zz}\dot{R} - I_{zx}\dot{P} + \left(I_{yy} - I_{xx}\right)PQ + I_{zx}QR \tag{3.1-29}$$

These six equations, however, contain more than six unknowns. The aircraft angular rates, P, Q and R, being in the body axes, need to have three angles to specify

a general orientation of the aircraft, or its body frame. Define three Euler angles to represent the roll, pitch, and yaw angles of the aircraft in its body frame. The rotation rate equation then becomes

$$\vec{\omega} = \vec{\dot{\Psi}} + \vec{\dot{\Theta}} + \vec{\dot{\Phi}} \tag{3.1-30}$$

The transformation matrices relating P, Q, R to $\dot{\Psi}, \dot{\Theta}, \dot{\Phi}$ are derived in Reference [41].

$$\begin{bmatrix} P \\ Q \\ R \end{bmatrix} = \begin{bmatrix} 1 & 0 & 0 \\ 0 & cos\Phi & sin\Phi \\ 0 & -sin\Phi & cos\Phi \end{bmatrix} \begin{bmatrix} -sin\Theta\dot{\Psi} \\ 0 \\ cos\Theta\dot{\Psi} \end{bmatrix} + \begin{bmatrix} 0 \\ cos\Phi\dot{\Theta} \\ -sin\Phi\dot{\Theta} \end{bmatrix} + \begin{bmatrix} \dot{\Phi} \\ 0 \\ 0 \end{bmatrix} \tag{3.1-31}$$

The three kinematic equations are reduced to

$$P = -sin\Theta\dot{\Psi} + \dot{\Phi} \tag{3.1-32}$$

$$Q = sin\Phi cos\Theta\dot{\Psi} + cos\Phi\dot{\Theta} \tag{3.1-33}$$

$$R = cos\Phi cos\Theta\dot{\Psi} - sin\Phi\dot{\Theta} \tag{3.1-34}$$

One final step is to express the gravity components in terms of the Euler angles. After this step, Equations (3.1-35) through (3.1-40) reveal the six nonlinear equations of motion that describe flight dynamics, where Equations (3.1-32) – (3.1-34) are appended as additional and necessary scalar equations.

$$m\left(\dot{U} + QW - RV\right) = -mgsin\Theta + F_{A_x} + F_{T_x} \tag{3.1-35}$$

$$\dot{Q}I_{yy} - PR(I_{zz} - I_{xx}) + (P^2 - R^2)I_{zx} = M_A + M_T \tag{3.1-36}$$

$$m\left(\dot{W} + PV - QU\right) = mgcos\Phi cos\Theta + F_{A_z} + F_{T_z} \tag{3.1-37}$$

$$\dot{P}I_{xx} + QR\left(I_{zz} - I_{yy}\right) - \left(\dot{R} + PQ\right)I_{zx} = L_A + L_T \tag{3.1-38}$$

$$m\left(\dot{V} + RU - PW\right) = mgsin\Phi cos\Theta + F_{A_y} + F_{T_y} \tag{3.1-39}$$

$$\dot{R}I_{zz} + PQ\left(I_{yy} - I_{xx}\right) + \left(QR - \dot{P}\right)I_{zx} = N_A + N_T \tag{3.1-40}$$

For many flight applications, a linear approach is sufficiently accurate and can drastically simplify the analysis. This method has been known to give results for stability and control responses accurate enough for engineering purposes. The linearization process begins with the concept of perturbed flight. Perturbed flight can be thought of as small deviations from a steady rectilinear flight path. This method of analysis begins by considering all of the variables to be given by their steady state value with the addition of a perturbed value. The linear and angular perturbed velocities, and their derivatives, along with perturbed angles, forces, and moments, will be denoted with the lower case values of their original letter or symbol. All steady state values will be represented with the subscript "1." Equations (3.1-3.5) – (3.1-40) become

$$\begin{aligned} m\left(\left(\dot{U}_1 + \dot{u}\right) + (Q_1 + q)(W_1 + w) - (R_1 + r)(V_1 + v)\right) \\ = -mgsin(\Theta_1 + \theta) + F_{A_{x_1}} + f_{A_x} + F_{T_{x_1}} + f_{T_x} \end{aligned} \tag{3.1-41}$$

$$\begin{aligned} \left(\dot{Q}_1 + \dot{q}\right)I_{yy} - (P_1 + p)(R_1 + r)(I_{zz} - I_{xx}) \\ + ((P_1 + p)^2 - (R_1 + r)^2)I_{zx} \\ = M_{A_1} + m_A + M_{T_1} + m_T \end{aligned} \tag{3.1-42}$$

$$m\left(\left(\dot{W}_1 + w\right) + (P_1 + p)(V_1 + v) - (Q_1 + q)(U_1 + u)\right) = mgcos(\Phi_1 + \varphi)\cos(\Theta_1 + \theta) + F_{A_{z_1}} + f_{A_z} + F_{T_{z_1}} + f_{T_z} \quad (3.1\text{-}43)$$

$$\left(\dot{P}_1 + \dot{p}\right)I_{xx} + (Q_1 + q)(R_1 + r)\left(I_{zz} - I_{yy}\right) - \left(\left(\dot{R}_1 + \dot{r}\right) + (P_1 + p)(Q_1 + q)\right)I_{zx} = L_{A_1} + l_A + L_{T_1} + l_T \quad (3.1\text{-}44)$$

$$m\left(\left(\dot{V}_1 + \dot{v}\right) + (R_1 + r)(U_1 + u) - (P_1 + p)(W_1 + w)\right) = mgsin(\Phi_1 + \varphi)\cos(\Theta_1 + \theta) + F_{A_{y1}} + f_{A_y} + F_{T_{y1}} + f_{T_y} \quad (3.1\text{-}45)$$

$$\left(\dot{R}_1 + \dot{r}\right)I_{zz} + (P_1 + p)(Q_1 + q)\left(I_{yy} - I_{xx}\right) + \left((Q_1 + q)(R_1 + r) - \left(\dot{P}_1 + \dot{p}\right)\right)I_{zx} = N_{A_1} + n_A + N_{T_1} + n_T \quad (3.1\text{-}46)$$

The six equations above are able to describe full six degree of freedom flight mechanics, since no simplifications have been made. For steady wings-level rectilinear flight, this level of complexity is not necessary. The following simplifications will be applied. First, many steady state values are zero for symmetric straight-line equilibrium, and those that are non-zero are cancelled from the equations, leaving only the perturbed force, moment, and acceleration terms. Second, the small angle assumption will be applied, where trigonometric functions for angles that yield very small values, as well as any terms they are multiplied with, will be considered negligible. Upon applying these simplifications and dropping any

remaining higher order terms, the six degree of freedom equations are reduced to the following linear form.

$$m\dot{u} = -mg\theta cos\Theta_1 + f_{A_x} + f_{T_x} \tag{3.1-47}$$

$$I_{yy}\dot{q} = m_A + m_T \tag{3.1-48}$$

$$m(\dot{w} - U_1 q) = -mg\theta sin\Theta_1 + f_{A_z} + f_{T_z} \tag{3.1-49}$$

$$I_{xx}\dot{p} - I_{zx}\dot{r} = l_A + l_T \tag{3.1-50}$$

$$m(\dot{v} + U_1 r) = mg\Phi cos\Theta_1 + f_{A_y} + f_{T_y} \tag{3.1-51}$$

$$I_{zz}\dot{r} - I_{xz}\dot{p} = n_A + n_T \tag{3.1-52}$$

To continue the mathematical derivation of the wings-level rectilinear flight model, the aerodynamic perturbed forces and moments must be determined. To do this, treat the forces and moments as functions of relevant full nonlinear variables, which are Taylor series expanded and truncated. Note that the symbols $\alpha, \beta, \delta_e, \delta_f . \delta_a, \delta_r$ in the expressions below represent linear perturbed variables.

$$F_{A_x}, M_A, F_{A_z} = f(U, \alpha, \dot{\alpha}, Q, \delta_e, \delta_f) \tag{3.1-53}$$

$$L_A, F_{A_y}, N_A = (\beta, \dot{\beta}, P, R, \delta_a, \delta_r) \tag{3.1-54}$$

$$f_{A_x} = \frac{\partial F_{A_x}}{\partial u}u + \frac{\partial F_{A_x}}{\partial \alpha}\alpha + \frac{\partial F_{A_x}}{\partial \dot{\alpha}}\dot{\alpha} + \frac{\partial F_{A_x}}{\partial q}q + \frac{\partial F_{A_x}}{\partial \delta_e}\delta_e + \frac{\partial F_{A_x}}{\partial \delta_f}\delta_f \tag{3.1-55}$$

$$m_A = \frac{\partial M_A}{\partial u}u + \frac{\partial M_A}{\partial \alpha}\alpha + \frac{\partial M_A}{\partial \dot{\alpha}}\dot{\alpha} + \frac{\partial M_A}{\partial q}q + \frac{\partial M_A}{\partial \delta_e}\delta_e + \frac{\partial M_A}{\partial \delta_f}\delta_f \tag{3.1-56}$$

$$f_{A_z} = \frac{\partial F_{A_z}}{\partial u}u + \frac{\partial F_{A_z}}{\partial \alpha}\alpha + \frac{\partial F_{A_z}}{\partial \dot{\alpha}}\dot{\alpha} + \frac{\partial F_{A_z}}{\partial q}q + \frac{\partial F_{A_z}}{\partial \delta_e}\delta_e + \frac{\partial F_{A_z}}{\partial \delta_f}\delta_f \tag{3.1-57}$$

$$l_A = \frac{\partial L_A}{\partial \beta}\beta + \frac{\partial L_A}{\partial \dot{\beta}}\dot{\beta} + \frac{\partial L_A}{\partial p}p + \frac{\partial L_A}{\partial r}r + \frac{\partial L_A}{\partial \delta_a}\delta_a + \frac{\partial L_A}{\partial \delta_r}\delta_r \tag{3.1-58}$$

$$f_{A_y} = \frac{\partial F_{A_y}}{\partial \beta}\beta + \frac{\partial F_{A_y}}{\partial \dot{\beta}}\dot{\beta} + \frac{\partial F_{A_y}}{\partial p}p + \frac{\partial F_{A_y}}{\partial r}r + \frac{\partial F_{A_y}}{\partial \delta_a}\delta_a + \frac{\partial F_{A_y}}{\partial \delta_r}\delta_r \tag{3.1-59}$$

$$n_A = \frac{\partial N_A}{\partial \beta}\beta + \frac{\partial N_A}{\partial \dot{\beta}}\dot{\beta} + \frac{\partial N_A}{\partial p}p + \frac{\partial N_A}{\partial r}r + \frac{\partial N_A}{\partial \delta_a}\delta_a + \frac{\partial N_A}{\partial \delta_r}\delta_r \tag{3.1-60}$$

Following Yechout [40], these equations can be converted to dimensional stability derivative form, so they may be used for comparisons and to allow for the insertion of non-dimensional stability derivative numerical data. After this process is complete, the following linear dynamic model, Equations (3.1-61) - (3.1-66), is revealed. Note that thrust force and moment terms have been dropped, implying that thrust is constant and that throttle inputs will not be used, henceforth. Also note that certain aerodynamic dependencies have also been dropped.

$$\dot{u} = -g\theta cos\Theta_1 + X_u u + X_\alpha \alpha + X_{\delta_f}\delta_f \tag{3.1-61}$$

$$\dot{w} - U_1 q = -g\theta sin\Theta_1 + Z_\alpha \alpha + Z_{\dot{\alpha}}\dot{\alpha} + Z_q q + Z_{\delta_e}\delta_e + Z_{\delta_f}\delta_f \tag{3.1-62}$$

$$\dot{q} = M_\alpha \alpha + M_{\dot{\alpha}}\dot{\alpha} + M_q q + M_{\delta_e}\delta_e + M_{\delta_f}\delta_f \tag{3.1-63}$$

$$\dot{v} + U_1 r = g\varphi cos\Theta_1 + Y_\beta \beta + Y_p p + Y_r r + Y_{\delta_a}\delta_a + Y_{\delta_r}\delta_r \tag{3.1-64}$$

$$\dot{p} - \frac{I_{xz}}{I_{xx}}\dot{r} = L_\beta \beta + L_p p + L_r r + L_{\delta_a}\delta_a + L_{\delta_r}\delta_r \tag{3.1-65}$$

$$\dot{r} - \frac{I_{xz}}{I_{zz}}\dot{p} = N_\beta \beta + N_p p + N_r r + N_{\delta_a}\delta_a + N_{\delta_r}\delta_r \tag{3.1-66}$$

Due to the fact that only vertical gusts will be considered, only longitudinal dynamics will be considered for the remainder of the analysis. The math model is therefore further reduced to a two degree of freedom pitch-plunge model, Equations (3.1-62) and (3.1-63), in order to focus on the short period dynamics. The main variables that contribute to these dynamics are angle of attack and pitch rate changes. This reduction means that a constant forward velocity assumption is made, yielding the longitudinal equation for perturbed forward velocity to be trivially zero. The remaining two equations are shown below, with the substitutions, in Table 3.1.

Table 3.1 Pitch-Plunge Model Assumptions

$U_1 = V_{cm}$	$\dot{w} = \dot{\alpha} V_{cm}$	$sin\Theta_1 = 0$

$$\dot{\alpha} V_{cm} - V_{cm} q = Z_\alpha \alpha + Z_{\dot{\alpha}} \dot{\alpha} + Z_q q + Z_{\delta_e} \delta_e + Z_{\delta_f} \delta_f \tag{3.1-67}$$

$$\dot{q} = M_\alpha \alpha + M_{\dot{\alpha}} \dot{\alpha} + M_q q + M_{\delta_e} \delta_e + M_{\delta_f} \delta_f \tag{3.1-68}$$

As angle of attack and pitch rate are to be the state variables, their equations were rearranged to solve for their derivatives. The lift equation was simply manipulated to solve for $\dot{\alpha}$, Equation (3.1-69). The moment equation was slightly more complicated, in that it originally contained the derivatives of both state variables, since the unsteady effects through $\dot{\alpha}$ have been retained. To modify the equation to contain only one variable derivative, Equation (3.1-69) was substituted into Equation (3.1-68) for its alpha derivative. After this substitution, the relation

could be rearranged to form Equation (3.1-70). Note that the disturbance gust angle of attack has been added to the appropriate terms.

$$\dot{\alpha} = \left(\frac{Z_\alpha}{V_{cm} - Z_{\dot{\alpha}}}\right)(\alpha + \alpha_g) + \left(\frac{V_{cm} + Z_q}{V_{cm} - Z_{\dot{\alpha}}}\right) q + \left(\frac{Z_{\delta_e}}{V_{cm} - Z_{\dot{\alpha}}}\right) \delta_e + \left(\frac{Z_{\delta_f}}{V_{cm} - Z_{\dot{\alpha}}}\right) \delta_f \tag{3.1-69}$$

$$\dot{q} = \left[M_\alpha + \left(\frac{M_{\dot{\alpha}} Z_\alpha}{V_{cm} - Z_{\dot{\alpha}}}\right)\right](\alpha + \alpha_g) + \left[M_q + M_{\dot{\alpha}}\left(\frac{V_{cm} + Z_q}{V_{cm} - Z_{\dot{\alpha}}}\right)\right] q + \left[M_{\delta_e} + \left(\frac{M_{\dot{\alpha}} Z_{\delta_e}}{V_{cm} - Z_{\dot{\alpha}}}\right)\right] \delta_e + \left[M_{\delta_f} + \left(\frac{M_{\dot{\alpha}} Z_{\delta_f}}{V_{cm} - Z_{\dot{\alpha}}}\right)\right] \delta_f \tag{3.1-70}$$

When the one-eighth scale model is flying at 40 miles per hour, a unit step gust will have passed along the entire length of the vehicle in roughly 80 milliseconds. Since a three millisecond simulation time step is utilized, gust penetration effects, where different parts of the airframe experience different gusts, should be modeled. In other words, a single gust input acting at the aircraft's center of gravity will be converted to individual gusts acting on the airframe components. Therefore, the alpha gust input to the model was split into a component for each lifting surface, i.e., the wing, body, and tail, yielding Equations (3.1-71) and (3.1-72). These equations were subsequently put into state space form, as seen in Equation (3.1-73), with the matrix element constants given in Table 3.2. The state space equation with outputs $\alpha, q,$ and normal load factor n_z is also shown in Equation (3.1-74).

$$\dot{\alpha} = \left(\frac{Z_\alpha}{V_{cm} - Z_{\dot{\alpha}}}\right)\alpha + \left(\frac{V_{cm} + Z_q}{V_{cm} - Z_{\dot{\alpha}}}\right)q + \left(\frac{Z_{\delta_e}}{V_{cm} - Z_{\dot{\alpha}}}\right)\delta_e + \left(\frac{Z_{\delta_f}}{V_{cm} - Z_{\dot{\alpha}}}\right)\delta_f + \left(\frac{Z_{\alpha_w}}{V_{cm} - Z_{\dot{\alpha}}}\right)\alpha_{g_w} + \left(\frac{Z_{\alpha_b}}{V_{cm} - Z_{\dot{\alpha}}}\right)\alpha_{g_b} + \left(\frac{Z_{\alpha_t}}{V_{cm} - Z_{\dot{\alpha}}}\right)\alpha_{g_t} \tag{3.1-71}$$

$$\dot{q} = \left[M_\alpha + \left(\frac{M_{\dot{\alpha}} Z_\alpha}{V_{cm} - Z_{\dot{\alpha}}}\right)\right]\alpha + \left[M_q + M_{\dot{\alpha}}\left(\frac{V_{cm} + Z_q}{V_{cm} - Z_{\dot{\alpha}}}\right)\right]q + \left[M_{\delta_e} + \left(\frac{M_{\dot{\alpha}} Z_{\delta_e}}{V_{cm} - Z_{\dot{\alpha}}}\right)\right]\delta_e + \left[M_{\delta_f} + \left(\frac{M_{\dot{\alpha}} Z_{\delta_f}}{V_{cm} - Z_{\dot{\alpha}}}\right)\right]\delta_f + \left[M_{\alpha_w} + \left(\frac{M_{\dot{\alpha}} Z_{\alpha_w}}{V_{cm} - Z_{\dot{\alpha}}}\right)\right]\alpha_{g_w} + \left[M_{\alpha_b} + \left(\frac{M_{\dot{\alpha}} Z_{\alpha_b}}{V_{cm} - Z_{\dot{\alpha}}}\right)\right]\alpha_{g_b} + \left[M_{\alpha_t} + \left(\frac{M_{\dot{\alpha}} Z_{\alpha_t}}{V_{cm} - Z_{\dot{\alpha}}}\right)\right]\alpha_{g_t} \tag{3.1-72}$$

$$\begin{bmatrix}\dot{\alpha}\\ \dot{q}\end{bmatrix} = \begin{bmatrix}A_{11} & A_{12}\\ A_{21} & A_{22}\end{bmatrix}\begin{bmatrix}\alpha\\ q\end{bmatrix} + \begin{bmatrix}B_{11} & B_{12} & B_{13} & B_{14} & B_{15}\\ B_{21} & B_{22} & B_{23} & B_{24} & B_{25}\end{bmatrix}\begin{bmatrix}\delta_e\\ \delta_f\\ \alpha_{g_w}\\ \alpha_{g_b}\\ \alpha_{g_t}\end{bmatrix} \tag{3.1-73}$$

$$\begin{bmatrix}\alpha\\ q\\ n_z\end{bmatrix} = \begin{bmatrix}1 & 0\\ 0 & 1\\ \frac{V_{cm}}{g}A_{11} & \frac{V_{cm}}{g}(A_{12} - 1)\end{bmatrix}\begin{bmatrix}\alpha\\ q\end{bmatrix} + \begin{bmatrix}0 & 0 & 0 & 0 & 0\\ 0 & 0 & 0 & 0 & 0\\ B_{11}\frac{V_{cm}}{g} & B_{12}\frac{V_{cm}}{g} & B_{13}\frac{V_{cm}}{g} & B_{14}\frac{V_{cm}}{g} & B_{15}\frac{V_{cm}}{g}\end{bmatrix}\begin{bmatrix}\delta_e\\ \delta_f\\ \alpha_{g_w}\\ \alpha_{g_b}\\ \alpha_{g_t}\end{bmatrix} \tag{3.1-74}$$

Table 3.2 Constants for Equations (3.1-73) – (3.1-74)

$A_{11} = \left(\frac{Z_\alpha}{V_{cm} - Z_{\dot{\alpha}}}\right)$	$A_{12} = \left(\frac{V_{cm} + Z_q}{V_{cm} - Z_{\dot{\alpha}}}\right)$	$A_{21} = M_\alpha + \left(\frac{M_{\dot{\alpha}} Z_\alpha}{V_{cm} - Z_{\dot{\alpha}}}\right)$
$A_{22} = M_q + M_{\dot{\alpha}}\left(\frac{V_{cm} + Z_q}{V_{cm} - Z_{\dot{\alpha}}}\right)$	$B_{11} = \left(\frac{Z_{\delta_e}}{V_{cm} - Z_{\dot{\alpha}}}\right)$	$B_{12} = \left(\frac{Z_{\delta_f}}{V_{cm} - Z_{\dot{\alpha}}}\right)$
$B_{13} = \left(\frac{Z_{\alpha_w}}{V_{cm} - Z_{\dot{\alpha}}}\right)$	$B_{14} = \left(\frac{Z_{\alpha_b}}{V_{cm} - Z_{\dot{\alpha}}}\right)$	$B_{15} = \left(\frac{Z_{\alpha_t}}{V_{cm} - Z_{\dot{\alpha}}}\right)$

$B_{21} = M_{\delta_e} + \left(\frac{M_{\dot{\alpha}} Z_{\delta_e}}{V_{cm} - Z_{\dot{\alpha}}}\right)$	$B_{22} = M_{\delta_f} + \left(\frac{M_{\dot{\alpha}} Z_{\delta_f}}{V_{cm} - Z_{\dot{\alpha}}}\right)$	$B_{23} = M_{\alpha_w} + \left(\frac{M_{\dot{\alpha}} Z_{\alpha_w}}{V_{cm} - Z_{\dot{\alpha}}}\right)$
$B_{24} = M_{\alpha_b} + \left(\frac{M_{\dot{\alpha}} Z_{\alpha_b}}{V_{cm} - Z_{\dot{\alpha}}}\right)$	$B_{25} = M_{\alpha_t} + \left(\frac{M_{\dot{\alpha}} Z_{\alpha_t}}{V_{cm} - Z_{\dot{\alpha}}}\right)$	

3.2 Stability Derivative Calculations

Before linear simulations were run, the stability derivatives for the AFM 1.5 needed to be calculated, starting with their non-dimensional lift and moment coefficients. The constants in Table 3.3 would be used for the aerodynamic coefficients in Equations (3.2-1) through (3.2-18). Following this data, Table 3.4 shows the conversion from non-dimensional stability derivatives to dimensional stability derivatives, which appear in the state space matrices indicated in Table 3.2. All aerodynamic centers were measured from the wing's leading edge.

Table 3.3 Constants for Aerodynamic Coefficients

Wing	$C_{L_\alpha} = 0.1097 \frac{1}{deg}$	$x_{ac_w} = 0.2083\ ft$	$e_w = 0.93$
Body	$x_{ac_b} = -0.141\ ft$	$s_{b_c} = 0.3333\ in^2$	$k_b = 0.93$
Tail	$x_{ac_t} = 2.972\ ft$		$e_t = 0.98$
Flap	$x_{cp_f} = 0.4167\ ft$		$\epsilon_f = 0.25$
Elevator	$x_{cp_e} = 3.113\ ft$		$\epsilon_e = 0.64$

$$C_{L_{\alpha_w}} = \frac{C_{L_\alpha}}{1 + \frac{57.3\ C_{L_\alpha}}{\pi e_w AR_w}} = 0.0857\ \frac{1}{deg} \tag{3.2-1}$$

$$C_{M_{\alpha_w}} = \frac{s_w}{\bar{s}} \frac{x_{cm} - x_{ac_w}}{\bar{c}} C_{L_{\alpha_w}} = 0.0056 \ \frac{1}{deg} \tag{3.2-2}$$

$$C_{L_{\alpha_b}} = \frac{2k_b s_{b_c}}{V_b^{2/3}} \frac{\pi}{180} = 0.0107 \ \frac{1}{deg} \tag{3.2-3}$$

$$C_{M_{\alpha_b}} = \frac{s_b}{\bar{s}} \frac{x_{cm} - x_{ac_b}}{\bar{c}} C_{L_{\alpha_b}} = 0.0017 \ \frac{1}{deg} \tag{3.2-4}$$

$$\varepsilon_{DW} = \frac{2C_{L_w}}{180 AR_w} = 0.4065 \tag{3.2-5}$$

$$C_{L_{\alpha_t}} = \frac{C_{L_\alpha}(1 - \varepsilon_{DW})}{1 + \frac{57.3 \ C_{L_\alpha}}{\pi e_t AR_t}} = 0.0432 \ \frac{1}{deg} \tag{3.2-6}$$

$$C_{M_{\alpha_t}} = \frac{s_t}{\bar{s}} \frac{x_{cm} - x_{ac_t}}{\bar{c}} C_{L_{\alpha_t}} = -0.0323 \ \frac{1}{deg} \tag{3.2-7}$$

$$C_{L_{\delta_f}} = \frac{s_w}{\bar{s}} \epsilon_f C_{L_{\alpha_w}} = 0.0214 \ \frac{1}{deg} \tag{3.2-8}$$

$$C_{M_{\delta_f}} = \frac{s_w}{\bar{s}} \epsilon_f \left(x_{cm} - x_{cp_f}\right) C_{L_{\alpha_w}} = -0.0040 \ \frac{1}{deg} \tag{3.2-9}$$

$$C_{L_{\delta_e}} = \frac{s_t}{\bar{s}} \epsilon_e \frac{C_{L_\alpha}}{1 + \frac{57.3 \ C_{L_\alpha}}{\pi e_t AR_t}} = 0.0107 \ \frac{1}{deg} \tag{3.2-10}$$

$$C_{M_{\delta_e}} = \frac{s_t}{\bar{s}} \epsilon_e \frac{C_{L_\alpha}}{1 + \frac{57.3 \ C_{L_\alpha}}{\pi e_t AR_t}} \left(x_{cm} - x_{cp_e}\right) = -0.0367 \ \frac{1}{deg} \tag{3.2-11}$$

$$x_{ac} = \frac{\frac{s_w}{\bar{s}} C_{L_{\alpha_w}} x_{ac_w} + \frac{s_t}{\bar{s}} C_{L_{\alpha_t}} x_{ac_t} + \frac{s_b}{\bar{s}} C_{L_{\alpha_b}} x_{ac_b}}{\frac{s_w}{\bar{s}} C_{L_{\alpha_w}} + \frac{s_t}{\bar{s}} C_{L_{\alpha_t}} + \frac{s_b}{\bar{s}} C_{L_{\alpha_b}}} = 0.4374 \ ft \tag{3.2-12}$$

$$C_{L_{\alpha_{AFM}}} = \frac{s_w}{\bar{s}} C_{L_{\alpha_w}} + \frac{s_t}{\bar{s}} C_{L_{\alpha_t}} + \frac{s_b}{\bar{s}} C_{L_{\alpha_b}} = 0.0991 \ \frac{1}{deg} \tag{3.2-13}$$

$$C_{L_{\dot{\alpha}}} = 2C_{L_{\alpha_t}} \frac{x_{ac_t}}{\bar{c}} \frac{s_t}{\bar{s}} = 0.0674 \ \frac{1}{deg} \tag{3.2-14}$$

$$C_{L_q} = 2\frac{C_{L_\alpha}}{1+\frac{57.3\ C_{L_\alpha}}{\pi e_t AR_t}}\frac{x_{ac_t}}{\bar{c}}\frac{s_t}{\bar{s}} = 0.1136\ \frac{1}{deg} \tag{3.2-15}$$

$$C_{M_{\alpha_{AFM}}} = \frac{s_w}{\bar{s}}\frac{x_{cm}-x_{ac_w}}{\bar{c}}C_{M_{\alpha_w}} + \frac{s_t}{\bar{s}}\frac{x_{cm}-x_{ac_t}}{\bar{c}}C_{M_{\alpha_t}} + \frac{s_b}{\bar{s}}\frac{x_{cm}-x_{ac_b}}{\bar{c}}C_{M_{\alpha_b}} = -0.0251\ \frac{1}{deg} \tag{3.2-16}$$

$$C_{M_q} = -2\frac{C_{L_\alpha}}{1+\frac{57.3C_{L_\alpha}}{\pi e_t AR_t}}\frac{s_t}{\bar{s}}\left(\frac{x_{ac_t}}{\bar{c}}\right)^2 = -0.4052\ \frac{1}{deg} \tag{3.2-17}$$

$$C_{M_{\dot{\alpha}}} = \frac{C_{M_q}}{3} = -0.1351\ \frac{1}{deg} \tag{3.2-18}$$

Table 3.4 Dimensional Stability Derivatives

$Z_\alpha = \frac{-\bar{q}\bar{s}C_{L_{\alpha_{AFM}}}}{m}\frac{180}{\pi} = -329.0019\ \frac{ft/s^2}{rad}$	$Z_{\alpha_w} = \frac{-\bar{q}s_w C_{L_{\alpha_w}}}{m}\frac{180}{\pi} = -284.5202\frac{ft/s^2}{rad}$
$Z_{\alpha_b} = \frac{-\bar{q}s_b C_{L_{\alpha_b}}}{m}\frac{180}{\pi} = -11.4719\ \frac{ft/s^2}{rad}$	$Z_{\alpha_t} = \frac{-\bar{q}s_w C_{L_{\alpha_t}}}{m}\frac{180}{\pi} = -33.0098\ \frac{ft/s^2}{rad}$
$Z_{\dot{\alpha}} = \frac{-\bar{q}\bar{s}\bar{c}C_{L_{\dot{\alpha}}}}{2mV_{cm}}\frac{180}{\pi} = -1.5886\ \frac{ft/s^2}{rad/s}$	$Z_q = \frac{-\bar{q}\bar{s}C_{L_q}}{2mV_{cm}}\frac{180}{\pi} = -2.6767\ \frac{ft/s^2}{rad/s}$
$Z_{\delta_e} = \frac{-\bar{q}\bar{s}C_{L_{\delta_e}}}{m}\frac{180}{\pi} = -35.5956\ \frac{ft/s^2}{rad}$	$Z_{\delta_f} = \frac{-\bar{q}\bar{s}C_{L_{\delta_f}}}{m}\frac{180}{\pi} = -71.1301\ \frac{ft/s^2}{rad}$
$M_\alpha = \frac{\bar{q}\bar{s}\bar{c}C_{M_{\alpha_{AFM}}}}{I_{yy}}\frac{180}{\pi} = -48.8791\ \frac{rad/s^2}{rad}$	$M_{\alpha_w} = \frac{\bar{q}\bar{s}\bar{c}C_{M_{\alpha_w}}}{I_{yy}}\frac{180}{\pi} = 10.8627\ \frac{rad/s^2}{rad}$
$M_{\alpha_b} = \frac{\bar{q}\bar{s}\bar{c}C_{M_{\alpha_b}}}{I_{yy}}\frac{180}{\pi} = 3.2607\ \frac{rad/s^2}{rad}$	$M_{\alpha_t} = \frac{\bar{q}\bar{s}\bar{c}C_{M_{\alpha_t}}}{I_{yy}}\frac{180}{\pi} = -63.0024\ \frac{rad/s^2}{rad}$
$M_{\dot{\alpha}} = \frac{\bar{q}\bar{s}\bar{c}^2C_{M_{\dot{\alpha}}}}{2I_{yy}V_{cm}}\frac{180}{\pi} = -1.8679\ \frac{rad/s^2}{rad/s}$	$M_q = \frac{\bar{q}\bar{s}\bar{c}^2C_{M_q}}{2I_{yy}V_{cm}}\frac{180}{\pi} = -5.6037\ \frac{rad/s^2}{rad/s}$
$M_{\delta_e} = \frac{\bar{q}\bar{s}\bar{c}C_{M_{\delta_e}}}{I_{yy}}\frac{180}{\pi} = -71.4732\frac{rad/s^2}{rad}$	$M_{\delta_f} = \frac{\bar{q}\bar{s}\bar{c}C_{M_{\delta_f}}}{I_{yy}}\frac{180}{\pi} = -7.7261\frac{rad/s^2}{rad}$

3.3 Separate Gust Verification

In order to verify that the separate gust method of approach was mathematically correct, time histories of a step response of 1.95 degrees, or 2 ft/s, of the single or point gust model were plotted with a step response for the separate or distributed gust model, with the gust hitting the wing, body, and tail at the same time step. Figures 3.1 and 3.3 show the individual pitch rate and the normal acceleration response contributions from each airframe component due to the input for the distributed gust model. Note these individual responses are not the actual motions of the components since the aircraft is rigid and does not permit relative motion between its parts. Here, an individual response represents the motion of a complete but imaginary aircraft where all but one of the component aerodynamics have been deactivated. It is noted that the wing and body respond to the gust input for different directions than the tail. This behavior was expected, due to the signs of the dimensional stability derivatives in Table 3.4. Figures 3.2 and 3.4 show that the summed results match the complete gust response curves exactly. These results show that a sense or verification that the distributed gust model was divided up correctly from the single or point gust model.

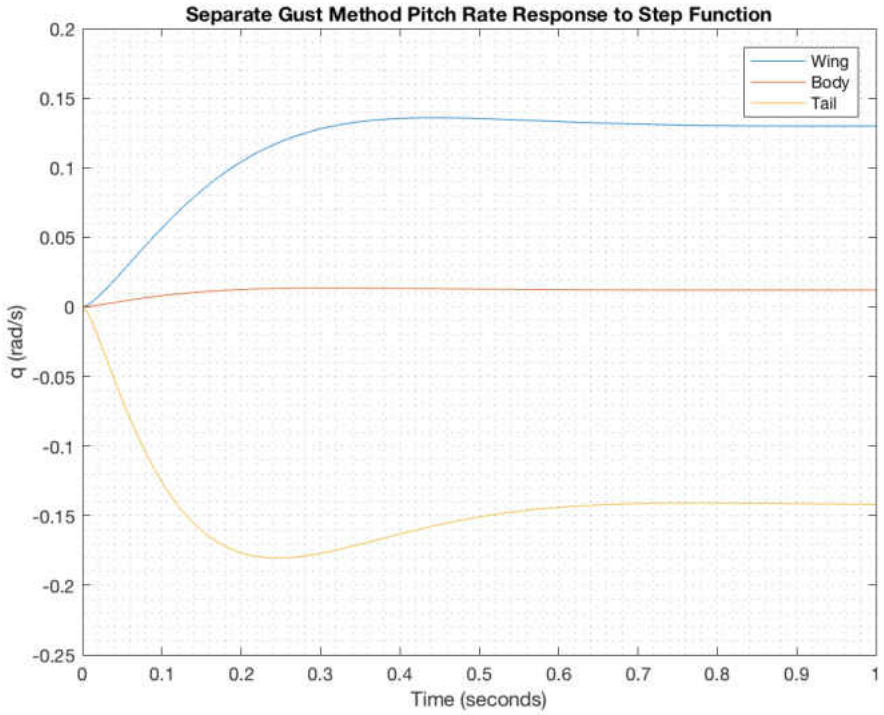

Figure 3.1 Separate Gust Pitch Rate Response

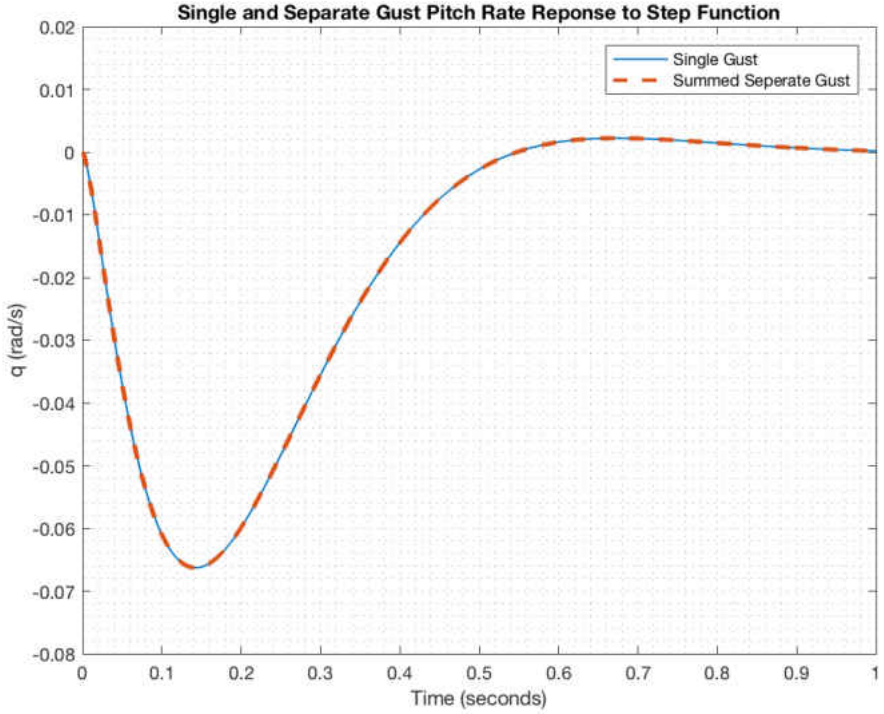

Figure 3.2 Single vs. Separate Gust Pitch Rate Comparison

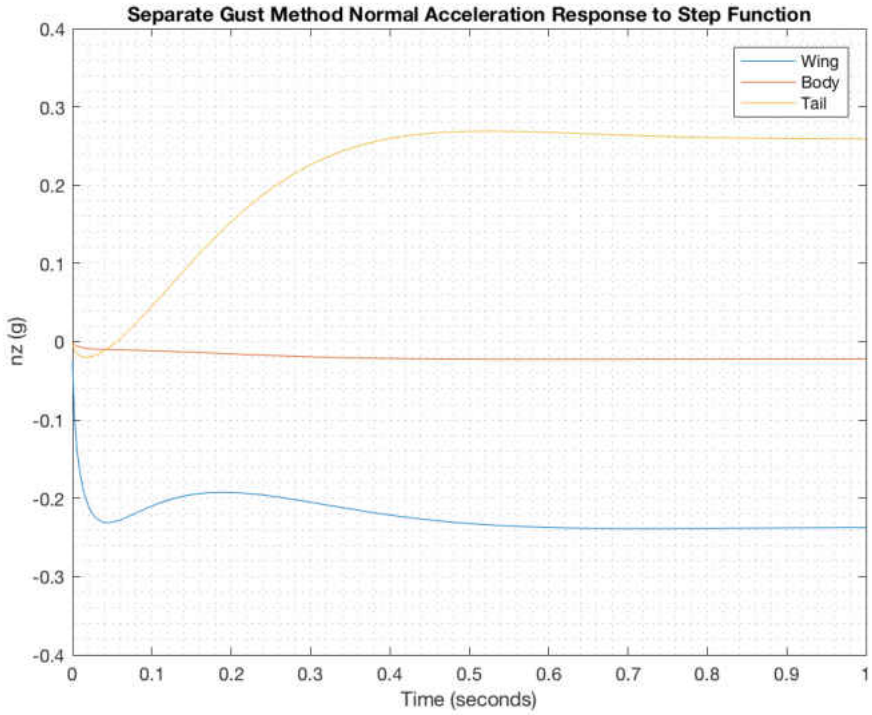

Figure 3.3 Separate Gust Normal Acceleration Response

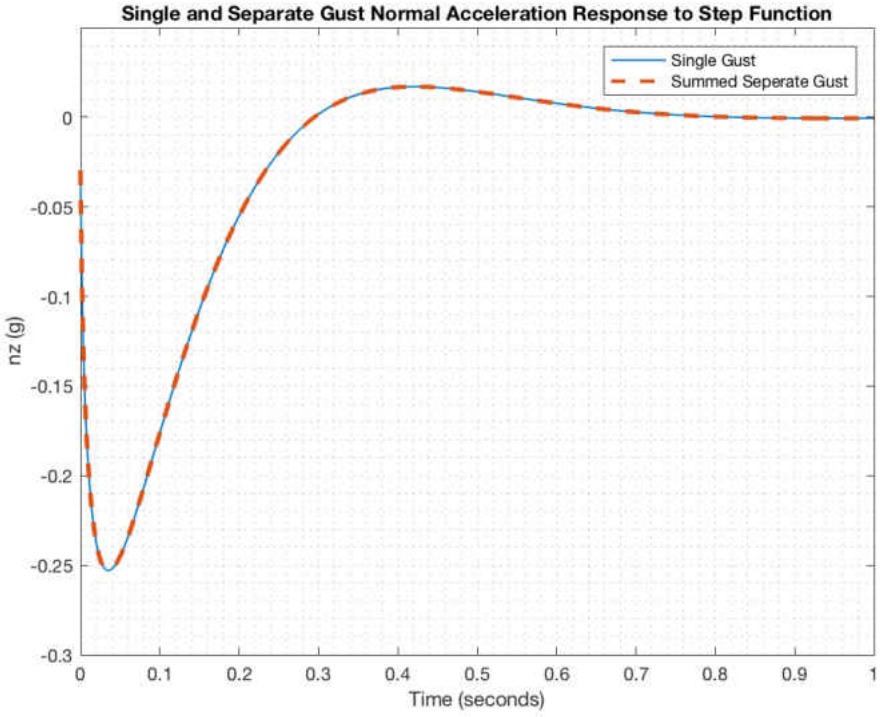

Figure 3.4 Single vs. Separate Gust Normal Acceleration Comparison

3.4 Unsteady Aerodynamics

In order to make the two degree of freedom aerodynamic model of the AFM as realistic and accurate as possible, indicial concepts were included into the state space system. In flight, a step input of a control surface will not immediately generate the entirety of its lift. In fact, the lift will build-up over a short period of time. Operational equivalents of angle of attack and gust induced lift build-up on a wing, using an aspect ratio of 6, were found in NACA-TR-681 by R. T. Jones [35]. These indicial models are given in equations (3.4-1) and (3.4-2). An expression for control surface lift in Equation (3.4-3), based on Equation (3.4-1), was used, from previous research supported by ViGYAN using computational fluid dynamics. These equations were described originally in terms of non-dimensional half chord lengths, "s". To reshape the equations in terms of time, the equations were normalized, and the variable "s" was replaced by the variable "t", expressed in seconds, divided by the time calculated to approximately travel one-half chord length at 40 mph, to arrive at Equations (3.4-4) – (3.4-6). A graphical representation is shown in Figure 3.5. Note that L_{α}, L_{g}, and L_{cs} are non-dimensional. Also note that the angle of attack and control surface lift responses have an initial direct feedthrough or impulsive nature, while the gust lift response does not. All indicial responses are rapid, compared to typical airframe frequencies.

$$L_\alpha(s) = 1.48\pi(1.000 - 0.361e^{-0.381\,s}) \tag{3.4-1}$$

$$L_g(s) = 1.50\pi(1.000 - 0.448e^{-0.290\,s} - 0.272e^{-0.725\,s} - 0.193e^{-3.00\,s}) \tag{3.4-2}$$

$$L_{CS}(s) = 1.000 - 0.44e^{-0.2334\,s} \tag{3.4-3}$$

$$L_\alpha(t) = 1.000 - 0.361e^{-53.662\,t} \tag{3.4-4}$$

$$L_g(t) = 1.000 - 0.448e^{-40.845\,t} - 0.272e^{-102.113\,t} - 0.193e^{-422.535\,t} \tag{3.4-5}$$

$$L_{CS}(t) = 1.000 - 0.44e^{-32.872\,t} \tag{3.4-6}$$

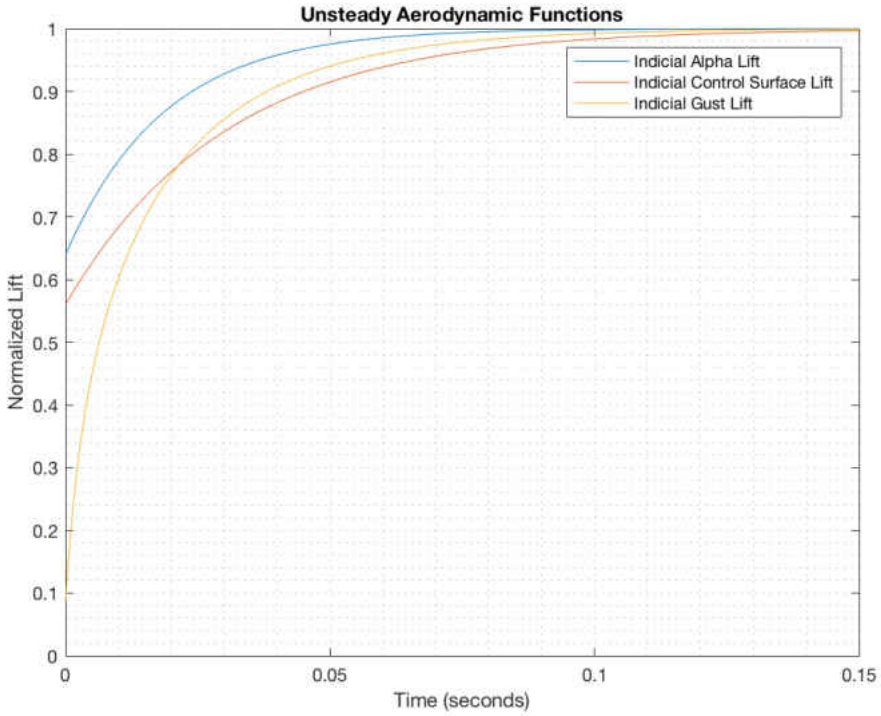

Figure 3.5 Unsteady Aerodynamic Functions

To append the indicial equations to the inputs of the aerodynamic state space model, first the Laplace transform of Equations (3.4-5) and (3.4-6) were taken, to

express Equations (3.4-7) and (3.4-8) in the form of numerical transfer functions, where "s" is the independent Laplace variable. Note the expression for L_α is not shown, as it is not included in the analysis.

$$L_{CS}(s) = \frac{0.56s + 32.872}{s + 32.872} * \frac{1}{s} \tag{3.4-7}$$

$$L_g(s) = \frac{0.087\, s^3 + 176.82\, s^2 + 39746.8\, s + 1.76231 * 10^6}{s^3 + 565.493\, s^2 + 64575.6\, s + 1.76231 * 10^6} * \frac{1}{s} \tag{3.4-8}$$

Since these functions describe lift with respect to a unit step input, the 1/s step term could be removed from each equation, yielding transfer functions for any input type. These transfer functions were then put into state space representation, in order for them to be appended to the model. This process would yield five state space systems as indicated below: two for the control surfaces, and three for each component of the aircraft. In these models, x_f, x_e, x_w, x_b, x_t represent aerodynamic indicial state variables, and $y_f = L_f = L_{cs},\ y_e = L_e = L_{cs},\ y_w = L_w = L_g, y_b = L_b = L_g,\ y_t = L_t = L_g$ denote the aerodynamic output lifts. Table 3.5 lists the numeric values associated with these models.

$$\dot{x}_f = \left[A_{11_f}\right]\left[x_f\right] + \left[\delta_f\right] \tag{3.4-9}$$

$$y_f = \left[C_{11_f}\right]\left[x_f\right] + \left[D_{11_f}\right]\left[\delta_f\right] \tag{3.4-10}$$

$$\dot{x}_e = \left[A_{11_e}\right]\left[x_e\right] + \left[\delta_e\right] \tag{3.4-11}$$

$$y_e = \left[C_{11_e}\right]\left[x_e\right] + \left[D_{11_e}\right]\left[\delta_e\right] \tag{3.4-12}$$

$$\dot{x}_w = \begin{bmatrix} 0 & 1 & 0 \\ 0 & 0 & 1 \\ A_{31_w} & A_{32_w} & A_{33_w} \end{bmatrix} [x_w] + \begin{bmatrix} 0 \\ 0 \\ 1 \end{bmatrix} [\alpha_{g_w}] \tag{3.4-13}$$

$$y_w = [C_{11_w} \quad C_{12_w} \quad C_{13_w}][x_w] + [D_{11_w}][\alpha_{g_w}] \tag{3.4-14}$$

$$\dot{x}_b = \begin{bmatrix} 0 & 1 & 0 \\ 0 & 0 & 1 \\ A_{31_b} & A_{32_b} & A_{33_b} \end{bmatrix} [x_b] + \begin{bmatrix} 0 \\ 0 \\ 1 \end{bmatrix} [\alpha_{g_b}] \tag{3.4-15}$$

$$y_b = [C_{11_b} \quad C_{12_b} \quad C_{13_b}][x_b] + [D_{11_b}][\alpha_{g_b}] \tag{3.4-16}$$

$$\dot{x}_t = \begin{bmatrix} 0 & 1 & 0 \\ 0 & 0 & 1 \\ A_{31_t} & A_{32_t} & A_{33_t} \end{bmatrix} [x_t] + \begin{bmatrix} 0 \\ 0 \\ 1 \end{bmatrix} [\alpha_{g_t}] \tag{3.4-17}$$

$$y_t = [C_{11_t} \quad C_{12_t} \quad C_{13_t}][x_t] + [D_{11_t}][\alpha_{g_t}] \tag{3.4-18}$$

Table 3.5 Indicial State Space Constants

$A_{11_f} = A_{11_e} = -32.87$	$C_{11_f} = C_{11_e} = 14.46$
$D_{11_f} = D_{11_e} = 0.56$	$A_{31_w} = A_{31_b} = A_{31_t} = -565.5$
$A_{32_w} = A_{32_b} = A_{32_t} = -6.458e+04$	$A_{33_w} = A_{33_b} = A_{33_t} = -1.762e+06$
$C_{11_w} = C_{11_b} = C_{11_t} = 127.6$	$C_{12_w} = C_{12_b} = C_{12_t} = -6.458e+04$
$C_{13_w} = C_{13_b} = C_{13_t} = 1.609e+06$	$D_{11_w} = D_{11_b} = D_{11_t} = 0.087$

To append the indicial systems to the aircraft state space system, the indicial systems would be linked to the inputs of the model, control surface deflections, and gust angle of attack on the wing, tail and body. The total system state space matrix form is shown in Equations (3.4-19) - (3.4-20).

$$\begin{bmatrix} \dot{\alpha} \\ \dot{q} \\ \dot{x}_e \\ \dot{x}_f \\ \dot{x}_{w_1} \\ \dot{x}_{w_2} \\ \dot{x}_{w_3} \\ \dot{x}_{b_1} \\ \dot{x}_{b_2} \\ \dot{x}_{b_3} \\ \dot{x}_{t_1} \\ \dot{x}_{t_2} \\ \dot{x}_{t_3} \end{bmatrix} = \begin{bmatrix} A_{11} & A_{12} & B_{11}C_{11_e} & B_{12}C_{11_f} & B_{13}C_{11_w} & B_{13}C_{12_w} & B_{13}C_{13_w} & B_{14}C_{11_b} & B_{14}C_{12_b} & B_{14}C_{13_b} & B_{15}C_{11_t} & B_{15}C_{12_t} & B_{15}C_{13_t} \\ A_{21} & A_{22} & B_{21}C_{11_e} & B_{22}C_{11_f} & B_{23}C_{11_w} & B_{23}C_{12_w} & B_{23}C_{13_w} & B_{24}C_{11_b} & B_{24}C_{12_b} & B_{24}C_{13_b} & B_{25}C_{11_t} & B_{25}C_{12_t} & B_{25}C_{13_t} \\ 0 & 0 & A_{11_e} & 0 & 0 & 0 & 0 & 0 & 0 & 0 & 0 & 0 & 0 \\ 0 & 0 & 0 & A_{11_f} & 0 & 0 & 0 & 0 & 0 & 0 & 0 & 0 & 0 \\ 0 & 0 & 0 & 0 & 0 & 1 & 0 & 0 & 0 & 0 & 0 & 0 & 0 \\ 0 & 0 & 0 & 0 & 0 & 0 & 1 & 0 & 0 & 0 & 0 & 0 & 0 \\ 0 & 0 & 0 & 0 & A_{13_w} & A_{23_w} & A_{33_w} & 0 & 0 & 0 & 0 & 0 & 0 \\ 0 & 0 & 0 & 0 & 0 & 0 & 0 & 0 & 1 & 0 & 0 & 0 & 0 \\ 0 & 0 & 0 & 0 & 0 & 0 & 0 & 0 & 0 & 1 & 0 & 0 & 0 \\ 0 & 0 & 0 & 0 & 0 & 0 & 0 & A_{13_b} & A_{23_b} & A_{33_b} & 0 & 0 & 0 \\ 0 & 0 & 0 & 0 & 0 & 0 & 0 & 0 & 0 & 0 & 0 & 1 & 0 \\ 0 & 0 & 0 & 0 & 0 & 0 & 0 & 0 & 0 & 0 & 0 & 0 & 1 \\ 0 & 0 & 0 & 0 & 0 & 0 & 0 & 0 & 0 & 0 & A_{13_t} & A_{23_t} & A_{33_t} \end{bmatrix} \begin{bmatrix} \alpha \\ q \\ x_e \\ x_f \\ x_{w_1} \\ x_{w_2} \\ x_{w_3} \\ x_{b_1} \\ x_{b_2} \\ x_{b_3} \\ x_{t_1} \\ x_{t_2} \\ x_{t_3} \end{bmatrix}$$

$$+ \begin{bmatrix} B_{11}D_{11_e} & B_{12}D_{11_f} & B_{13}D_{11_w} & B_{14}D_{11_b} & B_{15}D_{11_t} \\ B_{21}D_{11_e} & B_{22}D_{11_f} & B_{23}D_{11_w} & B_{24}D_{11_b} & B_{25}D_{11_t} \\ 1 & 0 & 0 & 0 & 0 \\ 0 & 1 & 0 & 0 & 0 \\ 0 & 0 & 0 & 0 & 0 \\ 0 & 0 & 0 & 0 & 0 \\ 0 & 0 & 1 & 0 & 0 \\ 0 & 0 & 0 & 0 & 0 \\ 0 & 0 & 0 & 0 & 0 \\ 0 & 0 & 0 & 1 & 0 \\ 0 & 0 & 0 & 0 & 0 \\ 0 & 0 & 0 & 0 & 0 \\ 0 & 0 & 0 & 0 & 1 \end{bmatrix} \begin{bmatrix} \delta_e \\ \delta_f \\ \alpha_{g_w} \\ \alpha_{g_t} \\ \alpha_{g_b} \end{bmatrix} \tag{3.4.19}$$

$$\begin{bmatrix} \alpha \\ q \\ n_z \end{bmatrix} = \begin{bmatrix} 1 & 0 & 0 & 0 & 0 & 0 & 0 & 0 & 0 & 0 & 0 & 0 & 0 \\ 0 & 1 & 0 & 0 & 0 & 0 & 0 & 0 & 0 & 0 & 0 & 0 & 0 \\ \frac{V_{cm}}{g}A_{11} & \frac{V_{cm}}{g}(A_{12}-1) & \frac{V_{cm}}{g}B_{11}C_{11_e} & \frac{V_{cm}}{g}B_{12}C_{11_f} & \frac{V_{cm}}{g}B_{13}C_{11_w} & \frac{V_{cm}}{g}B_{13}C_{12_w} & \frac{V_{cm}}{g}B_{13}C_{13_w} & \frac{V_{cm}}{g}B_{14}C_{11_b} & \frac{V_{cm}}{g}B_{14}C_{12_b} & \frac{V_{cm}}{g}B_{14}C_{13_b} & \frac{V_{cm}}{g}B_{15}C_{11_t} & \frac{V_{cm}}{g}B_{15}C_{12_t} & \frac{V_{cm}}{g}B_{15}C_{13_t} \end{bmatrix} \begin{bmatrix} \alpha \\ q \\ x_e \\ x_f \\ x_{w_1} \\ x_{w_2} \\ x_{w_3} \\ x_{b_1} \\ x_{b_2} \\ x_{b_3} \\ x_{t_1} \\ x_{t_2} \\ x_{t_3} \end{bmatrix}$$

$$+ \begin{bmatrix} 0 & 0 & 0 & 0 & 0 \\ 0 & 0 & 0 & 0 & 0 \\ B_{11}\frac{V_{cm}}{g}D_{11_e} & B_{12}\frac{V_{cm}}{g}D_{11_f} & B_{13}\frac{V_{cm}}{g}D_{11_w} & B_{14}\frac{V_{cm}}{g}D_{11_b} & B_{15}\frac{V_{cm}}{g}D_{11_t} \end{bmatrix} \begin{bmatrix} \delta_e \\ \delta_f \\ \alpha_{g_w} \\ \alpha_{g_b} \\ \alpha_{g_t} \end{bmatrix} \tag{3.4.20}$$

3.5 Transfer Functions

Graphical transfer functions (i.e., frequency responses) were generated to compare the unsteady indicial and steady non-indicial models. The characteristics are shown in Figures 3.6 - 3.23. Note that, in Figures 3.18 - 3.23, the gust attack angle represents a combined wing, body, and tail gust angle of attack. As expected, the two mathematical models show no differences at the low frequencies. However, at the high frequencies, the magnitudes begin to decrease more quickly with respect to frequency for the indicial models. This higher attenuation rate occurs due to the fact that at high frequencies, the exponential functions do not have sufficient time to build up their respective values before the input is changed again. These extra aerodynamic lags are also clearly evident in the higher attenuation rates of the phase responses. Note the peaks and change of slopes in the magnitude plots around 1 hertz. This feature corresponds with the AFM airframe's natural short period frequency. The phase plots also show the effect of unsteady aerodynamics at the higher frequencies by trending more out of phase from the designated input. The steady and unsteady aerodynamic numerical transfer functions are given in Tables 3.6 through 3.17, where the component gusts are kept separate.

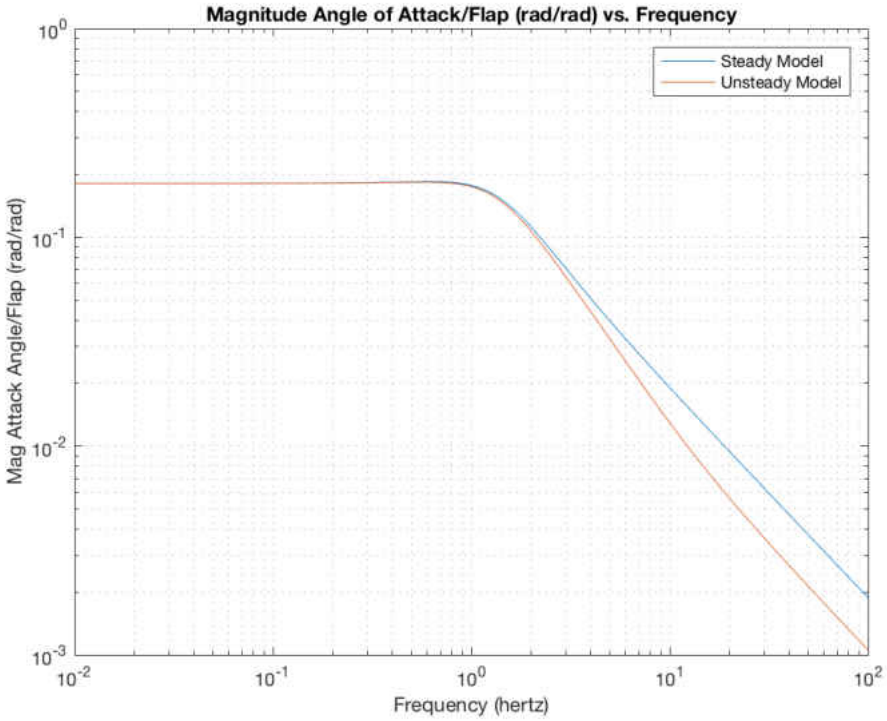

Figure 3.6 Angle of Attack per Flap Magnitude

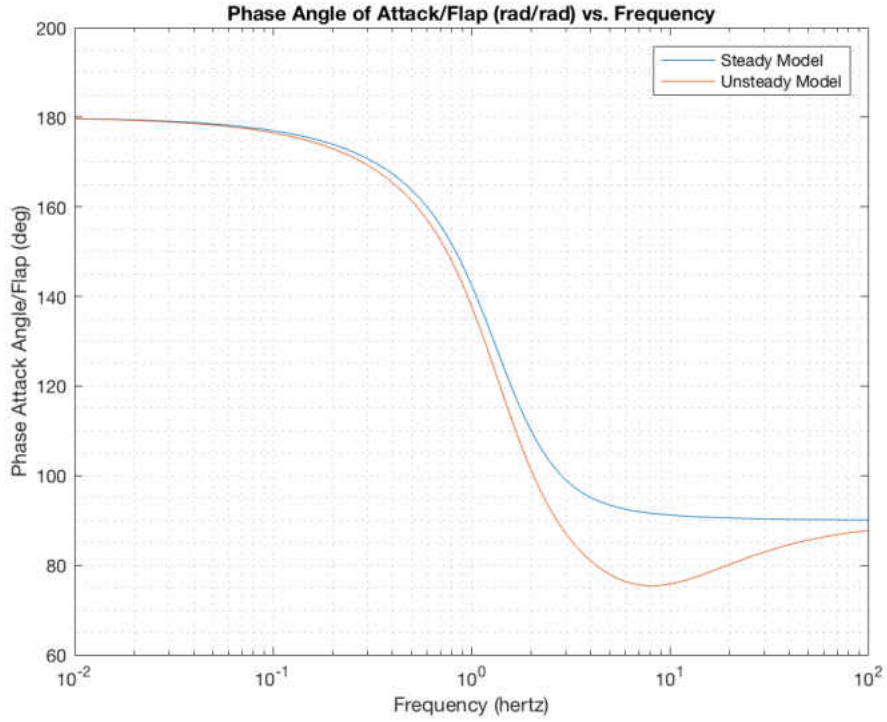

Figure 3.7 Angle of Attack per Flap Phase

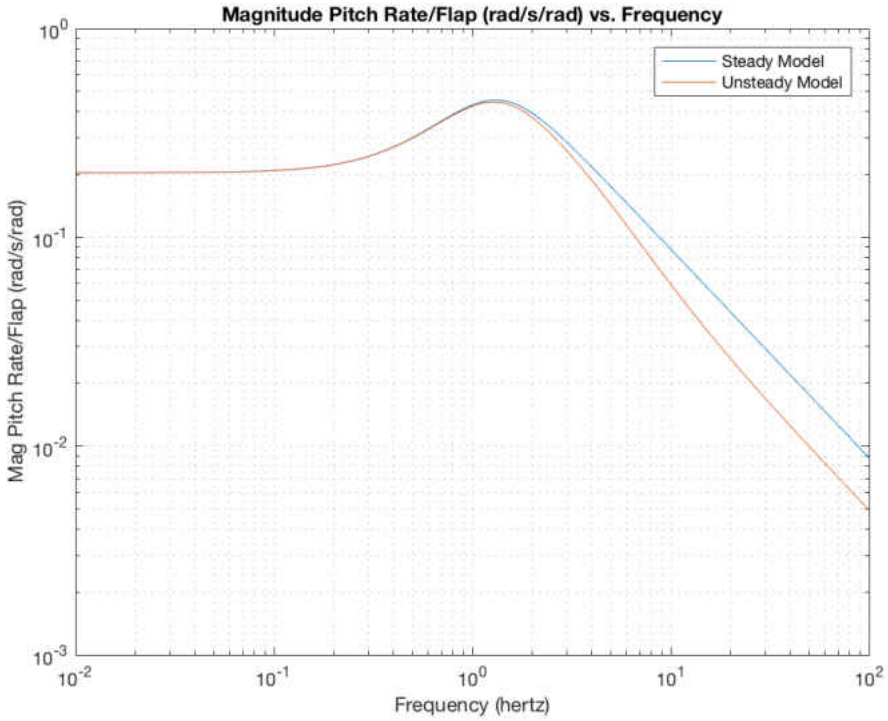

Figure 3.8 Pitch Rate per Flap Magnitude

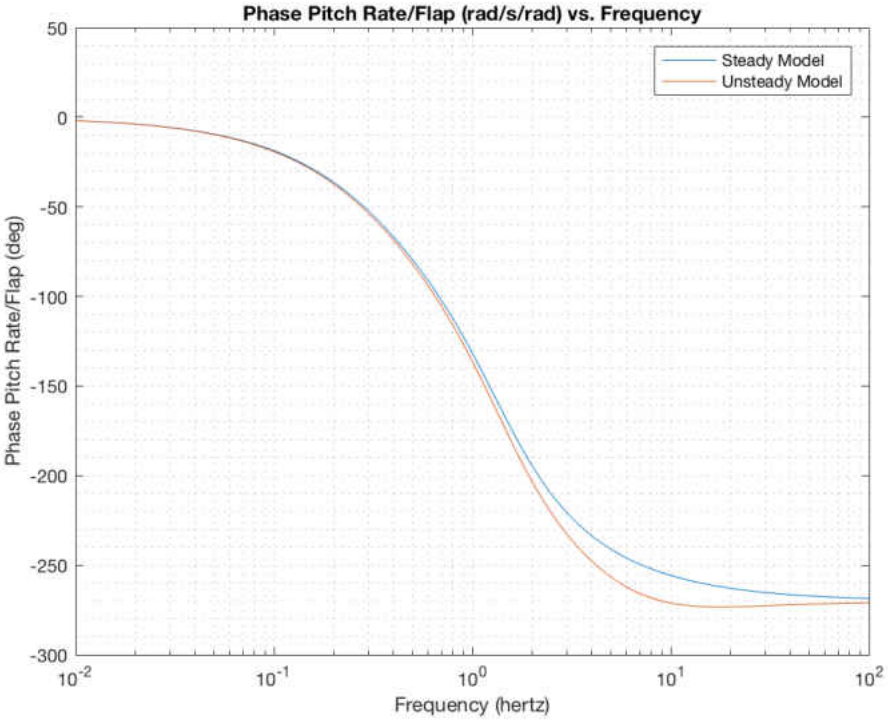

Figure 3.9 Pitch Rate per Flap Phase

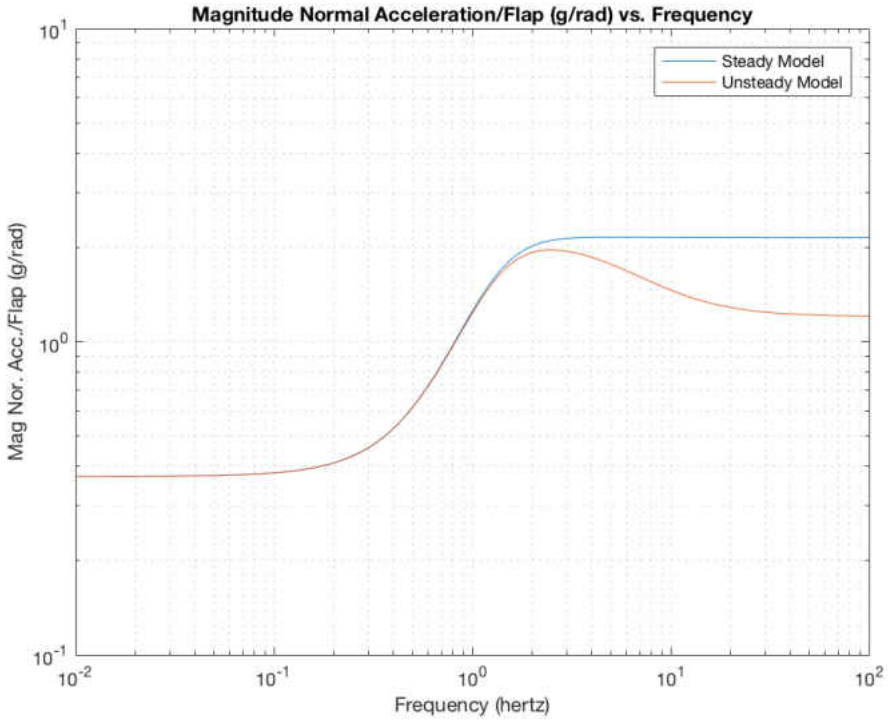

Figure 3.10 Normal Acceleration per Flap Magnitude

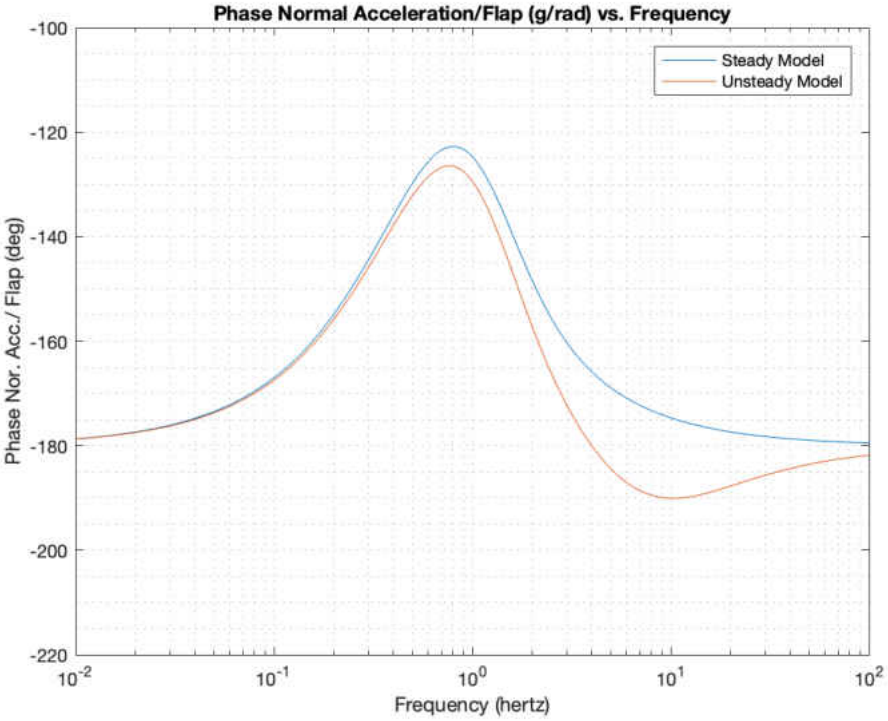

Figure 3.11 Normal Acceleration per Flap Phase

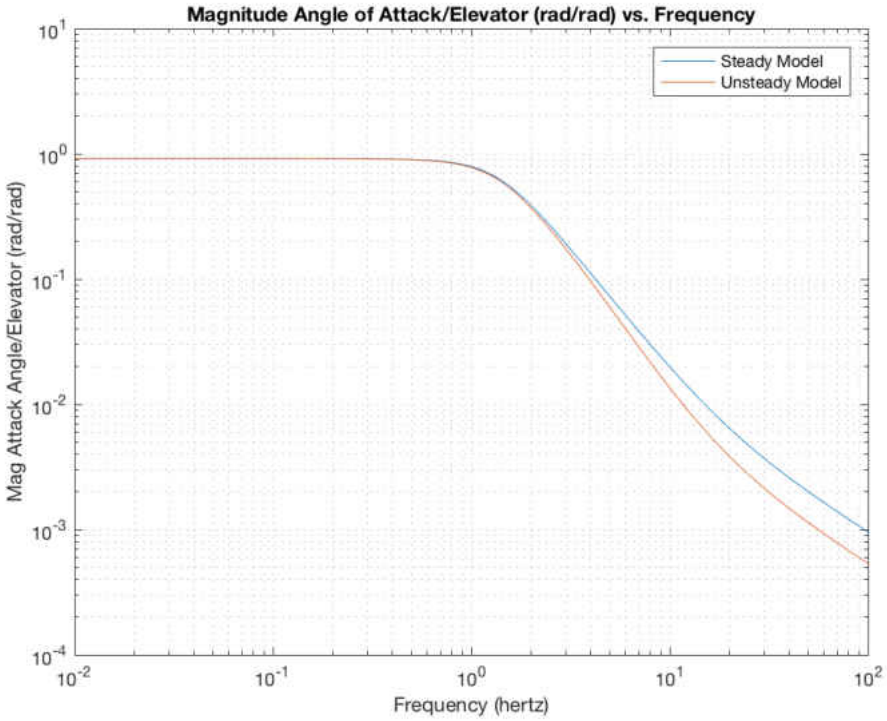

Figure 3.12 Angle of Attack per Elevator Magnitude

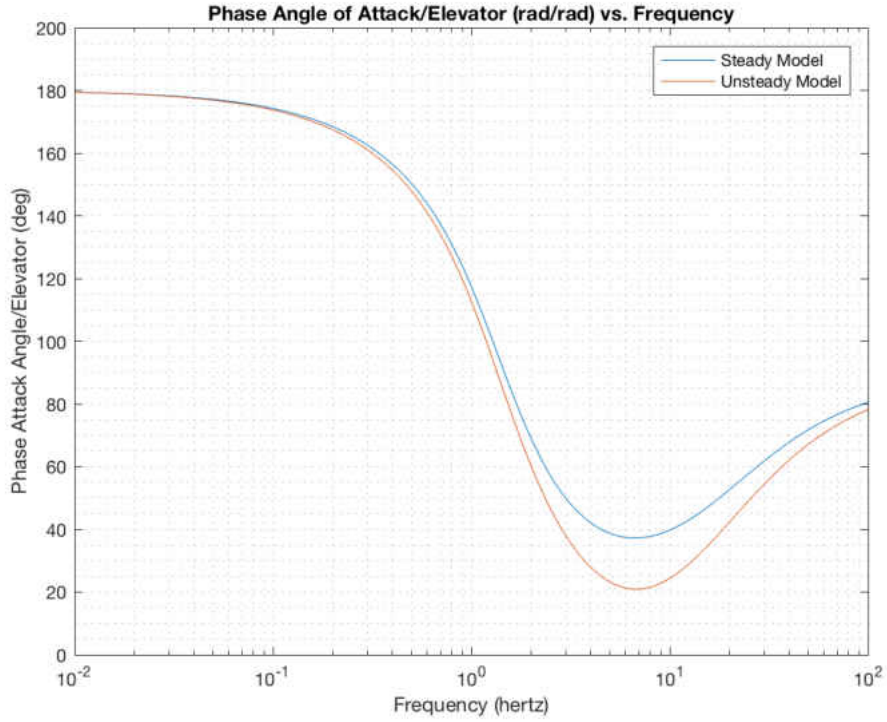

Figure 3.13 Angle of Attack per Elevator Phase

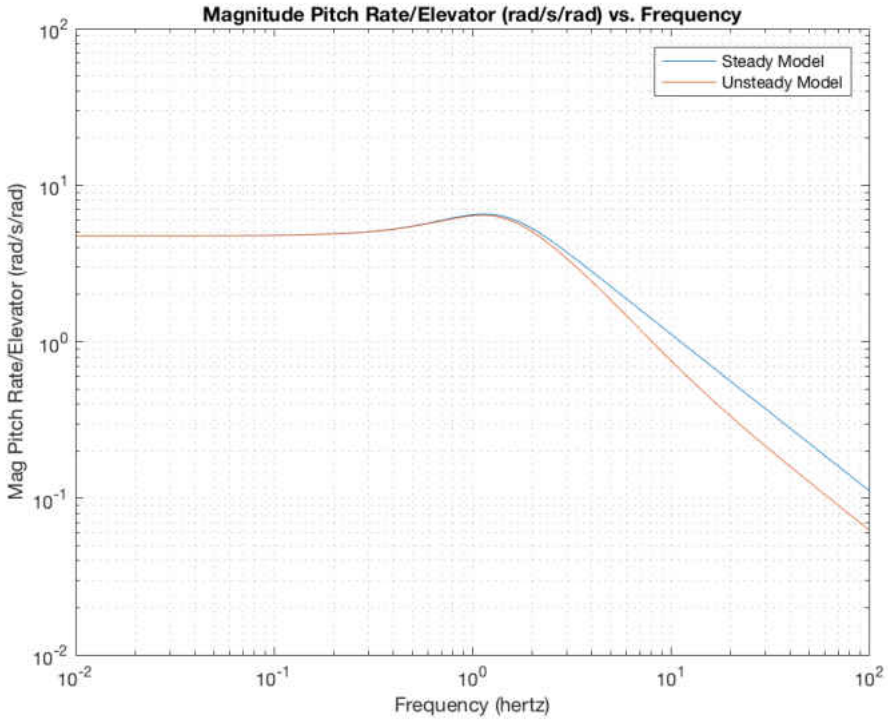

Figure 3.14 Pitch Rate per Elevator Magnitude

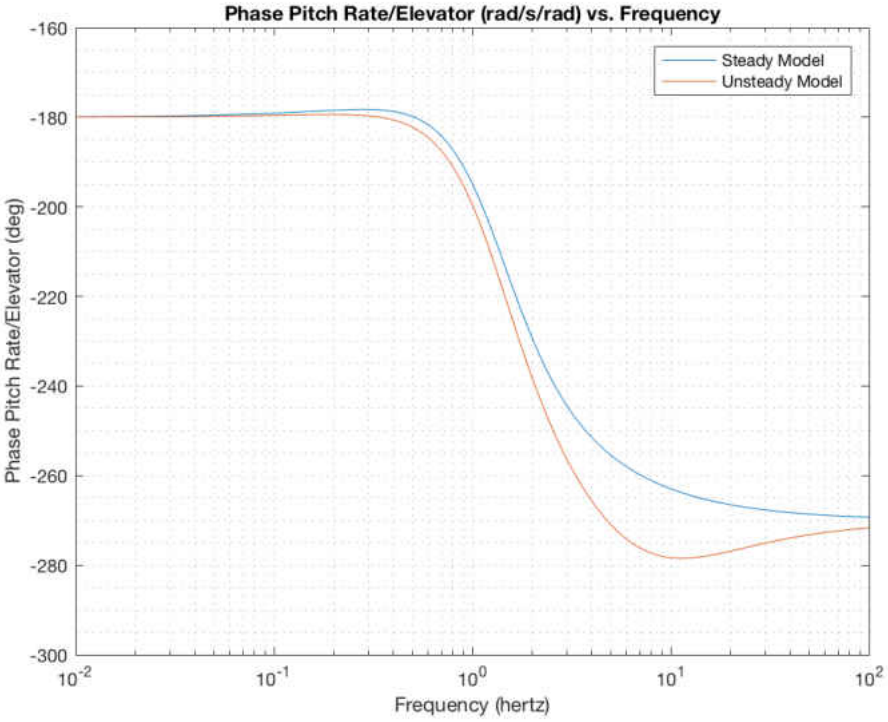

Figure 3.15 Pitch Rate per Elevator Phase

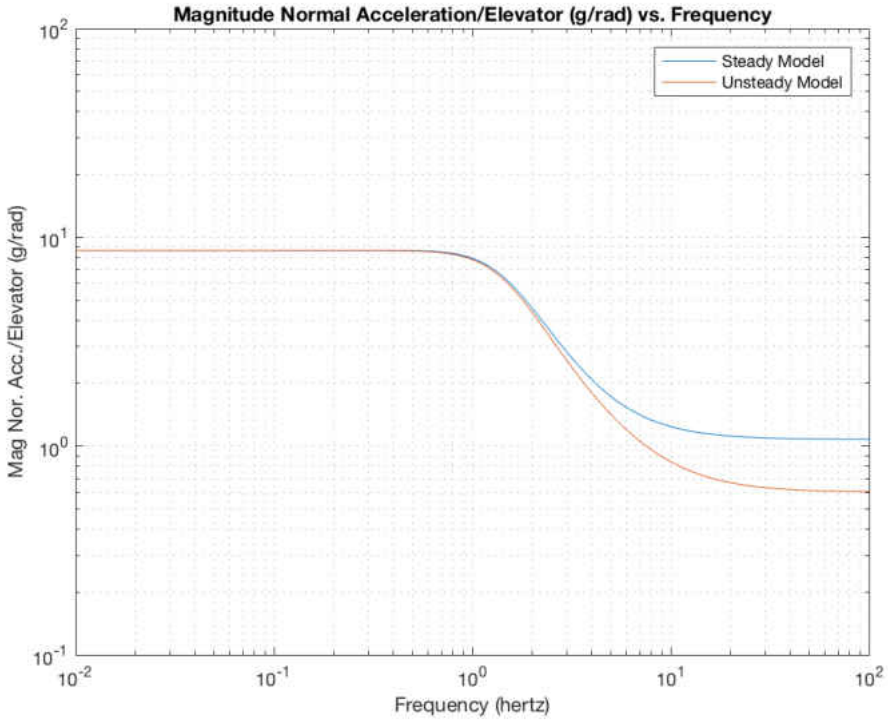

Figure 3.16 Normal Acceleration per Elevator Magnitude

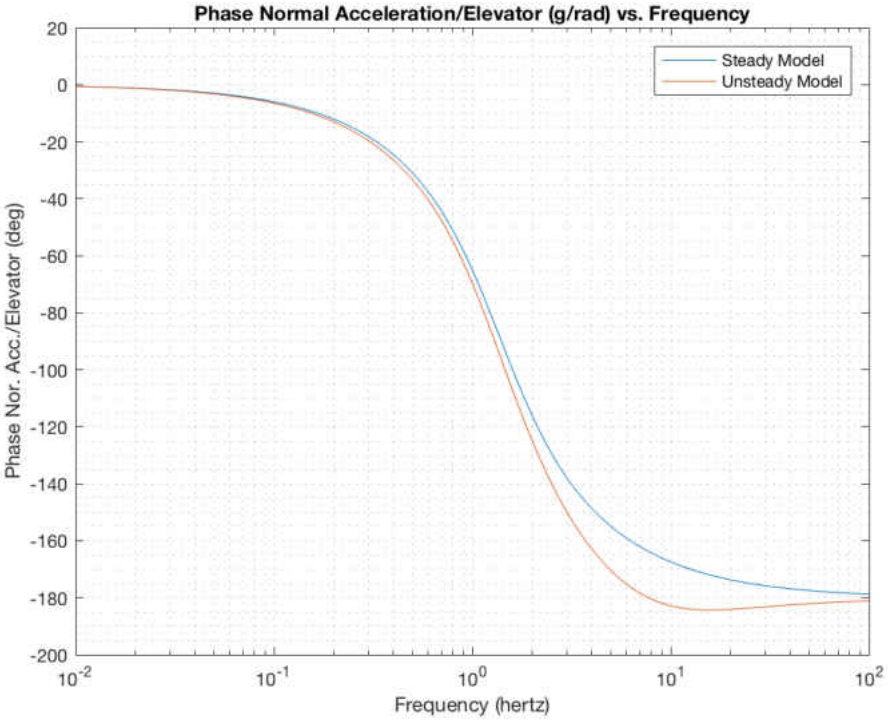

Figure 3.17 Normal Acceleration per Elevator Phase

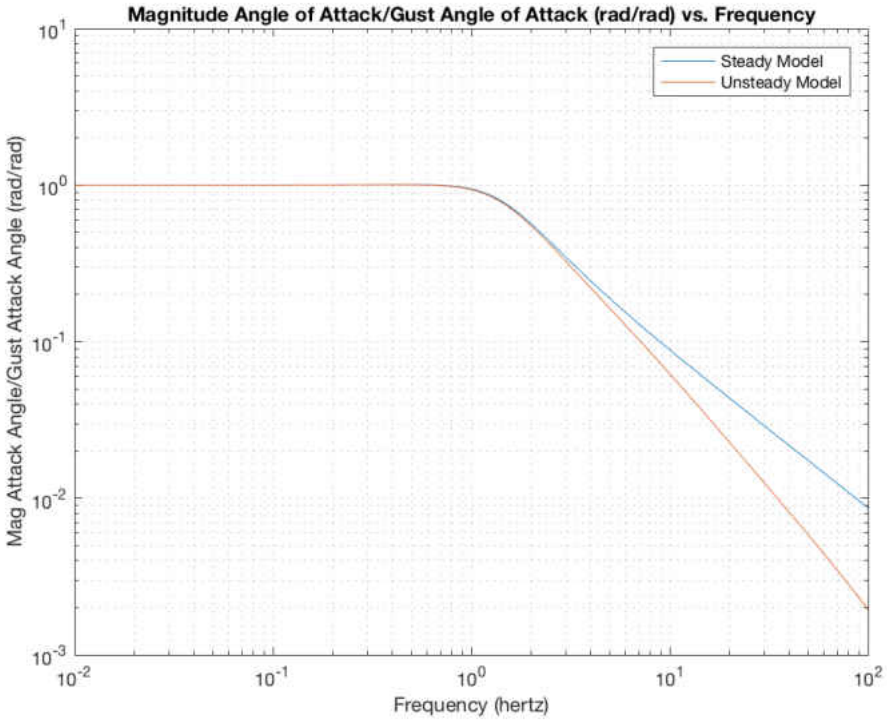

Figure 3.18 Angle of Attack per Gust Angle of Attack Magnitude

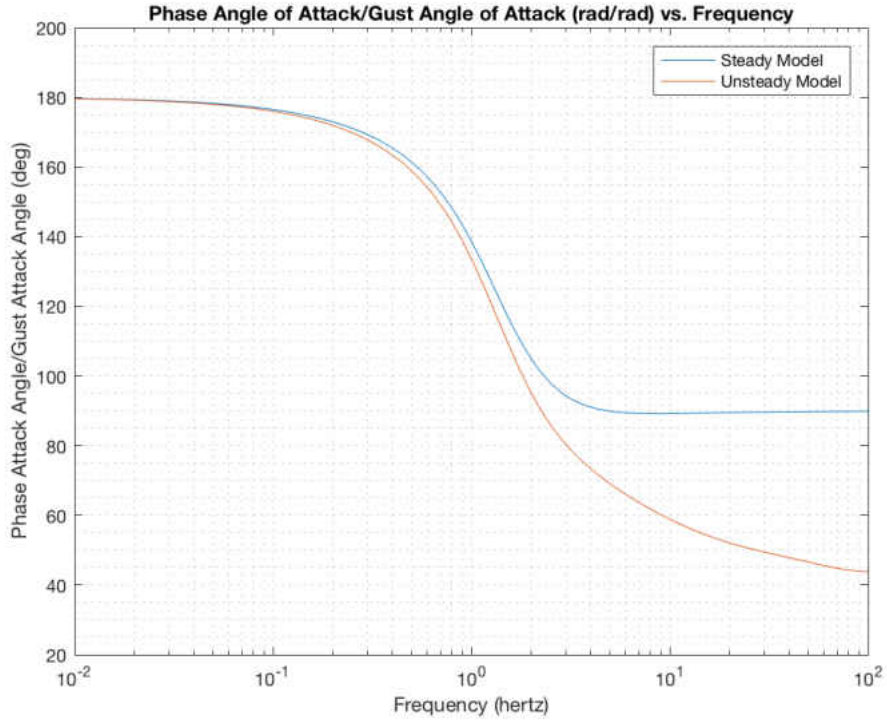

Figure 3.19 Angle of Attack per Gust Angle of Attack Phase

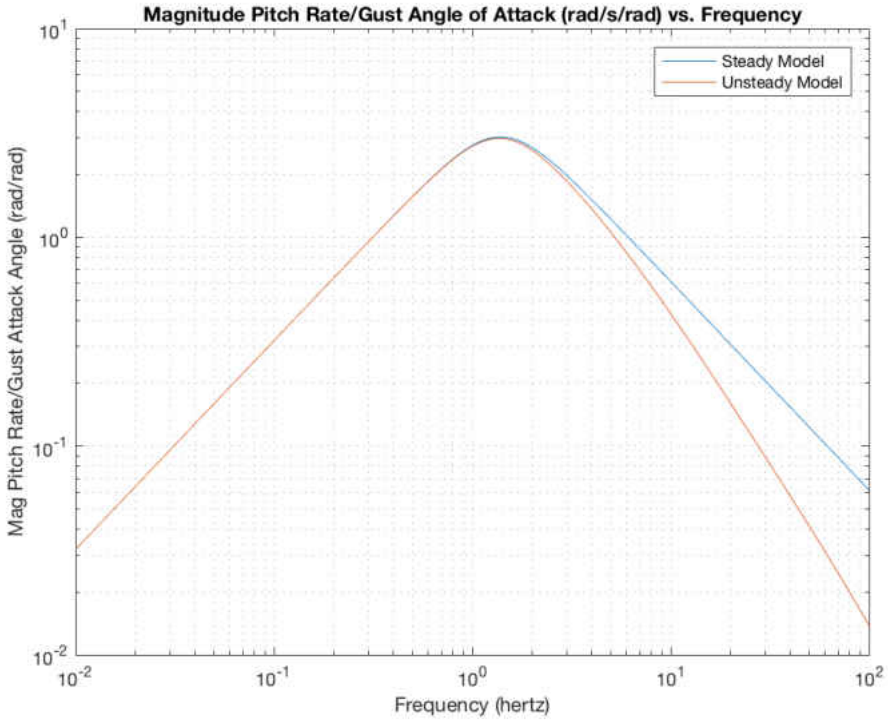

Figure 3.20 Pitch Rate per Gust Angle of Attack Magnitude

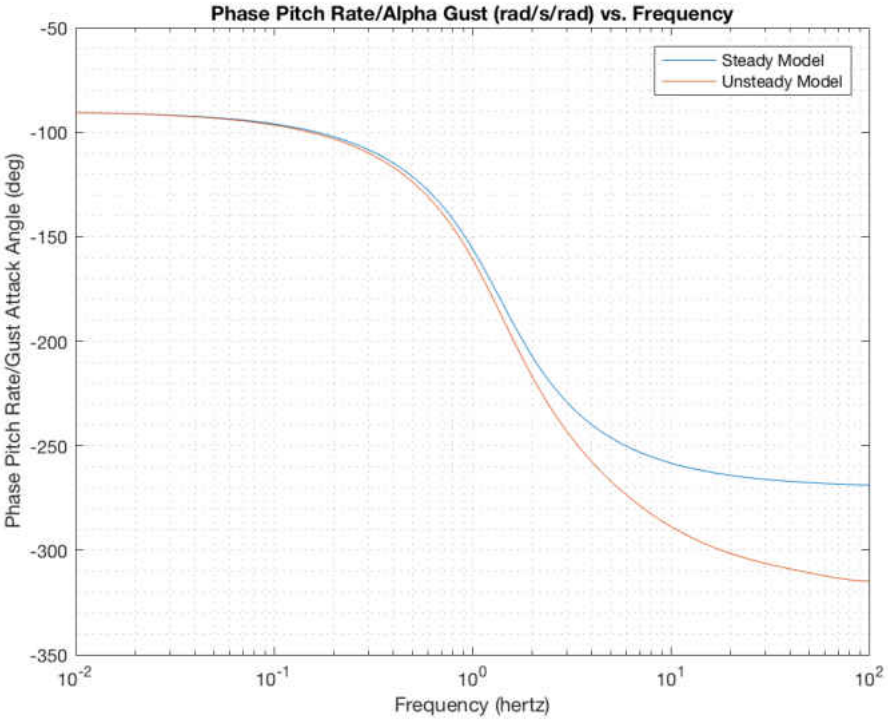

Figure 3.21 Pitch Rate per Gust Angle of Attack Phase

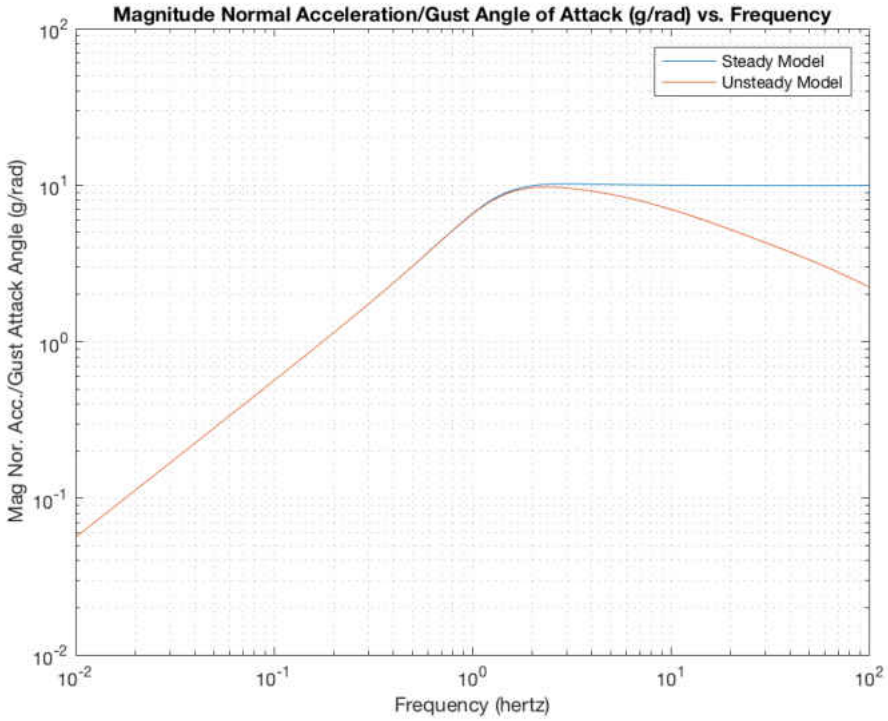

Figure 3.22 Normal Acceleration per Gust Angle of Attack Magnitude

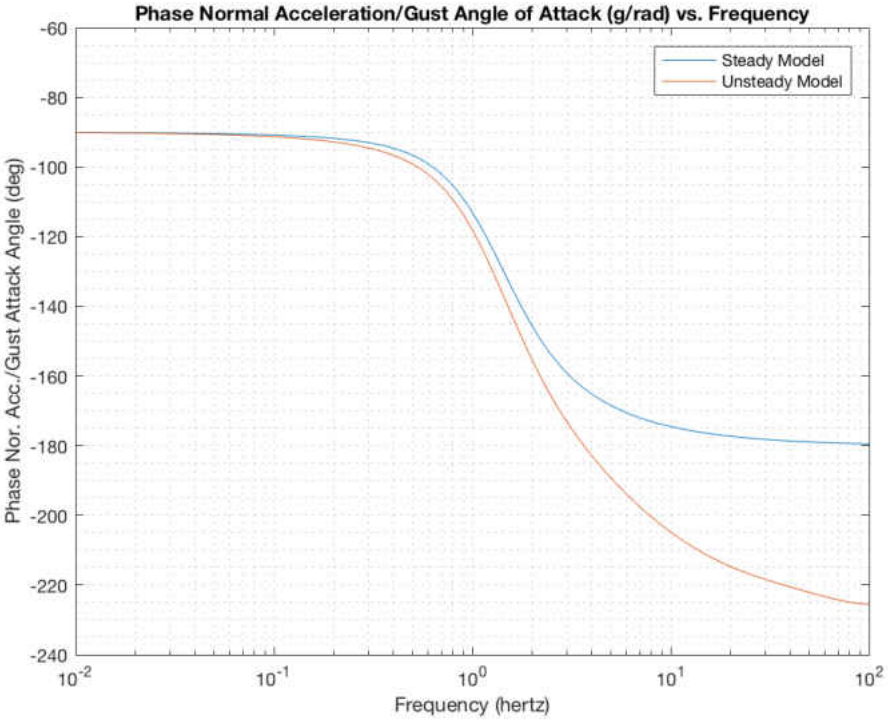

Figure 3.23 Normal Acceleration per Gust Angle of Attack Phase

Table 3.6 Flap Transfer Function Numerators: Steady Aero Model

Coefficient: $(s)\frac{rad}{s}$	Numerator of: $\left(\frac{\alpha}{\delta_f}\right)\frac{rad}{rad}$	Numerator of: $\left(\frac{q}{\delta_f}\right)\frac{rad/s}{rad}$	Numerator of: $\left(\frac{n_z}{\delta_f}\right)\frac{g}{rad}$
s^2	0	0	$-2.1508e+00$
s	$-1.1805e+00$	$-5.5211e+00$	$-1.5073e+01$
1	$-1.3794e+01$	$1.5515e+01$	$-2.8268e+01$

Table 3.7 Elevator Transfer Function Numerators: Steady Aero Model

Coefficient: $(s)\frac{rad}{s}$	Numerator of: $\left(\frac{\alpha}{\delta_e}\right)\frac{rad}{rad}$	Numerator of: $\left(\frac{q}{\delta_e}\right)\frac{rad/s}{rad}$	Numerator of: $\left(\frac{n_z}{\delta_e}\right)\frac{g}{rad}$
s^2	0	0	$-1.0763e+00$
s	$-5.9075e-01$	$-7.0370e+01$	$1.1762e+00$
1	$-6.9724e+01$	$-3.6138e+02$	$6.5841e+02$

Table 3.8 Wing Gust Transfer Function Numerators: Steady Aero Model

Coefficient: $(s)\frac{rad}{s}$	Numerator of: $\left(\frac{\alpha}{\alpha_{g_w}}\right)\frac{rad}{rad}$	Numerator of: $\left(\frac{q}{\alpha_{g_w}}\right)\frac{rad/s}{rad}$	Numerator of: $\left(\frac{n_z}{\alpha_{g_w}}\right)\frac{g}{rad}$
s^2	0	0	$-8.6031e+00$
s	$-4.7219e+00$	$1.9683e+01$	$-6.5680e+01$
1	$-1.6366e+01$	$2.9011e+02$	$-5.2857e+02$

Table 3.9 Body Gust Transfer Function Numerators: Steady Aero Model

Coefficient: $(s)\frac{rad}{s}$	Numerator of: $\left(\frac{\alpha}{\alpha_{g_b}}\right)\frac{rad}{rad}$	Numerator of: $\left(\frac{q}{\alpha_{g_b}}\right)\frac{rad/s}{rad}$	Numerator of: $\left(\frac{n_z}{\alpha_{g_b}}\right)\frac{g}{rad}$
s^2	0	0	$-3.4688e-01$
s	$-1.9039e-01$	$3.6163e+00$	$3.0123e+00$
1	$1.9630e+00$	$2.7110e+01$	$-4.9393e+01$

Table 3.10 Tail Gust Transfer Function Numerators: Steady Aero Model

Coefficient: $(s)\frac{rad}{s}$	Numerator of: $\left(\frac{\alpha}{\alpha_{g_t}}\right)\frac{rad}{rad}$	Numerator of: $\left(\frac{q}{\alpha_{g_t}}\right)\frac{rad/s}{rad}$	Numerator of: $\left(\frac{n_z}{\alpha_{g_t}}\right)\frac{g}{rad}$
s^2	0	0	$-9.9812e-01$
s	$-5.4783e-01$	$-6.1979e+01$	$6.6788e-01$
1	$-6.1613e+01$	$-3.1722e+02$	$5.7797e+0$

Table 3.11 Transfer Function Denominator: Steady Aero Model

Coefficient: $(s)\frac{rad}{s}$	Denominator:	~	~
s^2	$1.0000e+00$	~	~
s	$1.2800e+01$	~	~
1	$7.6016e+01$	~	~

Table 3.12 Flap Transfer Function Numerators: Unsteady Aero Model

Coefficient: $(s)\frac{rad}{s}$	Numerator of: $\left(\frac{\alpha}{\delta_f}\right)\frac{rad}{rad}$	Numerator of: $\left(\frac{q}{\delta_f}\right)\frac{rad/s}{rad}$	Numerator of: $\left(\frac{n_z}{\delta_f}\right)\frac{g}{rad}$
s^{13}	0	0	$-1.2044e+00$
s^{12}	$-6.6107e-01$	$-3.0918e+00$	$-2.1623e+03$
s^{11}	$-1.1899e+03$	$-5.5202e+03$	$-1.5937e+06$
s^{10}	$-8.8026e+05$	$-4.0368e+06$	$-6.3055e+08$
s^{9}	$-3.5015e+08$	$-1.5788e+09$	$-1.4872e+11$
s^{8}	$-8.3208e+10$	$-3.6611e+11$	$-2.2235e+13$
s^{7}	$-1.2570e+13$	$-5.3419e+13$	$-2.1832e+15$
s^{6}	$-1.2517+15$	$-5.0647e+15$	$-1.4295e+17$
s^{5}	$-8.3522e+16$	$-3.1500e+17$	$-6.2222e+18$
s^{4}	$-3.7301e+18$	$-1.2667e+19$	$-1.7566e+20$
s^{3}	$-1.0908e+20$	$-3.1312e+20$	$-3.0383e+21$
s^{2}	$-1.9807e+21$	$-4.1713e+21$	$-2.8660e+22$
s	$-1.9902e+22$	$-1.8305e+22$	$-1.1596e+23$
1	$-8.1953e+22$	$9.2178e+22$	$-1.6794e+23$

Table 3.13 Elevator Transfer Function Numerators: Unsteady Aero Model

Coefficient: $(s)\frac{rad}{s}$	Numerator of: $\left(\frac{\alpha}{\delta_e}\right)\frac{rad}{rad}$	Numerator of: $\left(\frac{q}{\delta_e}\right)\frac{rad/s}{rad}$	Numerator of: $\left(\frac{n_z}{\delta_e}\right)\frac{g}{rad}$
s^{13}	0	0	$-6.0273e-01$
s^{12}	$-3.3082e-01$	$-3.9407e+01$	$-1.0772e+03$
s^{11}	$-6.3063e+02$	$-7.0672e+04$	$-7.8845e+05$
s^{10}	$-5.0342e+05$	$-5.2012e+07$	$-3.0847e+08$
s^{9}	$-2.2132e+08$	$-2.0533e+10$	$-7.1421e+10$
s^{8}	$-5.9733e+10$	$-4.8274e+12$	$-1.0348e+13$
s^{7}	$-1.0507e+13$	$-7.1839e+14$	$-9.6137e+14$
s^{6}	$-1.2461e+15$	$-7.0068e+16$	$-5.6660e+16$
s^{5}	$-1.0117e+17$	$-4.5433e+18$	$-1.9575e+18$
s^{4}	$-5.6177e+18$	$-1.9484e+20$	$-2.6279e+19$
s^{3}	$-2.0926e+20$	$-5.3676e+21$	$6.9028e+20$
s^{2}	$-4.9887e+21$	$-8.8745e+22$	$3.6601e+22$
s	$-6.8656e+22$	$-7.5573e+23$	$6.2217e+23$
1	$-4.1424e+23$	$-2.1470e+24$	$3.9117e+24$

Table 3.14 Wing Gust Transfer Function Numerators: Unsteady Aero Model

Coefficient: $(s)\frac{rad}{s}$	Numerator of: $\left(\frac{\alpha}{\alpha_{g_w}}\right)\frac{rad}{rad}$	Numerator of: $\left(\frac{q}{\alpha_{g_w}}\right)\frac{rad/s}{rad}$	Numerator of: $\left(\frac{n_z}{\alpha_{g_w}}\right)\frac{g}{rad}$
s^{13}	0	0	$-7.4847e-01$
s^{12}	$-4.1081e-01$	$1.7124e+00$	$-2.4228e+03$
s^{11}	$-1.3281e+03$	$5.5552e+03$	$-2.5739e+06$
s^{10}	$-1.4071e+06$	$5.9278e+06$	$-1.3225e+09$
s^{9}	$-7.1994e+08$	$3.0669e+09$	$-3.7975e+11$
s^{8}	$-2.0537e+11$	$8.8965e+11$	$-6.5912e+13$
s^{7}	$-3.5287e+13$	$1.5662e+14$	$-7.2421e+15$
s^{6}	$-3.8183e+15$	$1.7541e+16$	$-5.1603e+17$
s^{5}	$-2.6569e+17$	$1.2813e+18$	$-2.3981e+19$
s^{4}	$-1.1881e+19$	$6.1407e+19$	$-7.1734e+20$
s^{3}	$-3.3232e+20$	$1.9023e+21$	$-1.3334e+22$
s^{2}	$-5.4162e+21$	$3.6401e+22$	$-1.4527e+23$
s	$-4.3332e+22$	$3.8723e+23$	$-8.8293e+23$
1	$-9.7373e+22$	$1.7261e+24$	$-3.1448e+24$

Table 3.15 Body Gust Transfer Function Numerators: Unsteady Aero Model

Coefficient: $(s)\frac{rad}{s}$	Numerator of: $\left(\frac{\alpha}{\alpha_{g_b}}\right)\frac{rad}{rad}$	Numerator of: $\left(\frac{q}{\alpha_{g_b}}\right)\frac{rad/s}{rad}$	Numerator of: $\left(\frac{n_z}{\alpha_{g_b}}\right)\frac{g}{rad}$
s^{13}	0	0	$-3.0178e-02$
s^{12}	$-1.6564e-02$	$3.1462e-01$	$-9.7718e+01$
s^{11}	$-5.3319e+01$	$1.0184e+03$	$-1.0388e+05$
s^{10}	$-5.5999e+04$	$1.0818e+06$	$-5.3439e+07$
s^{9}	$-2.8249e+07$	$5.5571e+08$	$-1.5375e+10$
s^{8}	$-7.8832e+09$	$1.5949e+11$	$-2.6775e+12$
s^{7}	$1.3101e+12$	$2.7651e+13$	$-2.9588e+14$
s^{6}	$-1.3474e+14$	$3.0310e+15$	$-2.1297e+16$
s^{5}	$-8.6582e+15$	$2.1490e+17$	$-1.0084e+18$
s^{4}	$-3.3857e+!7$	$9.8796e+18$	$-3.1275e+19$
s^{3}	$-7.2864e+18$	$2.8848e+20$	$-6.2575e+19$
s^{2}	$-5.4978e+19$	$5.0561e+21$	$-7.9457e+21$
s	$6.9504e+20$	$4.6758e+22$	$-6.3912e+22$
1	$1.1679e+22$	$1.6129e+23$	$-2.9387e+23$

Table 3.16 Tail Gust Transfer Function Numerators: Unsteady Aero Model

Coefficient: $(s)\frac{rad}{s}$	Numerator of: $\left(\frac{\alpha}{\alpha_{g_t}}\right)\frac{rad}{rad}$	Numerator of: $\left(\frac{q}{\alpha_{g_t}}\right)\frac{rad/s}{rad}$	Numerator of: $\left(\frac{n_z}{\alpha_{g_t}}\right)\frac{g}{rad}$
s^{13}	0	0	$-8.6837e-02$
s^{12}	$-4.7661e-02$	$-5.3922e+00$	$-2.8037e+02$
s^{11}	$-1.5928e+02$	$-1.7441e+04$	$-2.9623e+05$
s^{10}	$-1.8003e+05$	$-1.8499e+07$	$-1.5079e+08$
s^{9}	$-1.0126e+08$	$-9.4803e+09$	$-4.2614e+10$
s^{8}	$-3.2869e+10$	$-2.7111e+12$	$-7.1941e+12$
s^{7}	$-6.6597e+12$	$-4.6757e+14$	$-7.5205e+14$
s^{6}	$-8.8034e+14$	$-5.0869e+16$	$-4.8696e+16$
s^{5}	$-7.7596e+16$	$-3.5676e+18$	$-1.8376e+18$
s^{4}	$-4.5762e+18$	$-1.6143e+20$	$-2.9675e+19$
s^{3}	$-1.7772e+20$	$-4.6006e+21$	$4.5919e+20$
s^{2}	$-4.3485e+21$	$-7.7472e+22$	$3.0691e+22$
s	$-6.0627e+22$	$-6.6412e+23$	$5.4212e+23$
1	$-3.6657e+23$	$-1.8873e+24$	$3.4386+24$

Table 3.17 Transfer Function Denominator: Unsteady Aero Model

Coefficient: $(s)\frac{rad}{s}$	Denominator:	~	~
s^{13}	$1.0000e+00$	~	~
s^{12}	$1.7752e+03$	~	~
s^{11}	$1.2887e+06$	~	~
s^{10}	$4.9944e+08$	~	~
s^{9}	$1.1469e+11$	~	~
s^{8}	$1.6617e+13$	~	~
s^{7}	$1.5778e+15$	~	~
s^{6}	$1.0017e+17$	~	~
s^{5}	$4.2720e+18$	~	~
s^{4}	$1.2103e+20$	~	~
s^{3}	$2.2104e+21$	~	~
s^{2}	$2.4629e+22$	~	~
s	$1.5330e+23$	~	~
1	$4.5226e+23$	~	~

3.6 Control Law Derivation

The next problem to address was to solve for the proper gains of the control surfaces with respect to a gust input, using the gust alleviation control system architecture described in Figure 2.4 and Table 2.2. To achieve this calibration, a step gust fixed in space that the vehicle would pass through was considered. The magnitude of the gust would be solved for to effectively cause one g of normal acceleration ($n_z = 1$). After solving for the gust angle of attack, the linear and angular accelerations caused by the gust on the lifting surfaces, i.e., the wing, body, and tail, were generated using the stability derivatives. Although the wing and the body's aerodynamic centers do not coincide, the body's linear acceleration is small compared to that of the wing, so these terms were simply summed. Following this step, the necessary flap deflection (δ_f) to oppose the summed wing and body acceleration (Z_{w+b}), was solved for. Next, the proper deflection of the elevator (δ_{e1}), to equal out the summed angular accelerations of the wing and body caused by gust and flap (M_{w+b+f}), was calculated. Finally, the angular acceleration generated by the tail from the step gust (M_t) was solved for, from which the necessary elevator deflection (δ_{e2}) to generate equal and opposite angular acceleration was determined. Necessary gains for the control laws were computed by considering the ratio of the deflection magnitude to the gust angle of attack. All gain calculations are indicated below.

$$\alpha_g = \frac{g}{Z_\alpha} = -9.7872e-02\ rad \tag{3.6-1}$$

$$Z_{w+b} = \left(\frac{Z_{\alpha_w}}{V_{cm} - Z_{\dot{\alpha}}} + \frac{Z_{\alpha_b}}{V_{cm} - Z_{\dot{\alpha}}}\right)\alpha_g = 0.4808\ \frac{ft}{s^2} \tag{3.6-2}$$

$$\delta_f = -\frac{Z_{w+b}}{\frac{Z_{\delta_f}}{V_{cm} - Z_{\dot{\alpha}}}} = 4.0727e-01\ rad \tag{3.6-3}$$

$$k_f = \frac{\delta_f}{\alpha_g} = -4.1613\ \frac{rad}{rad} \tag{3.6-4}$$

$$M_{w+b+f} = \left(M_{\alpha_w} + \left(\frac{M_{\dot{\alpha}} Z_{\alpha_w}}{V_{cm} - Z_{\dot{\alpha}}}\right) + M_{\alpha_b} + \left(\frac{M_{\dot{\alpha}} Z_{\alpha_b}}{V_{cm} - Z_{\dot{\alpha}}}\right)\right)\alpha_g + \left(M_{\delta_f} + \left(\frac{M_{\dot{\alpha}} Z_{\delta_f}}{V_{cm} - Z_{\dot{\alpha}}}\right)\right)\delta_f = -4.5289\ \frac{rad}{s^2} \tag{3.6-5}$$

$$\delta_{e1} = -\frac{M_{w+b+f}}{M_{\delta_e} + \left(\frac{M_{\dot{\alpha}} Z_{\delta_e}}{V_{cm} - Z_{\dot{\alpha}}}\right)} = -6.4359e-02\ rad \tag{3.6-6}$$

$$k_{e1} = \frac{\delta_{e1}}{\alpha_g} = 0.6576\ \frac{rad}{rad} \tag{3.6-7}$$

$$M_t = \left(M_{\alpha_t} + \left(\frac{M_{\dot{\alpha}} Z_{\alpha_t}}{V_{cm} - Z_{\dot{\alpha}}}\right)\right)\alpha_g = 6.066\ \frac{rad}{s^2} \tag{3.6-8}$$

$$\delta_{e2} = -\frac{M_t}{M_{\delta_e} + \left(\frac{M_{\dot{\alpha}} Z_{\delta_e}}{V_{cm} - Z_{\dot{\alpha}}}\right)} = 8.6202e-02\ rad \tag{3.6-9}$$

$$k_{e2} = \frac{\delta_{e2}}{\alpha_g} = -0.8808\ \frac{rad}{rad} \tag{3.6-10}$$

The final control law scheme matching Table 2.2 for the AFM system was represented in Equation (3.6-11). Note, here, the gust sensor signal is equated and negated to the gust angle of attack, which assumes an ideal sensor model. Sensor dynamics are considered next. Also note the second elevator term is delayed by the time Δt to account for delayed gust penetration effects, which is also considered next.

$$\delta_{gs}(t) = -\alpha_g(t) \tag{3.6-11}$$

$$\delta_f(t) = -4.1613\ \delta_{gs}(t)$$

$$\delta_e(t) = 0.6576\ \delta_{gs}(t) - 0.8808\ \delta_{gs}(t - \Delta t)$$

3.7 Forward Gust Sensor Transfer Function

To accurately describe the dynamic responses and the inherent time lags of the forward gust sensor, an estimated transfer function was needed. The sensor was put into ViGYAN's low speed wind tunnel and pull pin tests were performed. The tunnel was run with the same dynamic pressure as would be experienced during flight testing. The sensor was deflected roughly six degrees, and a pin was placed to hold it in the same position. Once the pin was quickly removed, the sensor reacted to the wind velocity and returned to its steady state value. The recorded data was uploaded and input into MATLAB's system identification toolbox. Both the numerical and the graphical transfer functions are given below, where s has units of rad/s.

$$\frac{\delta_{gs}}{\alpha_g}(s) = \frac{-12399}{s^2 + 55s + 12399}\ \frac{rad}{rad} \tag{3.7-1}$$

After comparison of Figures 3.24 - 3.26 with Figures 3.6 - 3.23, note that the gust sensor dynamics are approximately one order of magnitude faster than the airframe dynamics, but they still could be significant and necessary for accurate prediction of motion responses. Further, to achieve maximum gust alleviation performance, these sensor dynamics should be considered. Finally, note that the inherent damping of the gust sensor is somewhat deficient and may require improvement.

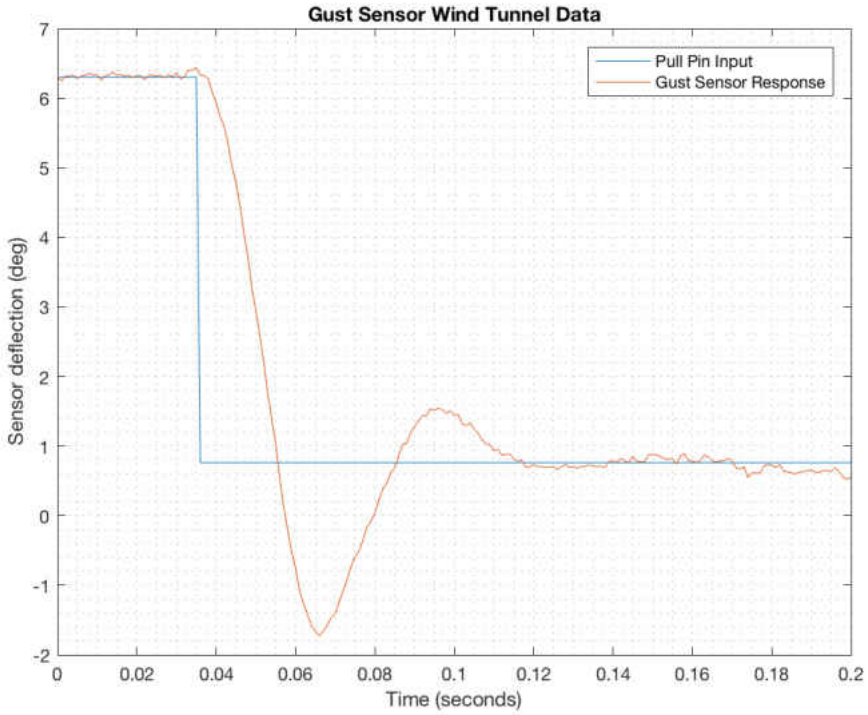

Figure 3.24 Forward Gust Sensor Wind Tunnel Data

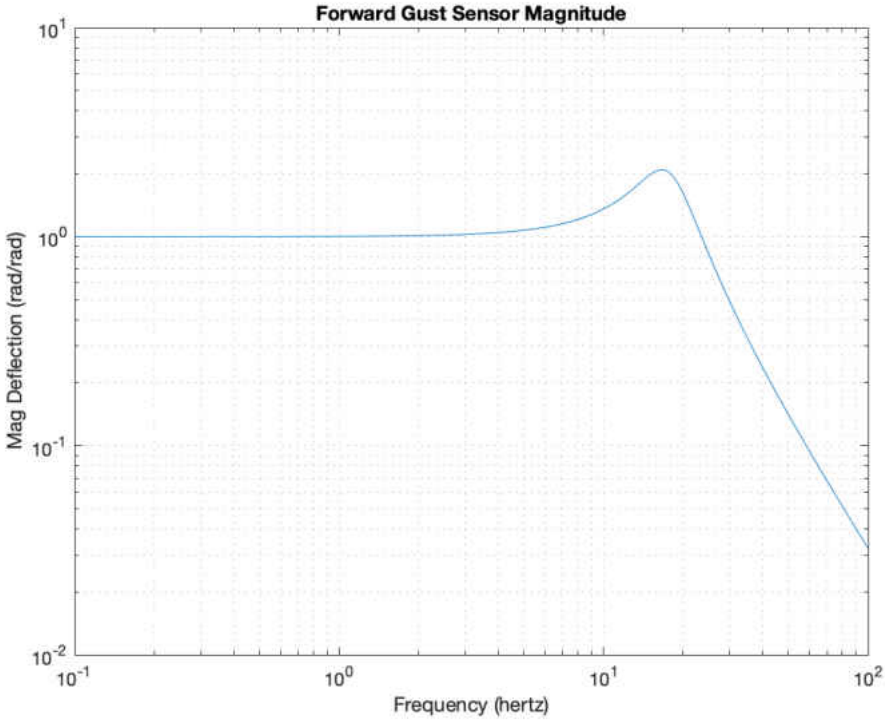

Figure 3.25 Forward Gust Sensor Estimated Magnitude

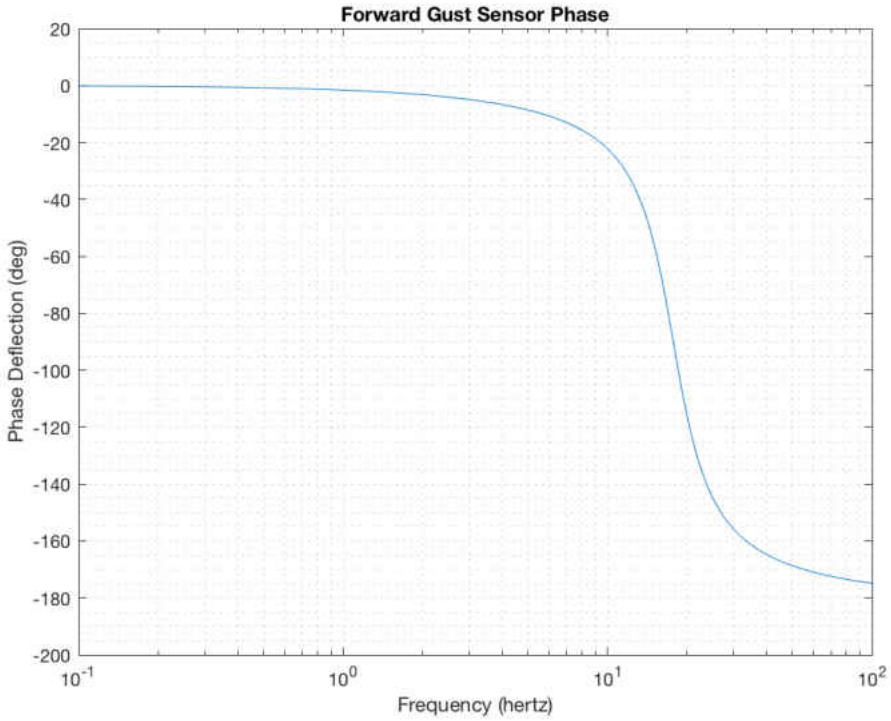

Figure 3.26 Forward Gust Sensor Estimated Phase

3.8 Control Surface Delay Times

Control surface deflection response times must be considered, as they have proven to be one of the limiting factors for past researchers in the gust alleviation area. During the same wind tunnel test that was used to derive the forward gust sensor's transfer function, the flap was connected to the same data system to test its response times. The flap is actuated by the electric servo motor described in Section 2.1. Figure 3.27 shows both the flap deflection and the gust sensor responses to the pull pin test. Observe that the actuated flap motion is delayed, relative to the sensed bird signal, by approximately 15 milliseconds at the peaks, even for a deflection with displacement of 35 degrees. Although 15 milliseconds may seem a small amount of time, this lag directly impacts the achievable gust alleviation performance. Also, it is

noteworthy that the forward gust sensor will not be able to fully respond to high frequencies of gust, over 16 hertz, meaning that the control surfaces inherently will not, either, since they respond directly to the gust sensor. For this reason, no transfer function was estimated for the control surface delay times, meaning that the flap would move with appropriate gains approximately 15 milliseconds, or 5 time steps, behind the sensor, within a bandwidth of 16 hertz.

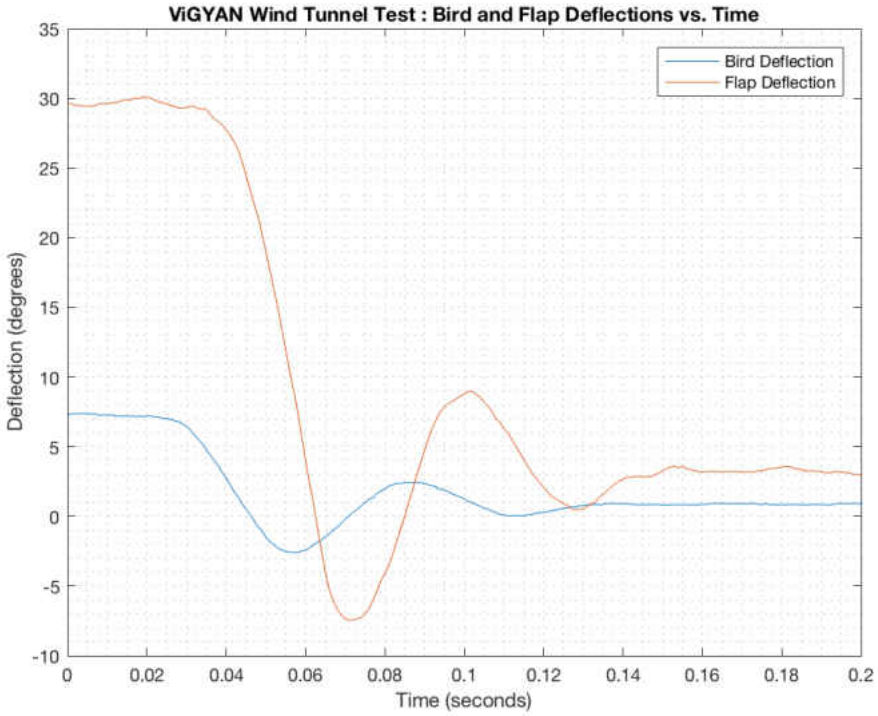

Figure 3.27 Wind Tunnel Test Bird and Flap Response

4 ANALYSIS AND RESULTS

This chapter will cover results from the linear simulations of the mathematical model for the AFM 1.5 in response to the selected wind fields, with and without the gust alleviation control system. Analyzed wind fields included the step gust, the doublet gust, and von Karman turbulence. All simulations were run at the maximum allowable frequency of the system, 333 hertz. This rate produces a three millisecond time step. To describe gust penetration sequencing, the reference "zero" time step will be used in relation to the gust hitting the forward sensor. The inputs to the lifting surfaces, wing, body, and tail, will be selected to the nearest time step of the actual time of the wind field hitting their aerodynamic centers. The first gust flap motion and the first elevator motion will begin one additional time step behind that of the delayed forward gust sensor initial excitation, to account for the pulse width modulation. The delay time for the second elevator motion was iteratively solved for, using the step gust input simulation. The optimum delay time was found to be the 17^{th} time step, and this was used throughout the analysis. The step and doublet gust responses were examined, with and without control activation. Next, the random turbulence wind field shown in Chapter 2 was inputted to the math model for linear simulations in controls fixed and active modes. Also, it was seen that the second elevator gain could be further optimized to achieve improved alleviations in turbulent disturbance environments. These two sets of stochastic results will be compared by means of visual peak inspections, standard deviations, and power spectral analyses.

4.1 Step Response

Determination of elevator delay time was considered first. Using a 3 degree step gust disturbance, the airframe motions with active controls were generated from linear simulation with a varying elevator delay time. Table 4.1 shows the delay times, the corresponding mean pitch rate, and the normal load factor values. Note that the delay time parameter can have a large influence on gust alleviation performance. Based on the results of varying the delay time of the second elevator motion, the 17th time step was chosen as the most adequate for reducing normal acceleration and pitch rate. The 17th time step corresponded to 51 milliseconds after the simulation began, or when the gust came in contact with the sensor. It is important to note that, due to lags in the gust sensor and to the control surface response times, the 5th time step is the first possible motion. This step is the time of the flap control motion and first elevator motion.

Table 4.1 Determination of Optimum Elevator Delay Time

Δt (step #)	Δt (ms)	Mean q $\left(\frac{rad}{s}\right)$	Mean n_z (g)
5	15	$5.5664e-03$	$-1.9919e-02$
6	18	$4.6388e-03$	$-1.8188e-02$
7	21	$3.7110e-03$	$-1.6456e-02$
8	24	$2.7828e-03$	$-1.4723e-02$
9	27	$1.8542e-03$	$-1.2990e-02$
10	30	$9.2533e-04$	$-1.1256e-02$
11	33	$-3.9605e-06$	$-9.5210e-03$

Δt (step #)	Δt (ms)	Mean q $\left(\frac{rad}{s}\right)$	Mean n_z (g)
12	36	$-9.3364e-04$	$-7.7854e-03$
13	39	$-1.8637e-03$	$-6.0491e-03$
14	42	$-2.7943e-03$	$-4.3121e-03$
15	45	$-3.7252e-03$	$-2.5744e-03$
16	48	$-4.6567e-03$	$-8.3589e-04$
17	51	$-5.5886e-03$	$9.0334e-04$
18	54	$-6.5210e-03$	$2.6433e-03$
19	57	$-7.4540e-03$	$4.3840e-03$
20	60	$-8.3875e-03$	$6.1255e-03$
21	63	$-9.3215e-03$	$7.8677e-03$
22	66	$-1.0256e-02$	$9.6106e-03$
23	69	$-1.1191e-02$	$1.1354e-02$
24	72	$-1.2127e-02$	$1.3099e-02$
25	75	$-1.3064e-02$	$1.4844e-02$
26	78	$-1.4001e-02$	$1.6590e-02$

Figure 4.1 shows the control surface responses to the 3 degree step gust input. As previously derived, the first control motions follow the forward gust sensor with their inherent 15 millisecond delays. Two curves, with and without the second elevator motion, are shown, which depart from one another after another 51 milliseconds have occurred. Upon visual inspection of the airframe time histories

given in Figures 4.2, 4.3, and 4.4, for the step gust input comparisons, the effectiveness of the gust alleviation system can be clearly seen. The AFM 1.5's angle of attack response to the step input is all but eliminated (see Figure 4.2). The short period response for pitch rate was an order of magnitude smaller for controls active, while damping to steady state in approximately one-third of the time (see Figure 4.3). Note that there was a residual pitch rate created by the control surfaces for a period of time that may have led to phugoid effects. The largest peak of normal acceleration for controls active reaches roughly fifty percent of the corresponding peak of controls fixed (see Figure 4.4). The gust alleviation system also aids in reaching the steady state of normal acceleration in roughly half of the time it takes the vehicle with the controls fixed.

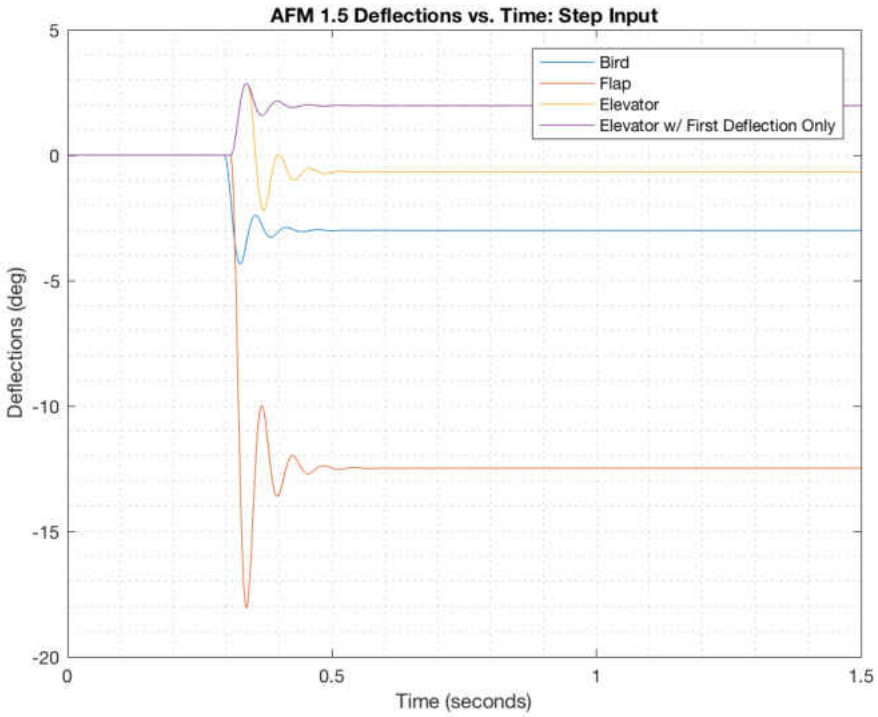

Figure 4.1 Step Gust Sensor and Control Surface Deflections

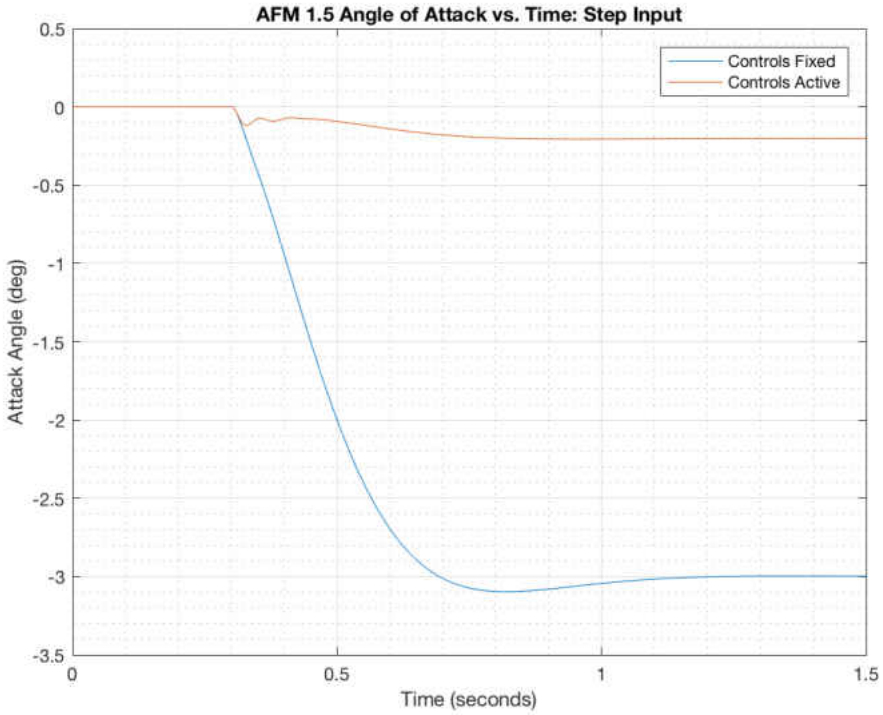

Figure 4.2 Step Gust Angle of Attack Response

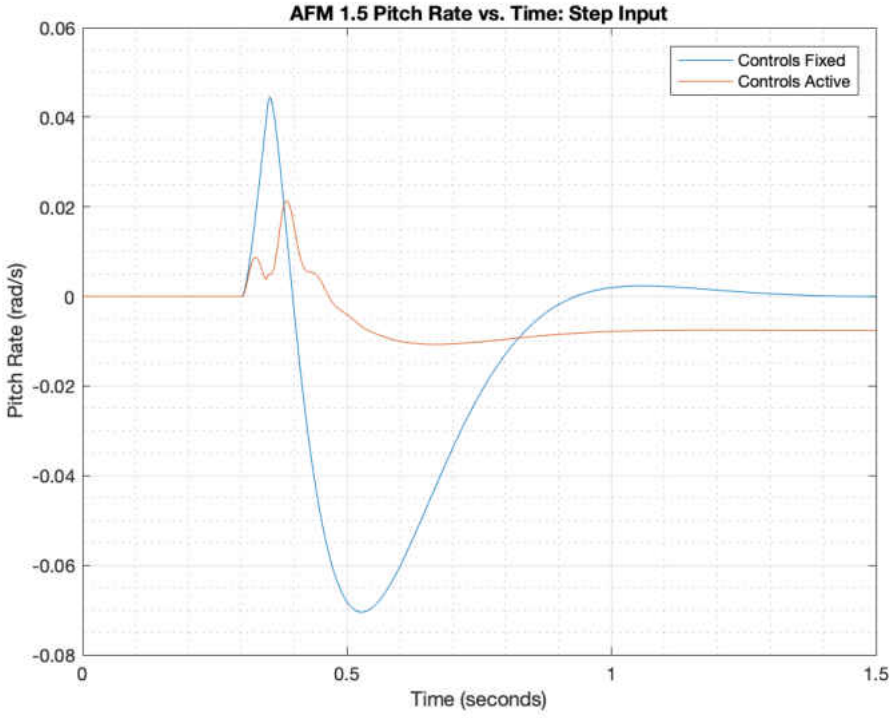

Figure 4.3 Step Gust Pitch Rate Response

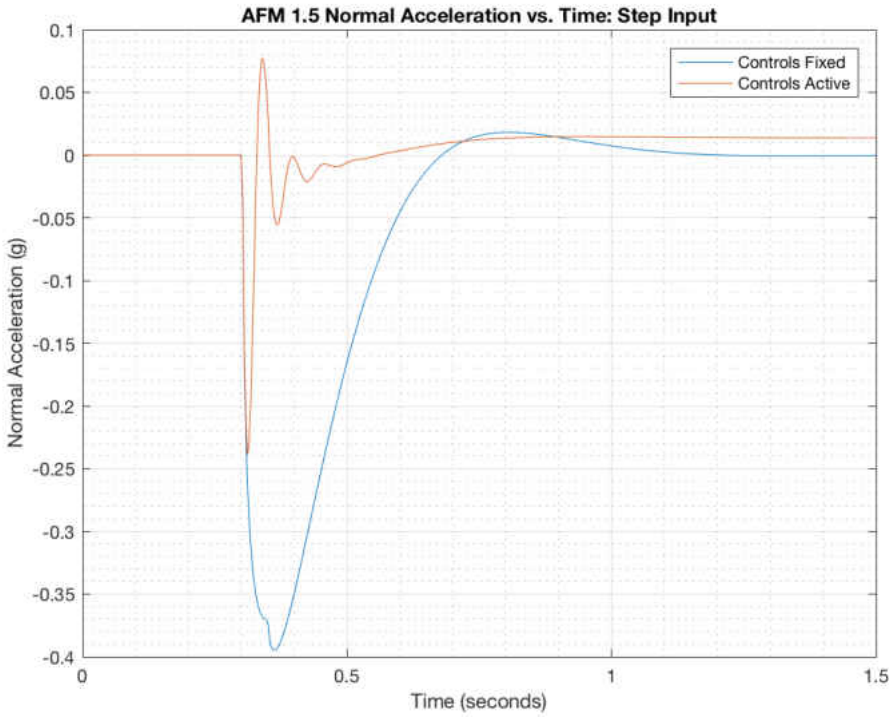

Figure 4.4 Step Gust Normal Acceleration Response

4.2 Doublet Response

The doublet response is included in the analysis as a precursor to the random turbulence input. This response is important to the analysis, due to the fact that the gust input changes signs multiple times. This feature allows closer inspection of the aircraft's damping abilities to a more chaotic input. All of the simulations are run with the same parameter values, as in the previous section. The doublet amplitude is $\pm$ 3 degrees, with total duration of 0.3 seconds (see Figure 2.9). Figures 4.5 - 4.8 show the surface deflections and the aircraft response.

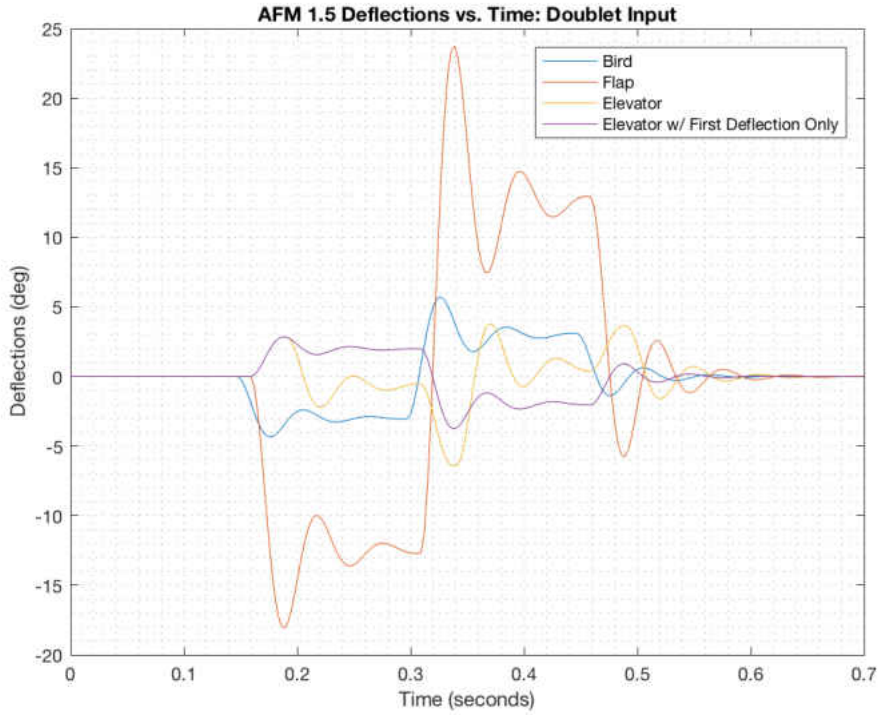

Figure 4.5 Doublet Gust Sensor and Control Surface Deflections

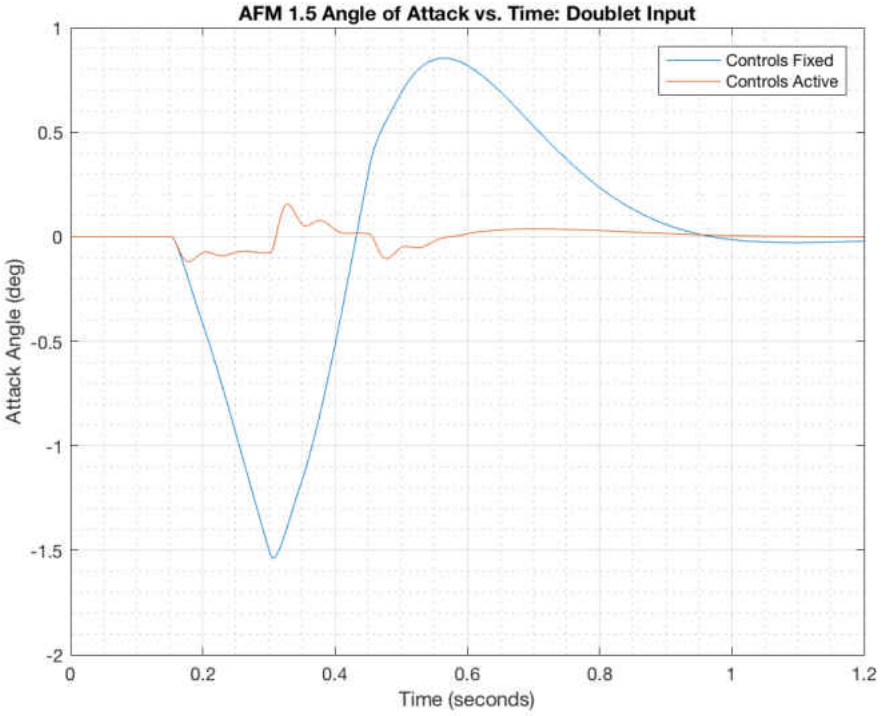

Figure 4.6 Doublet Gust Angle of Attack Response

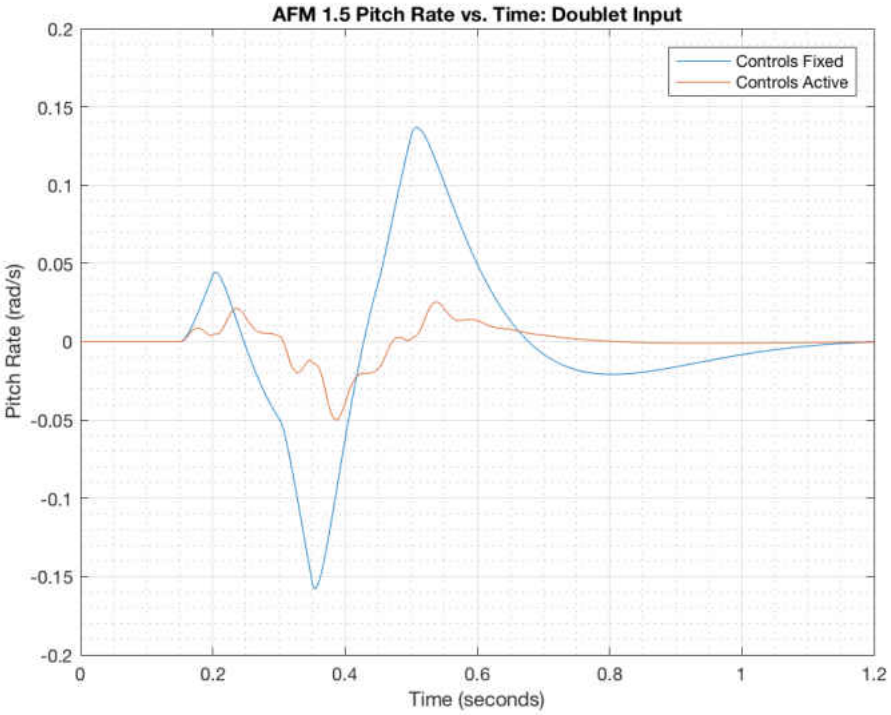

Figure 4.7 Doublet Gust Pitch Rate Response

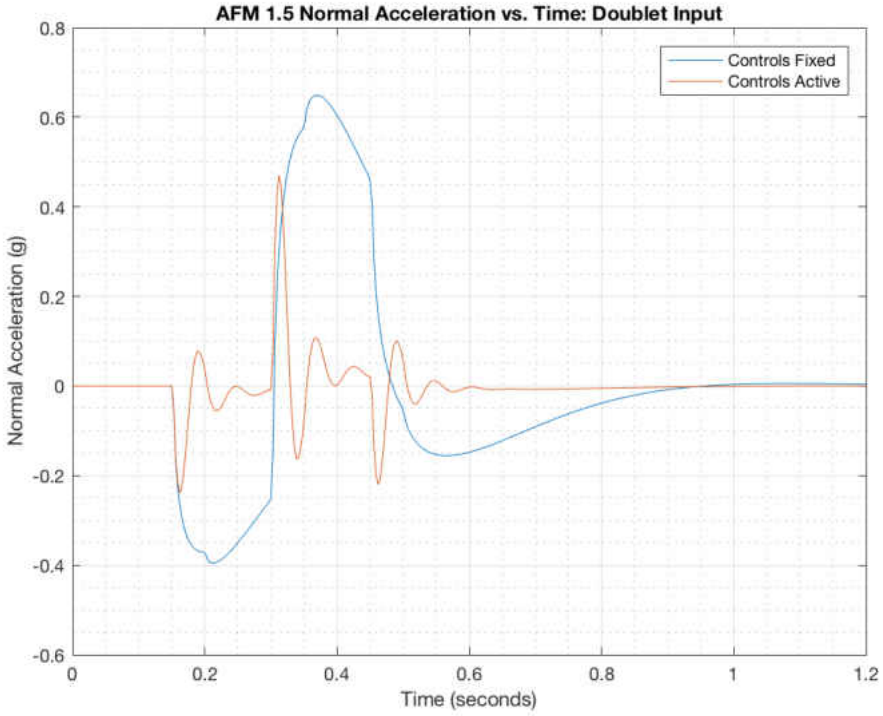

Figure 4.8 Doublet Gust Normal Acceleration Response

As with the step gust, promising results are shown. Again, the angle of attack change from the gust perturbation is all but eliminated (see Figure 4.6). The peaks of pitch rate for controls active are reduced by 80 percent, compared to those of controls fixed (see Figure 4.7). Normal acceleration, however, shows a controls active peak with only 25 percent alleviation improvement (see Figure 4.8). This shows that the ride of the passenger would be far superior, with this system in place. Further, the average normal acceleration level is far less with controls active. In Figure 4.5, the required surface deflections are identical for the first half of the gust encounter, and then are reflected in sign and amplified, but with similar shape for the second half of the gust encounter. Note that the +3 to -3 degree gust angle change requires approximately 35 degrees of change in the flap angle, but the peak deflection is still within the upper 30 degree travel limit. The abrupt change in flap deflection at this time will require quick responding flap actuators to achieve the predicted gust alleviation performance.

4.3 Random Turbulence

This section will show how the model responds to a stochastic environment, specifically the von Karman turbulence time series previously shown in Figure 2.11 with a 2 feet per second gust velocity standard deviation and a scale length of 300 feet. Control motions will be shown, as well as the forward gust sensor's response to the input, in Figures 4.9 to 4.11. Visual inspection of angle of attack, pitch rate, and normal accelerations alleviations will be seen in Figures 4.12, 4.13, and 4.14. To further define the amount of pitch rate and normal acceleration alleviation, standard

deviations of controls fixed and active cases will be compared for the motion sickness range region of 0.1 to 0.7 hertz. Power spectra are also shown in Figures 4.15, 4.16, and 4.17, for a visual inspection of the frequency analysis.

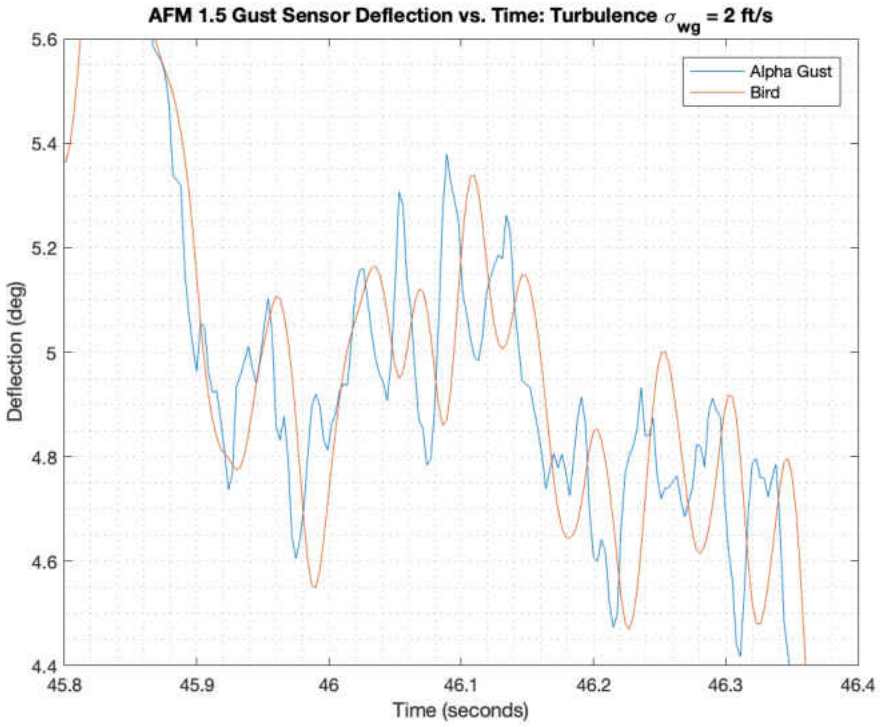

Figure 4.9 von Karman Turbulence Gust Sensor Response

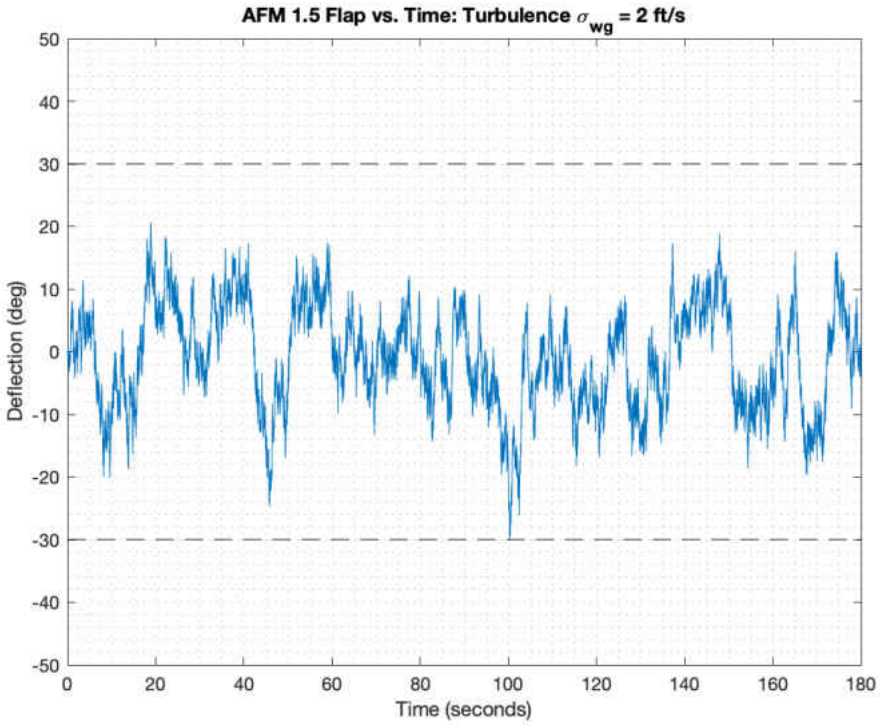

Figure 4.10 von Karman Turbulence Flap Response

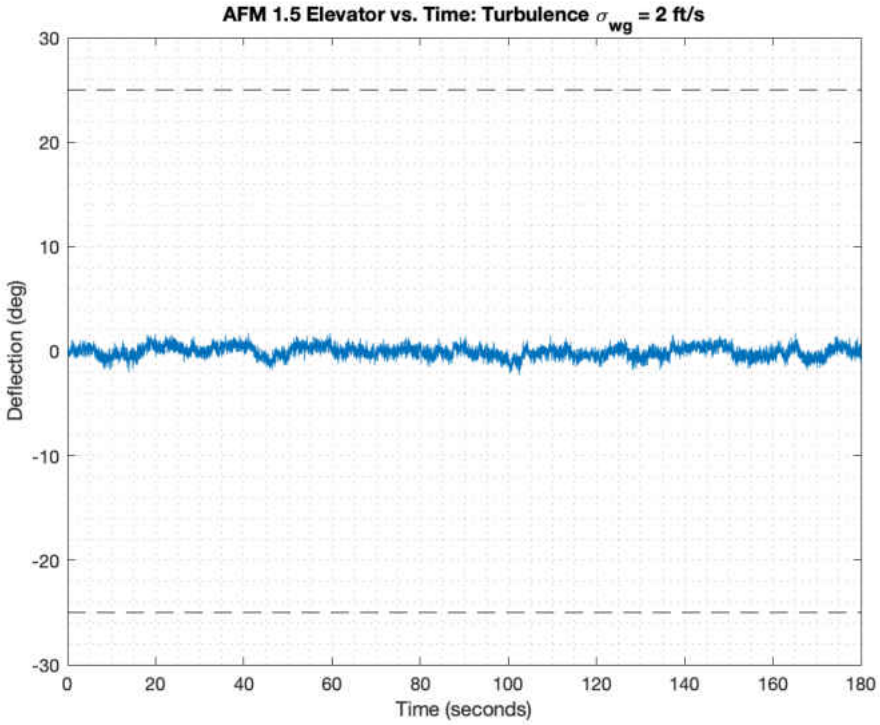

Figure 4.11 von Karman Turbulence Elevator Response

Figure 4.9 shows the comparison of the gust angle of attack and the negative of the forward gust sensor's response. As expected from visual inspection of the sensor's transfer function, the J-Bird cannot keep up with the high frequency --over 17 hertz -- changes in the gust angle of attack. However, the general trend follows rather well, yielding an average difference between the two curves, over the three minute simulation, of 0.15 degrees. Figures 4.10 and 4.11 show the gust flap and the elevator deflections, respectively, over the entirety of the three minute simulation. These plots are important to note, because they show that both control surfaces stay well within their given mechanical limits of 30 and 25 degrees.

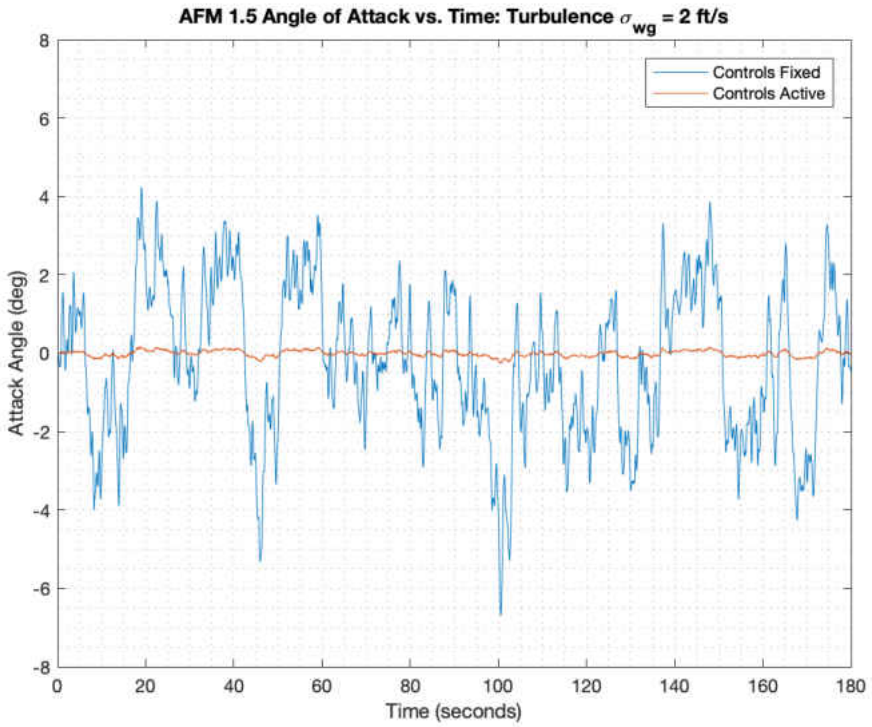

Figure 4.12 von Karman Turbulence Angle of Attack Response

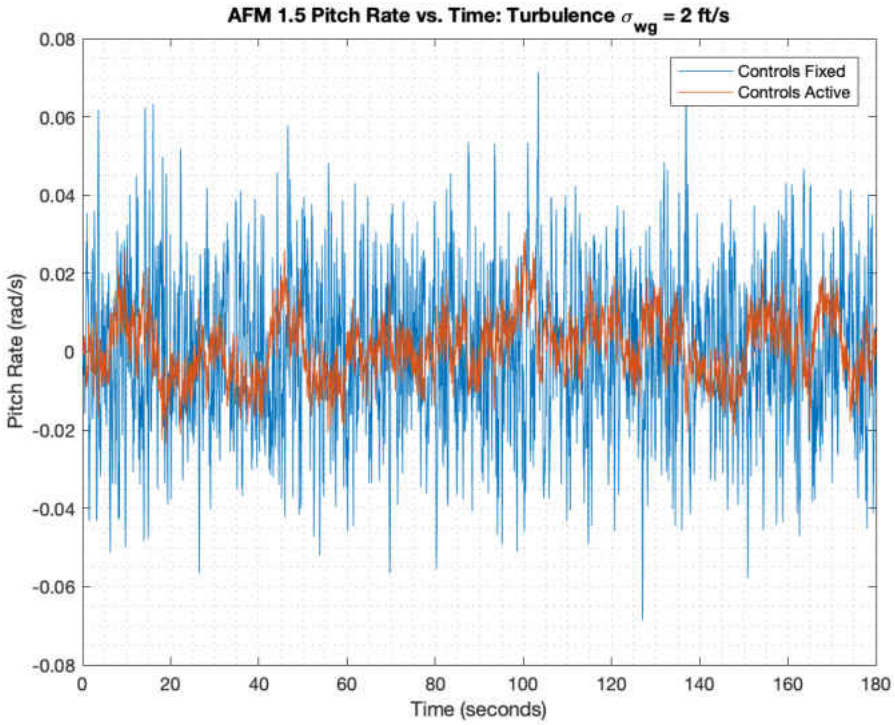

Figure 4.13 von Karman Turbulence Pitch Rate Response

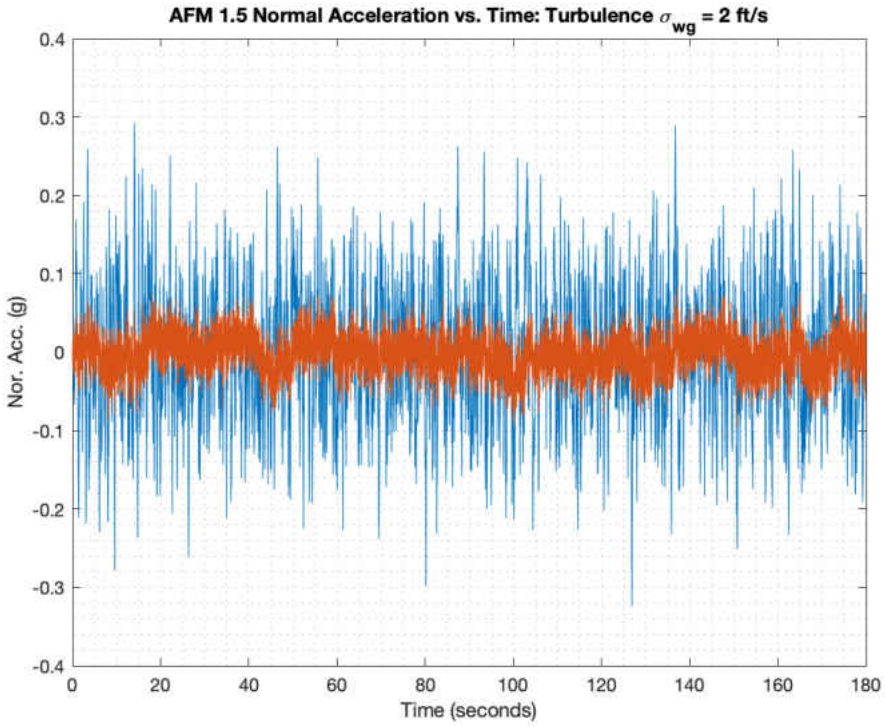

Figure 4.14 von Karman Turbulence Normal Acceleration Response

Table 4.2 von Karman Turbulence Alleviation Performance

Response	Controls Fixed	Controls Active	Alleviation
Pitch Rate	0.0101 rad/s	0.0038 rad/s	62.38 %
Normal Acceleration	0.0420 g	0.0077 g	81.67 %

Table 4.2 provides a description of the pitch rate and the normal acceleration gust alleviation performance provided by the control system. While the percent of root mean square (RMS) reduction in pitch rate is not as significant as that of normal acceleration, controls active case still yields a 62 percent reduction, in comparison to the controls fixed case. Normal acceleration yields nearly an order of magnitude reduction, at 81 percent. Closer examination of Figures 4.13 and 4.14 shows that all major peaks are eliminated, yielding a far more comfortable ride for the passenger. No statistical analysis is needed for angle of attack, since the response is approximately fully suppressed, as seen in Figure 4.12.

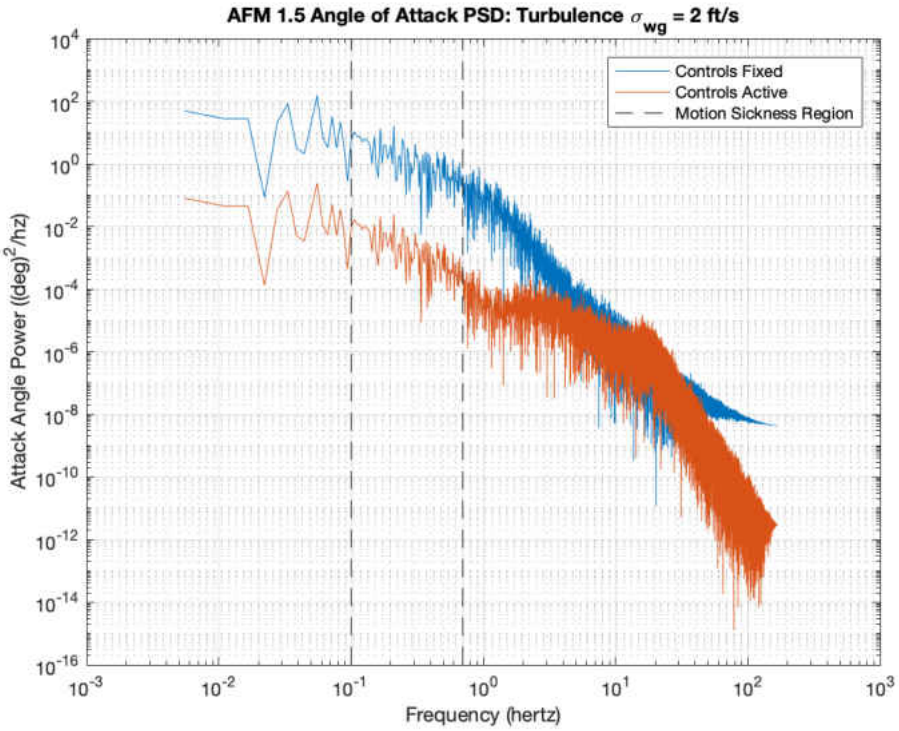

Figure 4.15 von Karman Turbulence Angle of Attack PSD

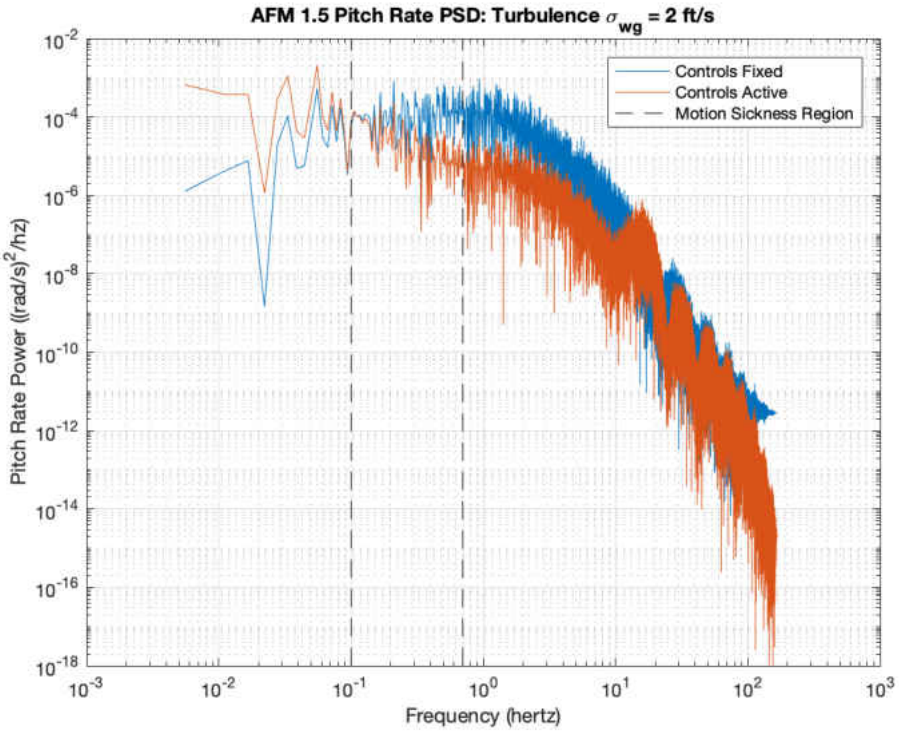

Figure 4.16 von Karman Turbulence Pitch Rate PSD

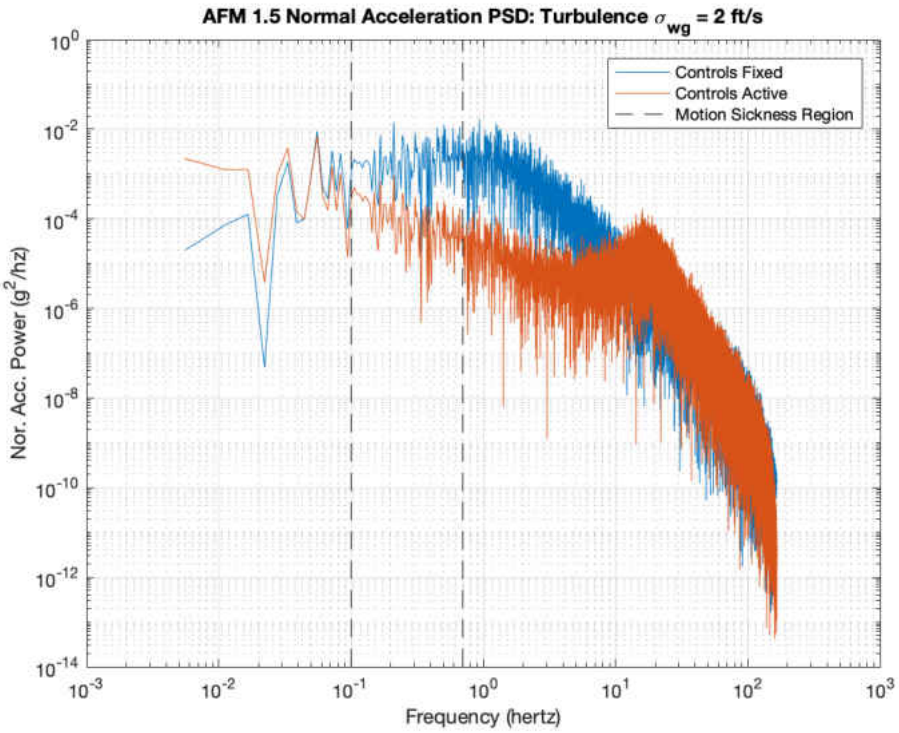

Figure 4.17 von Karman Turbulence Normal Acceleration PSD

The angle of attack power spectral density (PSD) comparisons of the two cases, as with the time histories, show multiple orders of reduction at lower frequencies and approach the controls fixed value as it reaches 10 to 20 hertz (see Figure 4.15). The power spectral densities of normal acceleration and pitch rate show extensive decreases in the frequency range of 0.1 to 10 hertz in Figures 4.17 and 4.16, respectively. The suspected mechanism behind all three controls active power spectrums approaching and overlapping the controls fixed power spectrums around 10 to 20 hertz is due to the forward gust sensor limitations. This frequency range coincides with the resonance frequency range of the sensor, where the measurement device begins to lose its ability to track gust behaviors beyond this frequency. The lower frequency deficiencies seen in the figures will be addressed in Section 4.4.

4.4 Random Turbulence with Adjusted Elevator Gain

With an original goal of reaching nearly an order of magnitude reduction in normal acceleration and pitch rate, an iterative process was conducted to adjust the second elevator gain k_{e2}. It was found that Equation (4.4-1) yielded the optimal gust alleviation control law for this specific von Karman turbulence time series. This gain value was changed from the original value of -0.8808 rad/rad (see Equation (3.6-11)) to the new value of -0.8450 rad/rad in Equation (4.4-1). This gain adjustment also aided in eliminating the low frequency inefficiencies seen in Section 4.3. Control surface deflection plots for the new control law responses were not included, as the elevator and flap responses are not visually different from those seen in Figures 4.10 and 4.11. As presented in the previous section, control fixed and active cases will be plotted for the three airframe time responses followed by the power spectrums. A table of alleviation performance values for pitch rate and normal acceleration was also included, Table 4.3.

$$\begin{aligned} \delta_{gs}(t) &= -\alpha_g(t) \\ \delta_f(t) &= -4.1613\ \delta_{gs}(t) \\ \delta_e(t) &= 0.6576\ \delta_{gs}(t) - 0.8450\ \delta_{gs}(t - \Delta t) \end{aligned} \tag{4.4-1}$$

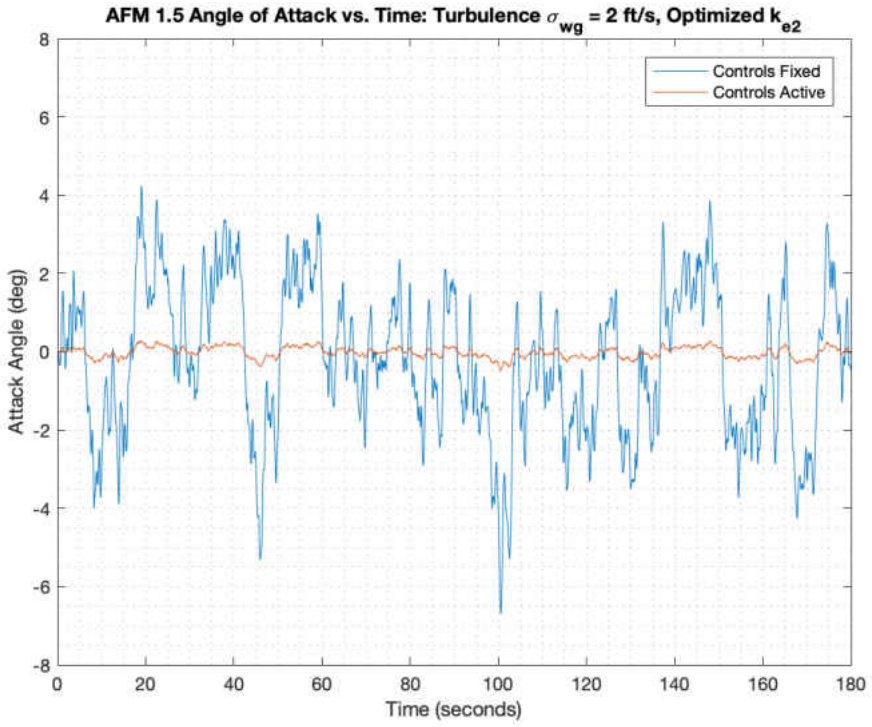

Figure 4.18 von Karman Turbulence Angle of Attack Response, Optimized

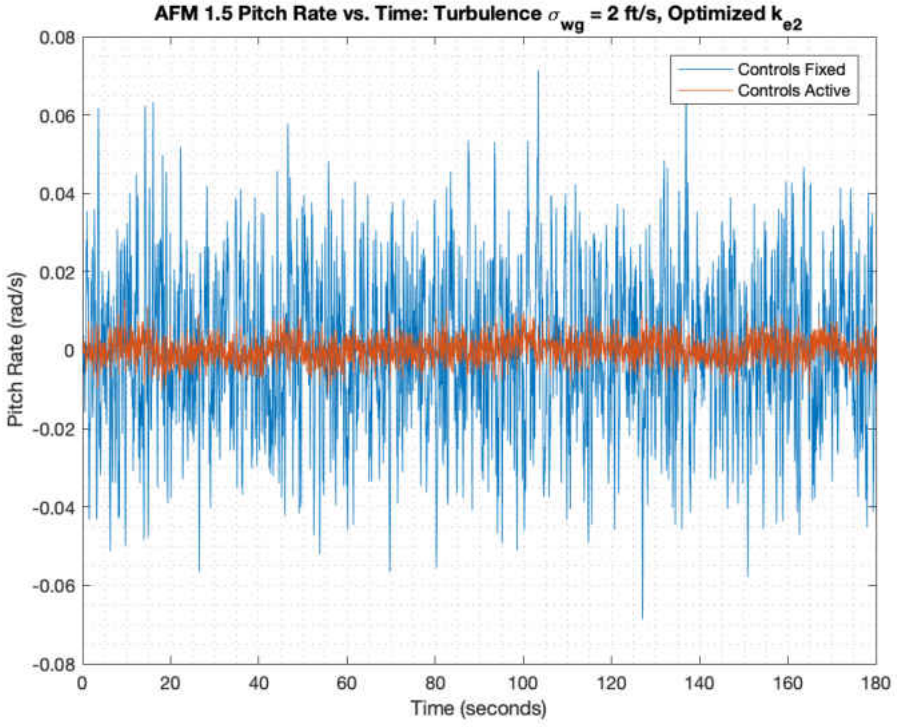

Figure 4.19 von Karman Turbulence Pitch Rate Response, Optimized

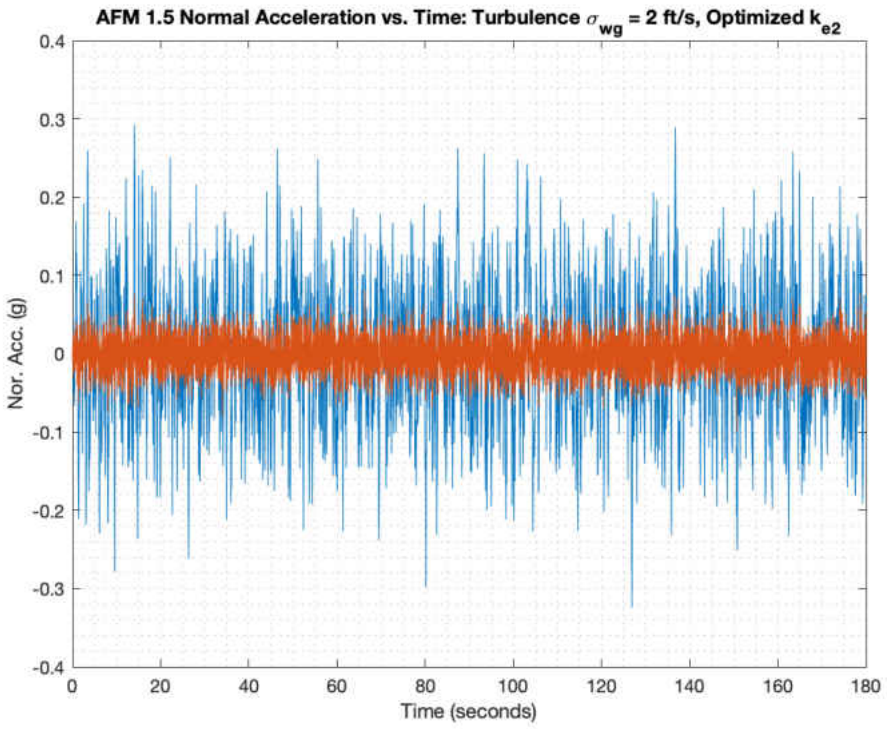

Figure 4.20 von Karman Turbulence Normal Acceleration Response, Optimized

Table 4.3 von Karman Turbulence Optimized Alleviation Performance

Response	Controls Fixed	Controls Active	Alleviation
Pitch Rate	0.0101 rad/s	0.0009 rad/s	91.09 %
Normal Acceleration	0.0420 g	0.0055 g	86.90 %

The results, using the optimized elevator gain from Table 4.3, show an order of magnitude reduction in pitch rate and nearly an order of magnitude in normal acceleration for the controls active case, compared to the controls fixed case. This improvement achieves the theoretical goals of the ARIS project at ViGYAN. Figures 4.21 through 4.23 show that the low frequency inefficiencies from Section 4.3 are eliminated, yielding the improved alleviations. With the original gain value, the elevator was overdriving the pitch acceleration slightly, causing the controls active

power to be above the controls fixed power at low frequency, as shown in Figure 4.16. In comparison, by a small reduction in elevator gain k_{e2}, the elevator induced pitch acceleration, was better matched to the gust induced pitch acceleration, causing the controls active power to fall below the controls fixed power at the low frequencies, as shown in Figure 4.22. No deficiencies occurred from this change at the higher frequencies.

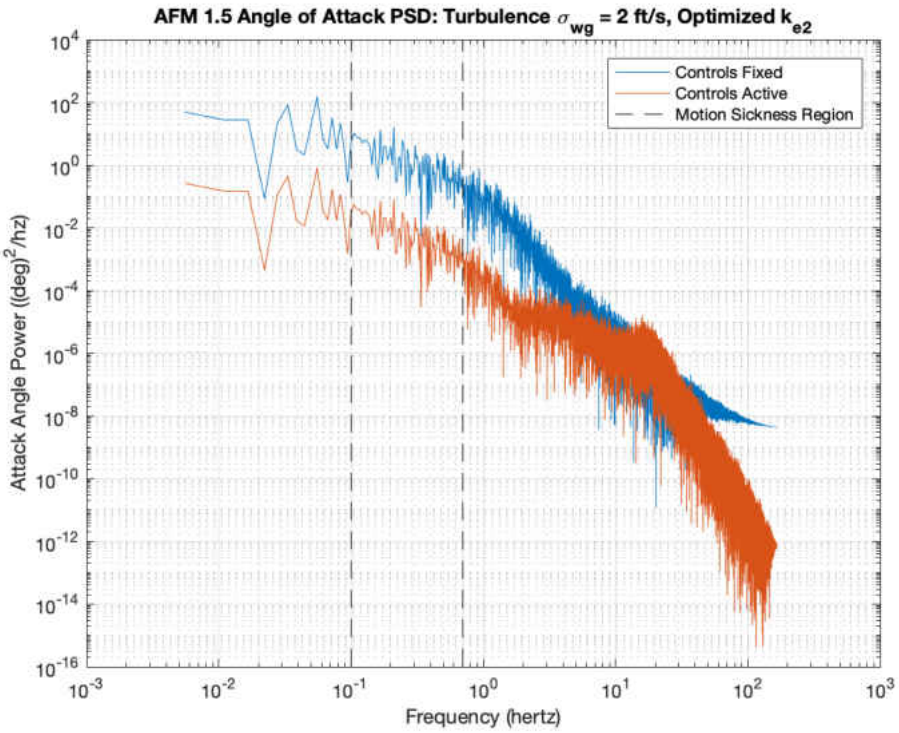

Figure 4.21 von Karman Turbulence Angle of Attack PSD, Optimized

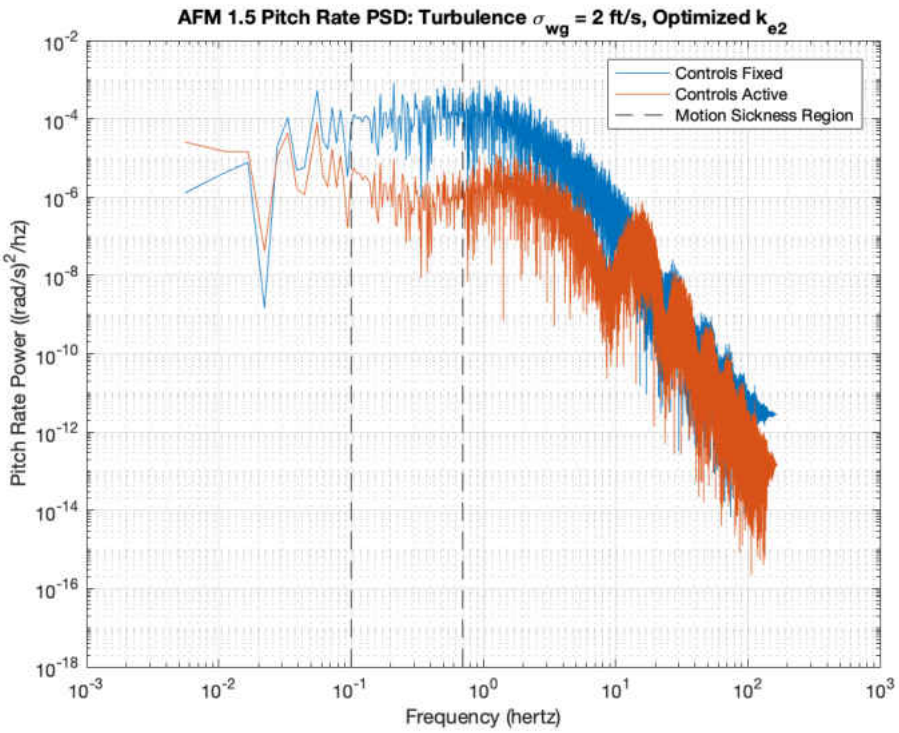

Figure 4.22 von Karman Turbulence Pitch Rate PSD, Optimized

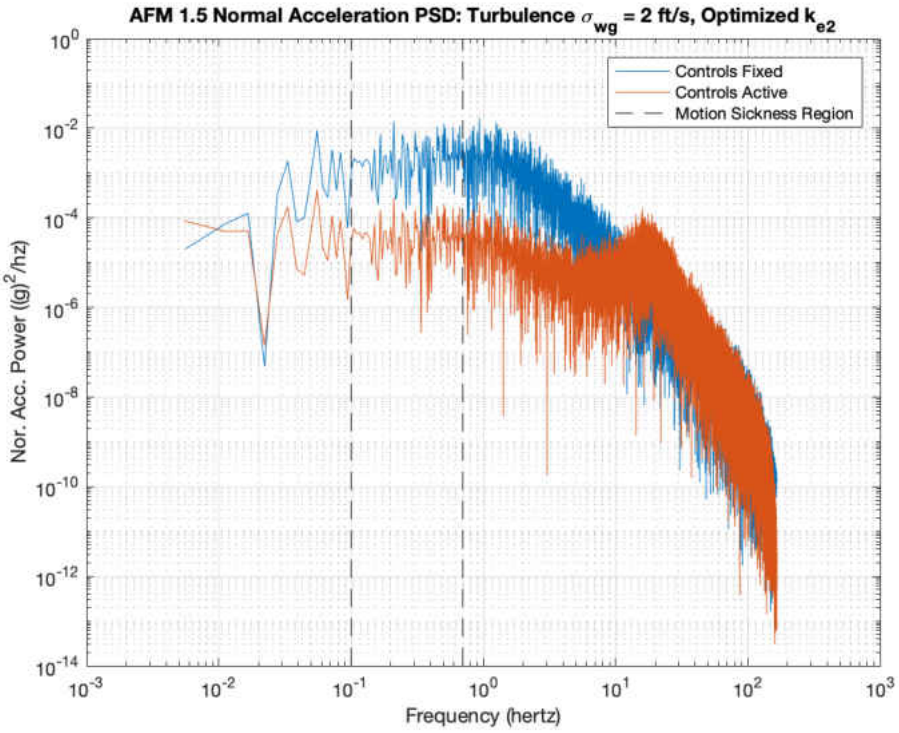

Figure 4.23 von Karman Turbulence Normal Acceleration PSD, Optimized

5 CONCLUSIONS AND RECOMMENDATIONS

5.1 Conclusions

A two degree of freedom, pitch-plunge dynamics, mathematical model, based on geometric attributes and assumed flight conditions, of ViGYAN's ARIS Flight Model, version 1.5, was successfully created. A disturbance wind input was added to the mathematical model and then was split into three separate inputs for each major component, including the wing, body, and tail. The separate gust model was then validated via time history comparisons of the single and separate gust models. To further enhance the realism of the model, unsteady aerodynamic models were appended, and a transfer function for the forward gust sensor utilized on the model was generated. A two stage gust alleviation control strategy using the full-span wing flap and tail elevator, based on the mechanics of the aircraft behavior, was formulated. Appropriate gains for the control laws were calculated, based on the model's stability derivatives. A step gust, doublet gust, and von Karman generated random turbulence were input into the model for linear simulations. Controls active cases were plotted over controls fixed cases for visual comparisons. Power spectral densities were computed, so that root mean square levels of pitch rate and normal acceleration could be calculated in the motion sickness range. Upon optimizing the second gain of the elevator motion, an order of magnitude reduction in both pitch rate and normal acceleration was achieved, thus fulfilling the theoretical goal of the ARIS project. The feasibility of a practical gust alleviation system offering significant potential ride quality improvement in a turbulent environment, for general aviation

aircraft, has been established, warranting further investigation and development, particularly flight testing.

5.2 Recommendations

Although much progress has been made, further research is recommended. The methodology of this gust alleviation system, so far, has been one of an open-loop system. To accommodate changes in flight speed, a closed-loop formulation should be applied. Head on gusts may be considered by adding the third, surge degree of freedom to the longitudinal dynamics model. Also, a lateral-directional dynamic model could be created and added to the current model, with the third longitudinal degree of freedom, to create a full six degree of freedom model. Phenomena such as hinge-moments and flutter should be investigated, as well. With the open-loop architecture, the dependency of the optimum gain value set on the wind disturbance was observed. This dependency needs to be explored further, in order to assess the performance robustness of this strategy. If significant sensitivity is found, an adaptive real-time system that tunes the control gains and elevator delay time for maximum performance should be considered. Once the preceding research is complete, the mathematical model should be scaled to the full size aircraft. Many changes will occur, including values of stability derivatives, lead and lag times, control surface delay times, etc. However, the research included in this manuscript will serve as a solid foundation for future researchers.

REFERENCES

[1] McCauley, M. E., Royal, J. W., Wylie, C. D., O'Hanlon, J. F., and Mackie, R. R., "Motion Sickness Incidence: Exploratory Studies of Habituation, Pitch and Roll, and the Refinement of a Mathematical Model," ONR-TR-1733-2, Human Factors Research Inc., Goleta, California, April, 1976.

[2] Hunsaker, J. C. and Wilson, E. B., "Report on Behavior of Aeroplanes in Gust: Part II. - Theory of an Aeroplane Encountering Gusts," NACA-TR-1, Massachusetts Institute of Technology, Cambridge, Massachusetts, January, 1917.

[3] Oxford Dictionary of English, "Gust," Oxford University Press, Oxford, England, 2010.

[4] Hoblit, F. M., "Gust Loads on Aircraft: Concepts and Applications," American Institute of Aeronautics and Astronautics, Washington, District of Columbia, 1988.

[5] Houbolt, J. C., "Atmospheric Turbulence," Proceedings of the AIAA-1972-219, Proceedings of the AIAA Aerospace Sciences Meeting, San Diego, California, January, 1972.

[6] International Civil Aviation Organization, "Manual on Low-Level Wind Shear," Doc 9817-AN/449, International Civil Aviation Organization, Montreal, Canada, 2005.

[7] Press, H. and Mazelsky, B., "A Study of the Application of Power-Spectral Methods of Generalized Harmonic Analysis to Gust Loads on Airplanes," NACA-TR-1172, Langley Research Center, Hampton, Virginia, January, 1954.

[8] von Karman, T., "The Fundamentals of the Statistical Theory of Turbulence," Journal of the Aeronautical Sciences, Vol. 4, No. 4, February, 1937, pp. 131-138.

[9] Dryden, H. L., "The Theory of Isotropic Turbulence," Journal of the Aeronautical Sciences, Vol. 4, No. 7, May, 1937, pp. 273-280.

[10] Liepman, H. W., "On the Application of Statistical Concepts to the Buffeting Problem," Journal of the Aeronautical Sciences, Vol. 19, No. 12, December, 1952, pp. 793-800.

[11] Diederich, F. W. and Drischler, J. A., "Effect of Spanwise Variations in Gust Intensity on the Lift Due to Atmospheric Turbulence," NACA-TN-3920, Langley Research Center, Hampton, Virginia, April, 1957.

[12] Houbolt, J. C., Steiner, R., and Pratt, K. G., "Dynamic Response of Airplanes to Atmospheric Turbulence Including Flight Data on Input and Response," NASA-TR-R-199, Langley Research Center, Hampton, Virginia, June, 1964.

[13] Bairstow, L. and Naylor, J. L. "The Longitudinal Motion of an Airplane in a Natural Wind When Use is Made of the Elevator," Report No 121, Advisory Committee for Aeronautics, London, England, 1913, pp 259-270.

[14] Donley, P. and Shufflebarger, C. C., "Tests of a Gust-Alleviating Flap in the Gust Tunnel," NACA-TN-745, Langley Research Center, Hampton, Virginia, January, 1940.

[15] Ludwig, L. G., "A Proposed Gust Alleviation System for Aircraft," Report No. SB-653-5-2, Cornell Aeronautical Laboratory, Buffalo, New York, February, 1950.

[16] Phillips, W. H. and Kraft, C. C., "Theoretical Study of Some Methods for Increasing the Smoothness of Flight Through Rough Air," NACA-TN-2416, Langley Research Center, Hampton, Virginia, July, 1951.

[17] Kraft, C. C., "Initial Results of a Flight Investigation of a Gust-Alleviation System," NACA-TN-3612, Langley Research Center, Hampton, Virginia, April, 1956.

[18] Crabill, N. L., "A Theoretical Investigation of a Simple Gust Alleviator," M.S. Thesis, University of Virginia, Charlottesville, Virginia, 1956.

[19] Krag, B., Rohlf, D., and Wonnenberg, H., "OLGA, A Gust Alleviation System for Improvement of Passenger Comfort of General Aviation Aircraft," ICAS-1980-5.4, Proceedings of the International Council of the Aeronautical Sciences, Munich, Germany, October, 1980.

[20] Etkin, B., "Turbulent Wind and Its Effect on Flight," AIAA-1980-1836, Proceeding of the AIAA Aircraft Systems Meeting, Anaheim, California, August, 1980.

[21] Etkin, B., "Turbulent Wind and Its Effect on Flight," Journal of Aircraft, Vol. 18, No. 5, May, 1981, pp. 327-345.

[22] Rynaski, E. G., "Gust Alleviation - Criteria and Control Laws," AIAA-1979-1676, Proceedings of the AIAA Atmospheric Flight Mechanics Conference, Boulder, Colorado, August, 1979, pp. 387-392.

[23] Rynaski, E. G., Andrisani, D., and Eulrich, B. J., "'Gust Alleviation Using Direct Turbulence Measurements," AIAA-1979-1674, Proceedings of the AIAA Atmospheric Flight Mechanics Conference, Boulder, Colorado, August, 1979, pp. 379-386.

[24] Motyka, P. R., Rynaski, E. G., and Reynolds, P. A., "Theory and Flight Verification of the TIFS Model-Following System," Journal of Aircraft, Vol. 9, No. 5, May, 1972, pp. 347-353.

[25] Burris, P. M. and Bender, M. A., "Aircraft Load Alleviation and Mode Stabilization (LAMS) Flight Demonstration Test Analysis," AFFDL-TR-68-164, Air Force Flight Dynamics Laboratory, Wright-Patterson Air Force Base, Ohio, December, 1969.

[26] Disney, T. E., "C-5A Active Load Alleviation System," Journal of Spacecraft and Rockets, Vol. 14, No. 2, February, 1977, pp. 81-86.

[27] Johnston, J. F., "Accelerated Development and Flight Evaluation of Active Controls Concepts for Subsonic Transport Aircraft, Volume 1: Load Alleviation/ Extended Span Development and Flight Test," NASA-CR-159097, Langley Research Center, Hampton, Virginia, September, 1979.

[28] Schoenman, R. L., "Thirty Years with the Jets, Commercial Transport Flight Management Systems - Past, Present, and Future," AIAA-1986-2289, Proceedings of the AIAA Guidance, Navigation, and Control Conference, Williamsburg, Virginia, August, 1986.

[29] Britt, R. T., Jacobson, S. B., and Arthurs, T. D., "Aeroservoelastic Analysis of the B-2 Bomber," Journal of Aircraft, Vol. 37, No. 5, September-October, 2000, pp. 745-752.

[30] Parks, E. K., Wingrove, R. C., Bach R. E., and Mehta, R. S., "Identification of Vortex-Induced Clear Air Turbulence Using Airline Flight Records," Journal of Aircraft, Vol. 22, No. 2, February, 1985, pp. 124-129.

[31] Wingrove, R. C. and Bach, R. E., "Severe Turbulence and Maneuvering from Airline Flight Records," Journal of Aircraft," Vol. 31, No. 4, July-August, 1994, pp. 753-760.

[32] Robinson, P. A., "The Use of Predictive Lidar Measurements in Alleviating Turbulence Induced Disturbances of Aircraft in Flight," SPIE-AS-1996-PP-86-97, Proceedings of the SPIE AeroSense Conference, April, 1996, pp. 86-97.

[33] Gatt, P., Shald, S., Robinson, P., and Newman, B., "Feed-Forward Turbulence Mitigation with Coherent Doppler Lidar," Phase II SBIR Final Report, NAS4-01007, Langley Research Center, Hampton, Virginia, March, 2003.

[34] von Karman, T., "Airfoil Theory for Non-Uniform Motion," Journal of the Aeronautical Sciences, Vol. 5, No. 10, 1938, pp. 379-390.

[35] Jones, R. T., "The Unsteady Lift of a Wing of Finite Aspect Ratio," NACA-TR-681, Langley Research Center Hampton, Virginia, January, 1940.

[36] Garrick, I. E., "On Some Reciprocal Relations in the Theory of Nonstationary Flows," NACA-TR-629, Langley Research Center, Hampton, Virginia, January, 1938.

[37] Theodorsen, T., "General Theory of Aerodynamic Instability and the Mechanism of Flutter," NACA-TR-496, Langley Research Center, Hampton, Virginia, May, 1934.

[38] Kussner H. G., Zusammenfassender Bericht iiber den instatiodren Auftrieb von Fliigeln, Luftfahrtforschung, Bd. 13, Nr. 12, 20, December, 1936, 410-424.

[39] Newman, B. A., "Multivariable Techniques for High-Speed Research Flight Control Systems," NASA-CR-1999-209528, Langley Research Center, Hampton, Virginia, December, 1999.

[40] Yechout, T. R., "Introduction to Aircraft Flight Mechanics," American Institute of Aeronautics and Astronautics, Reston, Virginia, 2014.

VITA

Lucas Coleman Mills earned a B.S. in Mechanical Engineering from Old Dominion University in July of 2015 and will complete a M.S. in Aerospace Engineering from Old Dominion University in December of 2018. While at Old Dominion University earning his masters degree, Mr. Mills worked for ViGYAN in Hampton, Virginia, performing flight mechanics research on their Active Ride Improvement System. He also wrote MATLAB scripts and created Graphical User Interfaces for NASA personnel for data analyzation of the Space Launch System Rocket. Additionally, Mr. Mills participated in the Summer Faculty Fellowship Program on Kirtland Air Force Base in Albuquerque, New Mexico during the Summer of 2017, performing orbital mechanics research. Following graduation, Mr. Mills began employment with the Raytheon Company as a Systems Engineer supporting the PATRIOT Air and Missile Defense System.